Rashba spin-splitting and terahertz quantum Hall effect for heavy holes in strained germanium quantum wells

by

Michele Failla

Thesis

Submitted to the University of Warwick

for the degree of

Doctor of Philosophy

Department of Physics

June 2017

Contents

Acknowledgements

I would first like to thank my supervisor James Lloyd-Hughes for his support, guidance and attitude towards me and my project. Apart from the really nice work environment I found here at the University of Warwick, I am glad he gave me the opportunity to visit and perform experiments in renowned universities such as Oxford and ETH in Zurich. I would also like to acknowledge the financial support of the EPSRC.

Furthermore, in chronological order, I want to thank the Oxford THz Photonics Group, with particular gratitude towards Prof. Michael B. Johnston for access to their superconducting magnet system, and to Samuel Jones for helping me with experiments presented in Chapter 4.

Special thanks to Prof. Jérôme Faist, Dr. Giacomo Scalari and all the Quantum Optoelectronics Group at ETH Zurich, where I performed experiments (Chapter 5) with the great help, company and support of Janine Keller.

I also want to thank Dr. Maksym Myronov, Dr. Chris Morrison and Prof. David Leadley of the Nano-Silicon Group at the University of Warwick for providing high quality samples, performing magnetotransport measurements as well as for the useful and interesting meetings. I would like to acknowledge, and thank Mark Crouch of the Quantum Devices group at the University of Warwick for all the training and useful help with all of the clean room processes, as well as the help from Neil Wilson, of the Microscopy Group at the University of Warwick, with using the AFM.

Finally, I would like to take the opportunity to thank all the new friends I made in these four quick years in Coventry for their support and for the really nice time spent together.

This thesis is dedicated to my parents, because of the way they brought me up. If I am glad to be who I am, it is thanks to them.

Grazie a tutti!

Declaration

This thesis is submitted to the University of Warwick in support of my application for the degree of Doctor of Philosophy. It has been composed by myself and has not been submitted in any previous application for any degree.

The work presented (including data generated and data analysis) was carried out by the author except when specified within the thesis.

Samples presented in Section 3.4 were grown by Dr. Maksym Mironov and colleagues (Nano Silicon group at the University of Warwick). The magneto-transport characterisation of the SiGe1 and SiGe2 samples (as presented in Section 3.4.1) was performed by Dr. Christopher Morrison (Nano Silicon group).

Parts of this thesis (Chapter 4 and 5) have been published by the author as indicated in the related chapters.

Publications

The following is a list of publications to which I have contributed during my PhD project (in chronological order).

1. "*Influence of nonmagnetic Zn substitution on the lattice and magnetoelectric dynamical properties of the multiferroic material CuO*"
   S. P. P. Jones, N. C. Wurz, **M. Failla**, D. Prabhakaran, C. F. McConville, and J. Lloyd-Hughes
   Phys. Rev. B **90**, 064405 (2014)

2. "*Interfacial and bulk polaron masses in $Zn_{1-x}Mg_xO/ZnO$ heterostructures examined by terahertz time-domain cyclotron spectroscopy*"
   J. Lloyd-Hughes, **M. Failla**, J. Ye, S. P. P. Jones, K. L. Teo and C. Jagadish
   Appl. Phys. Lett. **106**, 202103 (2015)

3. "*Narrow heavy-hole cyclotron resonances split by the cubic Rashba spin-orbit interaction in strained germanium quantum wells*"
   M. Failla, M. Myronov, C. Morrison, D. R. Leadley and J. Lloyd-Hughes
   Phys. Rev. B **92**, 045303 (2015)

4. "*Terahertz quantum Hall effect for spin-split heavy-hole gases in strained Ge quantum wells*"
   M. Failla, J. Keller, G. Scalari, C. Maissen, J. Faist, C. Reichl, W. Wegscheider, O. J. Newell, D. R. Leadley, M. Myronov and J. Lloyd-Hughes
   New Journal of Physics **18**, 113036 (2016)

5. "*Terahertz spectroscopy of anisotropic materials using beams with rotatable polarization*"
   C. D. W. Mosley , **M. Failla**, D. Prabhakaran and J. Lloyd-Hughes
   Submitted to Optics Express, (2017)

The following is a list of talks and posters which I presented during my PhD course (in reverse chronological order).

1. Contributed talk: "*Terahertz time-domain magneto-spectroscopy of spin-split heavy-hole gases in strained Ge quantum wells: the Rashba and optical quantum Hall effects*", ICSI-10, Coventry, UK (May 2017)
2. Poster: "*Terahertz quantum Hall effect for spin-split heavy-hole gases in strained Ge quantum wells*", OTST 2017, London, UK (April 2017)
3. Contributed talk: "*Narrow cyclotron resonances of heavy-holes in strained germanium quantum wells split by the cubic Rashba spin-orbit interaction*", E-MRS 2015 Fall Meeting, Warsaw, Poland (September 2015)
4. Invited talk: "*Quantum spin dynamics and spin-orbit coupling at terahertz frequencies in strained germanium quantum wells*", 2015 EMN, Cancun, Mexico (June 2015)
5. Contributed talk: "*Split cyclotron resonances in strained Ge quantum well probed by THz time-domain spectroscopy*", ICOOPMA 2014, Leeds, UK (July 2014)

List of abbreviations

2DEG/2DHG	Two dimensional electron/hole gas
AFM	atomic force microscopy
BIA	bulk inversion asymmetry
CB	conduction band
CES	constant energy surface
CMOS	complementary metal oxide semiconductor
CR	cyclotron resonance
CRA/CRI	cyclotron active/inactive modes
CVD	chemical vapour deposition
DOS	density of states
DP	Dyakonov-Perel mechanism
EFA	envelope function approximation
EMA	effective mass approximation
EOS	electro-optic sampling
EPP	empirical pseudopotential method
EY	Elliott-Yafet mechanism
FET	field effect transistor
FB	Fabry-Perot
HH	heavy hole
HWP	half wave plate
iPCE	interdigitated photoconductive emitter
IQHE	integer quantum Hall effect
ITRS	International Technology Roadmap for Semiconductors
JDOS	joint density of states
LL	Landau level
MOD	modulation doping
MOS	metal-oxide-semiconductor
MOSFET	metal-oxide-semiconductor field effect transistor
MT	magnetotransport
NPP	nonlocal pseudopotential method
OQHE	optical quantum Hall effect
PC	photoconductive
PD	photodiode
PP	pseudopotential method

PR-THz-TDMS	polarisation-resolved THz-TDMS
QHE	quantum Hall effect
QW	quantum well
QW-FET	quantum well field effect transistor
QWP	quarter wave plate
RMS	root mean square
RP-CVD	reduced-pressure chemical vapour deposition
RP-THz-TDS	rotatable polarisation THz-TDS
SC	semiconductor
SdH	Shubnikov-de Haas
sGe-QWs	strained germanium quantum wells
SIA	structural inversion asymmetry
SOI	spin-orbit interaction
THz-TDS	THz time-domain spectroscopy
THz-TDMS	THz time-domain magneto-spectroscopy
VB	valence band
WAL	weak anti-localisation
WL	weak localisation
XTEM	cross-sectional transmission electron microscopy

List of symbols

a	lattice constant
$a_{\parallel}$	in-plane lattice constant
a_0	unstrained lattice constant
$a^{\dagger}, a$	creation and annihilation operators
$\boldsymbol{A} = \boldsymbol{A}(\boldsymbol{r})$	vector potential
α	Rashba coefficient for electrons
$\alpha(\omega)$	absorption coefficient
b^{ij}	BIA coefficient
$\boldsymbol{B}$	applied magnetic field
$\boldsymbol{B}_{\text{eff}}$	effective magnetic field
$\boldsymbol{B}^{\text{BIA}}(\boldsymbol{k}_{\parallel})$	effective magnetic field from BIA
$\boldsymbol{B}^{\text{SIA}}(\boldsymbol{k}_{\parallel})$	effective magnetic field from SIA
β	Rashba coefficient for HHs and LHs
β_{MT}	Rashba coefficient for HHs and LHs from MT measurements
β_p	Rashba coefficient from the spin-split density obtained from THz-TDMS
c	speed of light
Δ	Rashba splitting energy
Δ_p	Rashba splitting energy obtained from THz-TDMS
Δ_{MT}	Rashba splitting energy from MT measurements
Δ^{-}	momentum matrix element
Δ_0, Δ_0'	SO-energies
Γ	Landau level linewidth (broadening)
g	density of states
g_B	density of states for Landau levels at B
g_0	electron g-factor
g^{*}	effective g-factor

E	energy
E_g	energy gap
$E(\boldsymbol{k}_\downarrow), E(\boldsymbol{k}_\uparrow)$	energy for spin-down and spin-up states
$E_\pm(\boldsymbol{k}_\parallel)$	energy for spin-down and spin-up states in 2D-systems
E_{mn}	energy for the n-th subband and m bulk band (see $_m$)
$E^\pm_{mn\mathcal{N}}(B)$	spin-split energy for the band m, n-th subband and Landau level index $\mathcal{N}$
$E_\pm = \sqrt{1/2}(E_x \pm iE_y)$	cyclotron resonance active and inactive mode
$E^\pm_{\mathrm{CR}} = E^{\uparrow\downarrow}_{\mathrm{CR}} = \hbar\omega_{c,\uparrow\downarrow}$	cyclotron resonance energies: transition energies from spin-up to spin-up states and from spin-down to spin-down states
η	ellipticity
E_0, E_0'	energy gaps
$E(\boldsymbol{k})$	energy dispersion
E_{F}	Fermi energy
E_{THz}	THz-pulse
$E_t(\omega)$	THz-pulse transmitted through the sample
$E_r(\omega)$	reference THz-pulse
$\boldsymbol{\mathcal{E}}$	electric field
$\epsilon_\parallel$	in-plane element of the strain tensor
$\epsilon(\omega)$	complex dielectric function
ϵ_L	lattice dielectric function
$f(E, \mu_{\mathrm{F}}, T)$	Fermi-Dirac distribution
f	occupation factor
$\gamma_1, \gamma_2, \gamma_3$	Luttinger parameters
$\gamma_1', \gamma_2', \gamma_3'$	reduced Luttinger parameters
H	Hamiltonian
H'_{ij}	perturbed component of the Hamiltonian
H_{SO}	spin-orbit Hamiltonian
I_l^{ij}	invariants
j	total angular momentum
$\boldsymbol{J}$	current density
$\boldsymbol{k}$	wavevector
$k_\parallel$	in-plane wavevector
k_{F}	Fermi wavevector
$k_\pm = k_x \pm ik_y$	
κ'	reduced Luttinger paramater
L	quantum well thickness
$\boldsymbol{l}$	orbital angular momentum
λ	spin-orbit coupling factor

λ_c	magnetic length
m	index for conduction, light hole or heavy hole band
m_0	electron mass
m_b^*	effective mass at the band-edge (i.e. $k = 0$)
m_{THz}^*	effective mass obtained from magnetic field dependence of the cyclotron frequency
m_j	projection of total angular momentum
m_{HH}^*	effective mass for heavy holse
m_{LH}^*	effective mass for light holes
m_{ij}	matrix tensor element of the effective mass
m_{MT}^*	effective mass obtained from MT experiments
$\mu_B = e\hbar/(2m_0)$	Bohr magneton
μ_{F}	chemical potential
μ	mobility
n	subband index in quantum wells
n_B	number of states (per unit area) for Landau levels
$\tilde{n} = n(\omega) + i\kappa(\omega)$	complex refractive index
N	volume carrier density
$N_\pm$	spin-split density ($_+$: up, $_-$: down)
N_s	sheet carrier density
$\mathcal{N}$	Landau level index
ω_c	cyclotron frequency
Ω_{dir}	volume of the primitive cell in real space
Ω_{rec}	volume of the primitive cell in reciprocal space
P, P'	momentum matrix element
$p = -i\hbar\nabla$	momentum operator
$\boldsymbol{p} = \hbar\boldsymbol{k}$	kinetic momentum
$p_{\uparrow,\downarrow}^{\mathrm{MT}}$	spin-split sheet density from MT measurements
$p_{\uparrow,\downarrow}^{\mathrm{THz}}$	spin-split sheet density from THz-TDMS
p_{2D}^{THz}	total sheet density from fits of THz-TDMS
$p_{\mathrm{2D}}^{\mathrm{sum}}$	total sheet density from sum rule
$p_{\mathrm{2D}}^{\mathrm{Hall}}$	total sheet density from classical Hall conductivity
ψ	wavefunction
$\Psi(\boldsymbol{r})$	wavefunction expansion in terms of band-edge Bloch functions
Q	momentum matrix element
r^{ij}	SIA coefficient
ρ	resistivity tensor
σ	conductivity tensor
$\sigma(\omega)$	optical conductivity
σ_0	DC sheet conductivity
$\boldsymbol{\sigma}$	vector of Pauli spin matrices
$\boldsymbol{s}$	spin angular momentum
τ	lifetime

τ_{s}	spin lifetime
τ_{tr}	transport lifetime
τ_{THz}	cyclotron resonance lifetime from THz-TDMS
τ_{q}	quantum lifetime
θ_F	Faraday angle
$\Theta_F(\omega, B)$	complex Faraday angle
$\boldsymbol{v}$	speed, drift velocity
ν	Landau levels filling factor
$V_0(\boldsymbol{r})$	periodic crystal potential
V_g	pseudopotential form factor
V_{G}	gate voltage
x	element content
χ^2	residual

Abstract

Terahertz time-domain spectroscopy (THz-TDS) allows the investigation, in a non-contact fashion and in the meV range (1 THz = 4.14 meV), of the coherent motion of particles close to their equilibrium position. In contrast with other optical spectroscopy techniques, THz-TDS gives the chance to perform phase-resolved measurements and to investigate quantum coherent phenomena within different materials or systems such as two dimensional hole or electron gases (2DHGs, 2DEGs).

This thesis presents a thorough characterisation - by means of THz-TD magneto-spectroscopy (THz-TDMS) and polarisation resolved (PR)-THz-TDMS - of high mobility 2DHGs in 0.8% and 1.3% compressively strained germanium quantum wells (sGe-QWs) grown on SiGe virtual substrates. These are attractive systems for electronic and spintronic devices due to the compatibility of Ge with CMOS technology as well as their finite spin-orbit interaction (SOI). The SOI, driven by structural inversion asymmetry (SIA) in modulation doped SiGe heterostructures, can lift the spin degeneracy and provide spin-split states separated by the Rashba energy Δ even at zero external magnetic field. Results presented in the following thesis proved the strain-dependence of the Rashba spin-splitting as well as a non-contact determination of the g-factor, effective mass, transport lifetime and mobility.

In addition to THz-TDMS, PR-measurements determined the off-diagonal conductivity $\sigma_{xy}(\omega, B)$. This was obtained by analysing the Faraday effect, which was seen as a change in the polarisation of the incident THz-pulse due to the presence of carriers within the QWs, under the application of a magnetic field. Determining σ_{xy} revealed, for the first time in a 2DHG, features of the optical quantum Hall effect (OQHE), i.e. the QHE driven by an ac electric field (ac THz-field).

The thesis ends with introducing rotatable polarisation THz-TDS experiments to study anisotropic materials. As an outlook of the presented work, this experimental technique can be exploited in order to evaluate the anisotropic mobility in sGeQWs.

Chapter 1

Introduction: germanium for CMOS-technology

This chapter first introduces the history, trends and challenges of the modern semiconductor industry. After focusing on silicon complementary metal oxide semiconductor (Si-CMOS) technology, in Sections 1.1.1 and 1.1.2 high mobility quantum wells (QWs) and spintronics are introduced as alternative ways to improve the performance of electronic devices. As this thesis is focused on the characterisation of Ge-QWs, the general advantages of using Ge in Si-CMOS and spintronics are introduced in Section 1.2. Specifically, Section 1.2.1 highlights the already established use of Ge in SiGe-strain technology while the general structure of Ge-QWs is presented in Section 3.4. Finally, the overview of this thesis is given in Section 1.3.

1.1 Silicon-CMOS technology

Since its birth around 1960, the core activity of the semiconductor industry has been producing metal-oxide-semiconductor field effect transistors (MOSFETs) whose structure will be presented later in Section 2.2. These are used to switch or amplify electronic signals by exploiting a channel - i.e. two dimensional electron/hole gas (2DEG/2DHG) - formed between source and drain when the gate voltage is applied. Mostly all of the electronic devices (such as memories and CPUs) are nowadays based on Si-CMOS circuits where p- and n-channel MOSFETs are integrated together [1]. The dominance of Si ever since is linked to its abundance (about 28% of the Earth's crust) and also to the convenient insulating properties of silicon dioxide (SiO_2). This has been used as an excellent insulator between the conduction channel and the gate electrode in a MOSFET and is also exploited as a mask during device fabrication

[2].

As predicted by Moore's law in 1965, by scaling the device sizes - for instance the oxide thickness and channel length - the number of transistors on integrated circuits doubled approximately every two years without a significant increase of costs [3]. Besides the chance to integrate a larger number of transistors per area, this also allowed better device performance because of increased switching speeds, as well as decreased power consumption per MOSFET. The International Technology Roadmap for Semiconductors (ITRS) has been referring to smaller device generations, initially in accordance with the length of the gate, as *process node* or *technology node*. Since the 45-nm node, the term *node* does not refer to any particular size but it just describes smaller device generations.

The *classical* scaling process, i.e. without effectively changing the MOSFET structure, was possible thanks to advancements in fabrication facilities - especially lithographic techniques - down to the 130-nm node in 2001. Since then, the device scaling faced performance degradation [4] which led to different approaches in order to maintain Moore's law. One of the main issues was initially the thickness of the SiO_2 layer. It has scaled so thin (1.2 nm for the 90- and the 60-nm nodes) that the excessive tunnelling current from the gate to the channel led to a rise in power dissipation (and then heat) which had originally been effectively kept constant. This was overcome by introducing high-k dielectrics at the 45-nm and below nodes [5]. Even though a mitigation of the tunnelling current was obtained, high-k dielectrics resulted in lowered channel mobility, which had been improved by introducing SiGe strain technology since the 90-nm node [6, 7]. In fact, as it will be outlined in Section 2.1.3, the strain affects the band structure of semiconductors and can improve their carrier mobility.

Beyond the 32-nm node the small distance between source and drain resulted in the degradation of the so called *short-channel effects* [4, 8]. Moore's law has been then held by replacing the conventional two-dimensional structure of MOSFETs with 3D transistors as the multi-gate fin-based field effect transistors (FinFETs) [9] used at the 22-nm node [10] and in the last 14-nm node [11].

1.1.1 High mobility channels and QWs for CMOS

In order to extend Moore's law, a further approach (already mentioned in 2007 by the ITRS [12]) is to use materials with higher intrinsic carrier mobility, like III-V compound semiconductors or germanium (Ge) [13, 14, 15]. These materials present a higher mobility as a consequence of their lighter effective mass and longer relaxation time due to a different band structure (Section 2.1). Table 1.1 compares

Quantity	Unit	Si	Ge	GaAs	InP	InAs	InSb
μ_e	(cm^2/Vs)	1450	3900	9200	5400	40000	77000
m_e^*	(m_0)	1.08	0.55	0.067	0.082	0.023	0.014
μ_h	(cm^2/Vs)	430	1900	400	200	500	850
m_{HH}^*	(m_0)	0.49	0.28	0.45	0.45	0.57	0.44
m_{LH}^*	(m_0)	0.16	0.044	0.082	0.12	0.35	0.016
E_g	(eV)	1.12	0.66	1.42	1.34	0.36	0.17

Table 1.1: Comparison between the electrical properties of Si, Ge and III-V semiconductors for electrons (e) and holes (h) [16]. Quantities are as follows: E_g =bandgap; μ = mobility, m^* = effective mass. Subscripts LH and LH refer to heavy holes and light holes within the valence band.

3D electron/hole mobilities and effective masses of the most studied semiconductors [16]. Already in 2011, the ITRS indicated 2018 as the expected year to introduce high mobility channels based on III-V and Ge to replace Si channels for nFETs and pFETs, respectively [17]. In this context, a successful integration of InGaAs-nMOSFETs and Ge-pMOSFETs, on the same Ge-wafer and using Al_2O_3 as gate insulator, showed superior device performances [18].

Even if high carrier densities are needed to control short channel effects [8] in nano-scale FETs, they introduce other unwanted effects like slower channel mobility and band to band tunnelling [19]. This can be overcome by implementing low-dimensional structures, such as quantum wells (QWs) for FET (QW-FET) where enhanced carrier mobility at high carrier density can be obtained [20, 21]. For 2DEGs, the highest mobility at room temperature (RT) was found to be 5×10^4 cm^2/Vs in InSb-QWs [22], while at low-temperature, a 2DEG mobility of 3.5×10^7 cm^2/Vs was obtained in a GaAs-QW at 360 mK [23]. The highest 2DHG mobilities are obtained in strained Ge-QWs (sGe-QWs) with RT mobility in the range 2400 - 3100 cm^2/Vs (carrier densities between $5 - 41 \times 10^{11}$ cm^{-2}), and low temperature mobilities (below 12 K) in the range of $0.03 - 1.1 \times 10^6$ cm^2/Vs (carrier densities of $3 - 19 \times 10^{11}$ cm^{-2}) [20].

1.1.2 Beyond-CMOS: QWs for spintronics

Apart from the different approaches introduced previously, in order to improve device performances in Si-CMOS and proceed with the scaling trend, further strategies are explicitly considered by the ITRS. One of these, named *Beyond-CMOS* in 2009 [24], focuses on discovering new devices - which have been referred as *exotic* in 2003 by the ITRS [25] - in order to exploit a new state variable. While traditional logic signals are based on the current state (i.e. the On/Off states of a transistor), new states, for instance, can be related to the spin of carriers as in spintronics devices (Section 2.4). Alongside other alternatives, spintronics is considered promising for lower energy consumption. This, in principle, is because the charge interaction energy scale is eV while the spin interaction lies in the meV scale [26].

As summarised in this Section, it is clear that understanding and characterising charge and spin transport in QWs is fundamental to improvements in information technology. The following will focus on Ge as a suitable material for application in both Ge-CMOS and spintronics.

1.2 Current use of germanium and future prospects

Among existing semiconductors, as already shown in Table 1.1, Ge presents higher electron mobility than Si and the highest hole mobility. Even though the first *point contact* transistor was fabricated using Ge in 1947, this has only recently received more attention from the semiconductor industry after the demonstration of very high electron and hole mobilities at the GeO_2/Ge interface in bulk Ge MOSFET devices [27].

Furthermore, by considering the beyond-CMOS approach, Ge is an attractive material for spintronics applications because its crystal inversion symmetry precludes (as it will be introduced in Section 2.1) the spin relaxation of electrons by the Dyakonov-Perel mechanism [28] (see Section 2.4). To date, RT experiments on Ge-bulk reported a spin diffusion length up to 660 nm [29] and relatively long spin lifetimes of up to 5 ns [30] only for n-type Ge, where the Elliot-Yafet spin relaxation mechanism (see Section 2.4) was identified as dominant [31]. Conversely, for p-type Ge-bulk, RT spin injection and transport have not yet been investigated [26] but a spin-lifetime of ~ 150 ps, at $\sim 6\,\mathrm{K}$ was reported [32].

The following describes the current application of Ge in SiGe-strain technology and the strained Ge-QWs characterised in this thesis.

1.2.1 $Si_{1-x}Ge_x$-alloy and Ge on Si-substrates

The advantages of directing research efforts towards Ge are linked to the fact that using Ge in modern Si-CMOS is already an established reality [33]. In fact, unlike other semiconductors, Ge is an element of the IV-group, with the same diamond structure of Si but with a 4.2% larger lattice constant ($a_{\mathrm{Si}} = 5.431\,\mathrm{Å}$ and $a_{\mathrm{Ge}} = 5.658\,\mathrm{Å}$). This makes Ge completely miscible in Si and, as introduced previously,

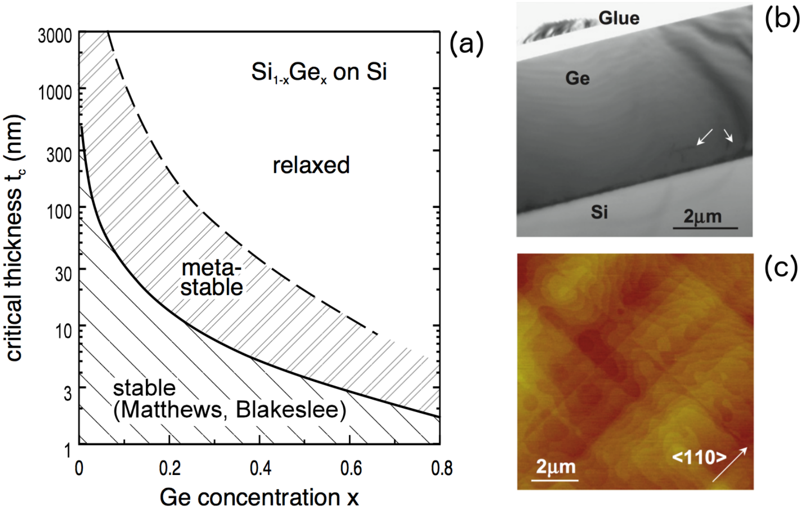

Figure 1.1: **(a)** Critical thickness t_c of $\mathrm{Si}_{1-x}\mathrm{Ge}_x$ as a function of the Ge concentration x (see text) [2]; Example of 4.7 μm thick Ge layer on Si growth by CVD: **(b)** XTEM images (white arrows indicate dislocations) [35], **(c)** AFM scan [35].

was already used as an important way to maintain the Moore's law by means of strain-engineering, which is based on the use of SiGe-alloys [6].

In more detail, the content $0 < x < 1$ of Ge can be varied to change the lattice constant of the $\mathrm{Si}_{1-x}\mathrm{Ge}_x$ buffer layer according to [34]:

$$a_{\mathrm{Si}_{1-x}\mathrm{Ge}_x} = a_{\mathrm{Si}}(1-x) + a_{\mathrm{Ge}}(x) + [0.0273(x^2 - 10x)]. \tag{1.1}$$

This increases with x and, because $a_{\mathrm{Si}_x\mathrm{Ge}_{1-x}} > a_{\mathrm{Si}}$, makes the SiGe buffer layer bi-axially compressively strained if deposited on Si-wafers (Section 2.1.3). The amount of strain energy increases with the SiGe thickness until dislocations start to form above a certain critical thickness t_c. Figure 1.1(a) shows the theoretical limit of t_c (Matthews and Blakelee curve [36]) under which the strained SiGe buffer layer remains stably strained. The top limit (People and Bean curve [37]) describes the thickness at which dislocation nucleation occurs, leading to relaxed SiGe. The region in between represents the thickness for which the SiGe is metastable. In this region, no relaxation occurs if the growth is performed at low temperatures (typically < 550°C) while any subsequent thermal process can cause the relaxation of the layer [2].

As a relaxed SiGe buffer layer serves as a substrate for depositing strained channels with enhanced mobility, it is often called a *virtual substrate*. According to Equation (1.1), $a_{\mathrm{Si}_x\mathrm{Ge}_{1-x}}$ depends on the Ge content x. In principle, SiGe virtual substrates can be used to incorporate all type of semiconductors by matching their lattice constant or making $a_{\mathrm{Si}_x\mathrm{Ge}_{1-x}}$ slightly different to exploit the associated strain [see Equation (2.30)] and improve the carrier mobility of deposited channels in Si-CMOS. For instance, Si layers grown on SiGe virtual substrates will experience a tensile biaxial strain which is maintained as soon as the layer thickness is kept below the critical value [38].

To obtain high quality relaxed/strained Si, Ge or SiGe-alloy layers on Si substrates, the best deposition technique is chemical vapour deposition (CVD), which is one of the conventional techniques for mass device production in modern Si-CMOS [26]. The main goal of a successful deposition is related to a low concentration of threading dislocations, i.e. dislocations that can run up through the deposited layer to terminate on the free surface and affect device properties, as they can provide a leakage path. A cross section transmission electron microscopy (XTEM) image of a Ge layer grown directly on Si(001), with threading dislocation density (TDD) below $10^7\,\mathrm{cm}^{-2}$, is presented in Figure 1.1(b). Atomic force microscope (AFM) scans, as shown in Figure 1.1(c), resulted in a root mean square (RMS) surface roughness below 1 nm [35].

1.3 Overview of this thesis

The suitability of Ge for Si-CMOS and spintronics was outlined in order to justify the impact of researching 2DHGs in sGe-QWs. The main aim of this thesis is to perform THz time-domain spectroscopy (THz-TDS) experiments in order to evaluate important material parameters such as density, transport lifetime, effective mass, mobility and the Rashba spin splitting in 2DHGs within the characterised sGe-QWs.

The theoretical background, needed to interpret and analyse experimental data, is summarised in Chapter 2. The THz-TDS setup used to obtain data reported within this thesis, as well as a general overview of the accessible informations from this technique, are outlined in Chapter 3, where the characterised sGe-QW samples are also presented. Chapter 4 reports the experimental data, related analysis and therefore the transport characterisation - obtained by means of THz-TD magneto-spectroscopy (THz-TDMS) - of 0.8% compressively sGe-QWs. The transport characterisation of 1.3% compressively sGe-QWs, as obtained by exploiting polarisation-resolved THz-TDMS, is presented in Chapter 5. Finally, in Chapter 6, a rotatable polarisation THz-TDS experiment is outlined as a suitable method to investigate the anisotropic mobility in sGe-QWs.

Chapter 2

Spin-splitting in 2D systems

The following chapter summarises the needed theoretical background for the analysis of THz-TDS experiments in sGe-QWs as characterised in this thesis. After a brief introduction to electronic band structure and crystal structure, Section 2.1 introduces the relevant background on free electrons, in order to define the density of states in the reciprocal space, effective mass and mobility. This ends by introducing the pseudo potential method in order to present the band structure of bulk Ge. As the spin-orbit interaction (SOI) is fundamental in describing the splitting of the valence band in semiconductors, its influence on the calculation of the band structure - along with the $\boldsymbol{k} \cdot \boldsymbol{p}$ and envelope function approximation models - is outlined together with the effects of strain on the band structure of Ge.

Two dimensional systems are introduced in Section 2.2 where MOSFET and QW-FET are presented together with the description, by means of the effective mass approximation, of the quantum confinement. As in the first section, this mostly focuses on sGe-QWs.

Section 2.3 introduces the SOI as responsible for structural inversion asymmetry which can provide spin-split states at a zero magnetic field in 2D-systems. The chance to exploit these spin-split states is presented in Section 2.4 where the main concepts of spintronics are introduced by focusing on the spin-FET transistor.

The effect of applying an external magnetic field in 2D-systems is described in Section 2.5, which also outlines magnetotransport measurements, together with a general introduction of the integer quantum Hall effect. Finally, before introducing the THz-TDS experiment in Chapter 3 and presenting the investigated samples, an example of a previous cyclotron resonance experiment in strained germanium quantum wells is outlined in Section 2.6.

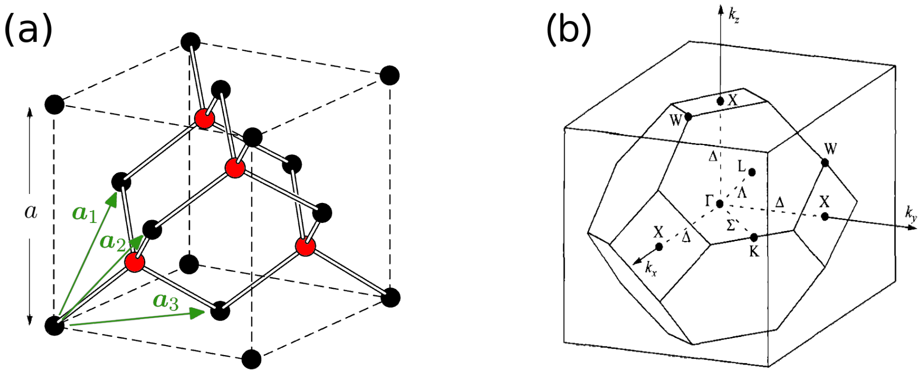

Figure 2.1: (**a**) Fcc structure for diamond and zinc-blende crystal semiconductors in the real space. (**b**) Example of reciprocal lattice for fcc structures with relative symmetry points. (Adapted from [39] and [1]).

2.1 Band structure of semiconductors

The behaviour of charge carriers within semiconductors (SCs) can be understood by considering how the valence electrons of single atoms are rearranged when these are close to each other within crystals or amorphous materials. The following section considers the case of IV semiconductors (Ge) or III-V compound semiconductors (GaAs) which crystallise in the face-centered cubic (fcc) structure depicted in Figure 2.1(a). While for the GaAs structure the black dots are Ga atoms and the red ones are As, leading to the so called *zincblende* structure, in the case of Ge all the atomic positions are occupied by the same element, making a *diamond* structure.

As will be outlined in Section 2.1.1, the calculation of the energy band structure is facilitated - through the *group theory* - by considering the crystal symmetries in relation to translation, rotation and reflection operators [39, 1, 40]. Electronic properties are understood by considering the *primitive* or *unit cell* of a crystal, as depicted in Figure 2.1(a) with respective *primitive lattice vectors* $(\boldsymbol{a}_1, \boldsymbol{a}_2, \boldsymbol{a}_3)$, which define the *real* or *direct lattice space.* Electrons, in a certain energy state E, are described by means of *wavefunctions* $\psi(\boldsymbol{k})$, where $\boldsymbol{k}$ is the *wavevector.* This represents a point in the *reciprocal lattice space*, whose basis vectors can be obtained from the primitive lattice constants $(\boldsymbol{a}_1, \boldsymbol{a}_2, \boldsymbol{a}_3)$ as [39, 1, 40]:

$$\boldsymbol{b}_i = 2\pi \frac{\boldsymbol{a}_j \times \boldsymbol{a}_k}{(\boldsymbol{a}_1 \times \boldsymbol{a}_2) \cdot \boldsymbol{a_3}}. \tag{2.1}$$

An example of reciprocal space for fcc crystals, together with the relevant symmetry points, is given in Figure 2.1(b). The main distinction between diamond and zincblende crystals is the lack of an *inversion center* or *centre of symmetry* for the zincblende structure [41]. By assuming the centre of symmetry at (0,0,0) in direct space, diamond structures (point group m3m) - referred to as *centrosymmetric* crystals - are such that one can find the same element with a translation from (x,y,z) to (-x,-y,-z). Consequently, in such structures there is no change in the electronic properties between the points (k_x, k_y, k_z) and $(-k_x, -k_y, -k_z)$ in the reciprocal space. On the other hand, as the presence of different elements prevents the existence of an inversion centre [42], zinc-blende crystals (point group $\bar{4}3$m) are said to be *non-centrosymmetric*.

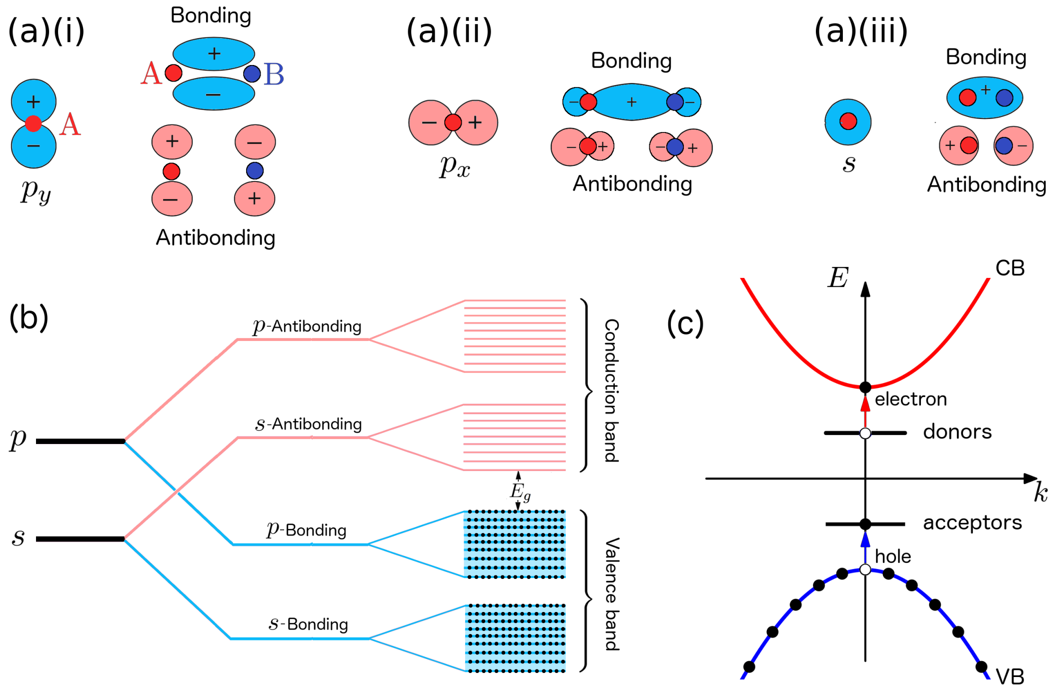

Figure 2.2: (**a**) Scheme of shared p_y- (**a**)(i), p_x- (**a**)(ii) and s-orbitals (**a**)(iii) for adjacent atoms in typical semiconductors such as Si, Ge and III-V compounds. The overlap can be bonding-like (symmetric in relation to the interchange of the atoms A→B and vice-versa) or antibonding-like (asymmetric). (**b**) Scheme of the overlap between p- and s-orbitals and formation of CBs and VBs separated by the energy gap E_g. (Adapted from [39] and [43]). (**c**) Scheme of parabolic band dispersion for CBs and VBs. The introduction of doping materials leads to the formation of localised energy states close to the VB (acceptors) or to the CB (donors).

Figure 2.2(a) shows a sketch of the electronic distribution, and related symmetry, for s- and p-orbitals of isolated Ge, or GaAs, atoms. By bringing atoms closer together, the electron wavefunctions overlap and create shared orbitals. These are classified in *bonding orbitals* (symmetric with respect to atom interchange, i.e. A→B) and *antibonding orbitals* (asymmetric). As depicted in Figure 2.2(b), the consequence of the mutual interaction of atoms within a solid consists of increasing (decreasing) the antibonding (bonding) orbital's energies and leads to the formation of conduction bands (CBs) and valence bands (VBs) separated by an energy gap E_g. The rearrangement of electrons in semiconductors leads to totally full VBs and empty CBs.

Free electron model in 3D. In order to introduce the energy band calculation in semiconductors, it is useful to treat first the case of free electrons in the primitive cell with volume $\Omega_{\mathrm{dir}} = a_1 \times a_2 \times a_3$. The periodic boundary conditions result in wavefunctions $\psi_{\boldsymbol{k}}(\boldsymbol{r})$ and energy dispersion $E_{\boldsymbol{k}}$ given as eigenfunctions and eigenvalues of the Schrödinger equation for free electrons:

$$H\psi_{\boldsymbol{k}}(\boldsymbol{r}) = \left[\frac{p^2}{2m_0}\right]\psi_{\boldsymbol{k}}(\boldsymbol{r}) = E(\boldsymbol{k})\psi_{\boldsymbol{k}}(\boldsymbol{r}), \tag{2.2}$$

where $p = -i\hbar\nabla$ is the momentum operator, $\hbar$ is the Planck's constant, m_0 is the electron mass. From Equation (2.2) one obtains:

$$\psi_{\boldsymbol{k}}(\boldsymbol{r}) = \frac{1}{\sqrt{\Omega_{\mathrm{dir}}}}e^{i\boldsymbol{k}\cdot\boldsymbol{r}} \quad \text{and} \quad E(\boldsymbol{k}) = \frac{\hbar^2|\boldsymbol{k}|^2}{2m_0}, \tag{2.3}$$

where the allowed wave vectors are $\boldsymbol{k} = (l_1\boldsymbol{b}_1, l_2\boldsymbol{b}_2, l_3\boldsymbol{b}_3)$ with $l_i = [0, \pm1, \pm2, \dots]$ and $\boldsymbol{b}_i$ from Equation (2.1). The energy dispersion $E(\boldsymbol{k})$ for free electrons in Equation (2.3) is isotropic and parabolic. Figure 2.2(c) shows an example, in one dimension, of the parabolic dispersion for CB and VB.

Density of states. Free carriers within SCs are obtained by means of *doping*, that is the introduction of a certain density of atoms with localised energy states that lie, as depicted in Figure 2.2(c), within the energy gap. Donor atoms provide electrons to the CB, whereas acceptors trap electrons from the VB, leaving electrons missing, i.e. *holes*. Doped SCs are called p-doped or n-doped in relation to the kind of introduced atoms. The amount of doping defines the last occupied energy level, corresponding to a particular k. Since the concentration of dopants is such that $\boldsymbol{k} \ll 2\pi/a_i$, the free electron model is often used to approximate the CB and VB in the vicinity of the gap where $\boldsymbol{k} \simeq 0$. By considering that each unit cell in reciprocal space has a volume $\Omega_{\mathrm{rec}} = (2\pi)^3/\Omega_{\mathrm{dir}}$, the density of states (DOS), i.e. the number of allowed states per unit volume of the reciprocal space and direct space, is given by $g(\boldsymbol{k}) = 2/(\Omega_{\mathrm{rec}}\Omega_{\mathrm{dir}}) = 2/(2\pi)^3$. Here the factor of 2 takes into account that every state can be occupied by two carriers with opposite spin. More generally, for a d-dimensional system, $g^d(\boldsymbol{k}) = 2/(2\pi)^d$ [44].

By introducing a density of carriers N within a volume Ω_{dir}, the energy band $E(\boldsymbol{k})$ is filled up to a specific wave-vector, named the Fermi vector $\boldsymbol{k}_{\mathrm{F}}$. This defines a sphere in reciprocal space with volume $(4/3)\pi k_{\mathrm{F,3D}}^3$ whose surface represents the Fermi energy $E_{\mathrm{F,3D}}$. From the condition $N = (4/3)\pi k_{\mathrm{F,3D}}^3 g^{d=3}(\boldsymbol{k})$, these two quantities are:

$$k_{\mathrm{F,3D}} = \left(\frac{3\pi^2 N}{\Omega}\right)^{1/3} \quad \text{and} \quad E_{\mathrm{F,3D}} = \frac{\hbar^2 k_{\mathrm{F,3D}}^2}{2m_0} = \frac{\hbar^2}{2m_0}\left(\frac{3\pi^2 N}{\Omega}\right)^{2/3}. \tag{2.4}$$

More precisely, the total number of carriers depends on the temperature through the Fermi-Dirac distribution

$$f(E, \mu_{\mathrm{F}}, T) = \frac{1}{1 + \exp[E - \mu_{\mathrm{F}})/(k_{\mathrm{B}}T)]}, \tag{2.5}$$

as

$$N = \int g(E) f(E, \mu_{\mathrm{F}}, T) dE, \tag{2.6}$$

where $g(E)$ is the energy-dependent DOS, k_{B} is the Boltzmann constant, T is the temperature and μ_{F} is the chemical potential which corresponds to E_{F} at $T = 0\,\mathrm{K}$. For any energy dispersion $E(\boldsymbol{k})$ in a d-dimensional system, a general expression for the energy-dependence of the DOS, per volume unit (d=3), area unit (d=2) or per length unit (d=1), is [45]:

$$g^d(E) = \frac{2}{(2\pi)^d} \int_0^{k(E)} d^d\boldsymbol{k}. \tag{2.7}$$

From the free electron model in 3D one obtains $g^{d=3}(E) = m_0\sqrt{2m_0E}/(\pi^2\hbar^3)$.

Effective mass and mobility. The response of carriers to applied electric or magnetic fields depends on their effective mass. This is essentially a tensor as it takes into account the response along different crystallographic directions. The effective mass is linked to the curvature of the energy dispersion [1]:

$$m_{ij}^* = \hbar^2 \left(\frac{\partial^2 E(k)}{\partial k_i \partial k_j}\right)^{-1}, \tag{2.8}$$

While for free electrons in 3D the effective mass from Equation (2.8) results in a constant mass m_0, in real systems m^* depends on $\boldsymbol{k}$ and therefore on the carrier density and the crystallographic direction probed. One of the most important parameters in electronic devices is the mobility of carriers μ. This relates the carrier drift velocity v_d to an applied electric field $\mathcal{E}$ as:

$$v_d = \mu\mathcal{E}. \tag{2.9}$$

In the relaxation approximation the mobility depends on the effective mass as well as on the carrier lifetime, or transport lifetime τ_{tr} - which describes the average time between scattering events with other carriers, impurities (like dopants) or phonons - as:

$$\mu = \frac{e\tau_{\text{tr}}}{m^*_{ij}}. \tag{2.10}$$

Since the mobility is related to the effective mass, this depends on the crystal orientation. Effective masses, mobilities and energy gaps, for the most studied semiconductors, were compared in Table 1.1.

Pseudopotential method. The interaction between electrons and the periodic crystal potential $V_0(\boldsymbol{r})$ are considered within Equation (2.2) as:

$$\left[\frac{p^2}{2m_0} + V_0(\boldsymbol{r})\right]\psi_{\boldsymbol{k}} = E_{\boldsymbol{k}}\psi_{\boldsymbol{k}}. \tag{2.11}$$

Within the *pseudopotential method* (PP), valence electrons are considered free but affected by the nuclear potential which is considered screened by electrons in the core shells, i.e. the *pseudopotential* or *local pseudopotential* [43, 39]. An example of a pseudopotential is depicted in Figure 2.3 (a) and is compared with the unscreened one. Since the pseudopotential can be considered as a weak perturbation of the free electron band structure, the PP method considers pseudo-wave-functions in the Schrödinger equation which are obtained by expanding them, in terms of plane waves $|\boldsymbol{k}\rangle$ in Equation (2.3), as:

$$\psi_{\boldsymbol{k}} = \sum_g a_g \left|\boldsymbol{k} + \mathbf{g}\right\rangle. \tag{2.12}$$

Here $\boldsymbol{g}$ is a vector of the reciprocal space obtained from a linear combination of the basis in Equation (2.1). The coefficients a_g and energies E_k are obtained by solving Equation (2.11), where the effect of $V(\boldsymbol{r})$ is related to the matrix elements:

$$\langle\boldsymbol{k}|V_0(\boldsymbol{r})|\boldsymbol{k} + \mathbf{g}\rangle \propto V_g, \quad \text{with} \quad V_g = \frac{1}{\Omega_{\text{dir}}}\int_{\Omega_{\text{dir}}} V_0(\boldsymbol{r})e^{-i\mathbf{g}\cdot\boldsymbol{r}}d\boldsymbol{r}. \tag{2.13}$$

The term V_g is known as the *pseudopotential form factor.* Generally, by using a

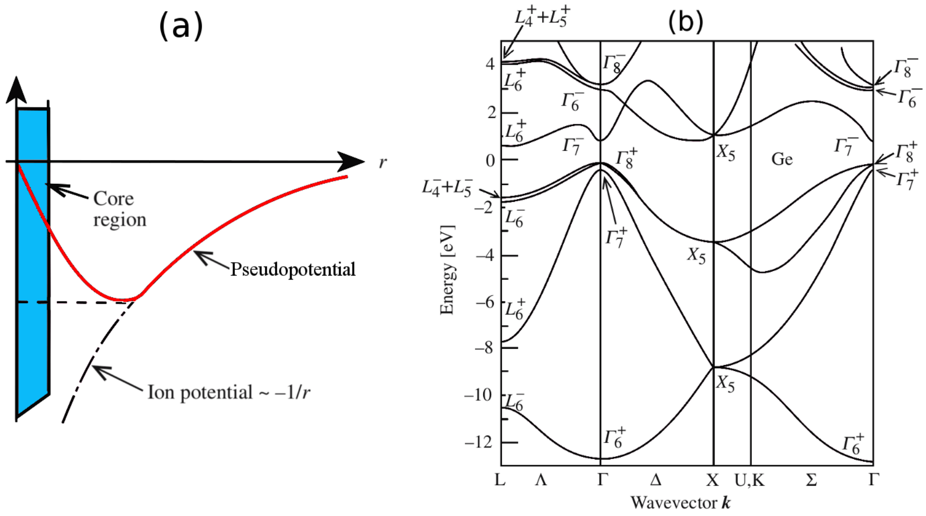

Figure 2.3: (**a**) Comparison between the ion potential and the pseudopotential which considers the screening of the core shells electrons. (**b**) Band structure of Ge, along different direction, obtained by the EPP method. (Adapted from [39]).

method called Empirical PP (EPP), V_g is iteratively varied in order to calculate and compare quantities obtained from experimental data. The band structure of Ge, along the different crystallographic directions depicted in Figure 2.1, is shown in Figure 2.3 (b). Labels $\Gamma_i^{\pm}$ - where ± refers to VB and CB, respectively - are known within the *theory of invariance* as the *double group notations* and describe the translational and rotational symmetries of the considered states in relation to the examined crystal structure [45, 39, 46] .

2.1.1 The spin-orbit interaction in band calculations

The Ge band structure in Figure 2.3 (b) also takes into account the effects of the spin-orbit interaction (SOI), the consideration of which is often indispensable to model experimental results.

The SOI arises as a relativistic effect which results in an effective magnetic field. By considering the Lorentz-transform and an electron orbiting around the nucleus with speed $v \ll c$ (nonrelativistic limit), where c is the speed of light, this *effective* magnetic field is given by [45]:

$$\boldsymbol{B}_{\text{eff}} = -\frac{1}{2}\frac{\boldsymbol{v} \times \boldsymbol{\mathcal{E}}}{c^2}, \tag{2.14}$$

and results in coupling the orbital angular momentum $\boldsymbol{l}$ and spin $\boldsymbol{s}$ through the spin-orbit Hamiltonian, $H_{\text{SO}} = \lambda \boldsymbol{l} \cdot \boldsymbol{s}$, where the strength of the interaction is given by the spin-orbit coupling factor λ.

In semiconductors, by analogy, charges move in a periodic potential $V_0(r)$ and the SOI is described by the Pauli SO Hamiltonian:

$$H_{\mathrm{SO}} = -\frac{\hbar}{4m_0^2c^2}\boldsymbol{\sigma}\cdot\boldsymbol{p}\times(\nabla V_0), \tag{2.15}$$

where $\boldsymbol{\sigma} = (\sigma_x, \sigma_y, \sigma_z)$ is the vector of Pauli spin matrices [46]. Therefore, by taking into account the SOI, a particular band requires to be described in terms of the total angular momentum $j = l + s$, and respective projection, m_j, along the direction of an effective magnetic field which arises as a relativistic effect. For instance, the p-like valence band ($l = 1$) is split into three different bands with projections $m_j = 3/2, 1/2$ [Γ_8^+ in Figure 2.3 (b)] and $m_j = 0$ [Γ_7^+]. In comparison with Si, since the electric field is provided by the crystal atoms, the SOI is stronger for heavier semiconductors like Ge and GaAs [39].

$\boldsymbol{k}\cdot\boldsymbol{p}$-method. Differently from the pseudopotential method, within the $\boldsymbol{k}\cdot\boldsymbol{p}$ theory the periodic potential $V_0(r)$ is considered through the Bloch functions:

$$\mathrm{e}^{i\boldsymbol{k}\cdot\boldsymbol{r}}u_{\nu\boldsymbol{k}}(\boldsymbol{r}) \equiv \mathrm{e}^{i\boldsymbol{k}\cdot\boldsymbol{r}}\left\langle \boldsymbol{r}|\nu\boldsymbol{k}\right\rangle. \tag{2.16}$$

The advantage of using Bloch functions consists of the fact that they implicitly include the potential periodicity within the functions $u_{\nu\boldsymbol{k}}(\boldsymbol{r})$. By including the Pauli-SO term given in Equation (2.15), the corresponding Schrödinger equation reads [39, 46]:

$$\left[\frac{p^2}{2m_0} + V_0 + \frac{\hbar^2k^2}{2m_0} + \frac{\hbar}{m_0}\boldsymbol{k}\cdot\boldsymbol{\pi} + \frac{\hbar}{4m_0^2c^2}\boldsymbol{p}\cdot\boldsymbol{\sigma}\times(\nabla V_0)\right]\left|n\boldsymbol{k}\right\rangle = E_n(\boldsymbol{k})\left|n\boldsymbol{k}\right\rangle, \tag{2.17}$$

where:

$$\boldsymbol{\pi} := \boldsymbol{p} + \frac{\hbar}{4m_0^2c^2}\boldsymbol{\sigma}\cdot\boldsymbol{p}\times(\nabla V_0) \tag{2.18}$$

and $\left|n\boldsymbol{k}\right\rangle$ are wave functions (spinors) with combined band-spin index n. For a fixed $\boldsymbol{k_0}$, the set $\left|n\boldsymbol{k_0}\right\rangle$ is a complete and orthonormal basis for the Schrödinger Equations (2.17), as well as $\left|\nu\boldsymbol{k_0}\right\rangle$, if one excludes the SOI term. This consideration allows an expansion of $\left|n\boldsymbol{k}\right\rangle$ in terms of the *band-edge* (i.e. at $\boldsymbol{k} = \boldsymbol{0}$) Bloch functions $\left|\nu\boldsymbol{0}\right\rangle$ times the spin eigenstates $\left|\sigma\right\rangle$ as:

$$\left|n\boldsymbol{k}\right\rangle = \sum_{\nu',\sigma'=\uparrow,\downarrow} c_{n\nu'\sigma'}(\boldsymbol{k})\left|\nu'\sigma'\right\rangle \tag{2.19}$$

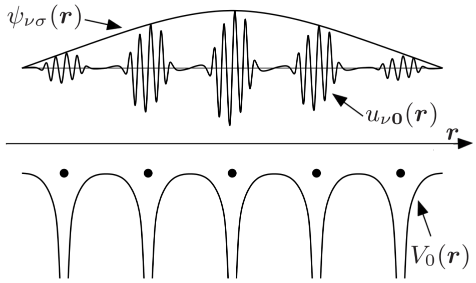

Figure 2.4: Comparison between the crystal potential, $V(\boldsymbol{r})$, Bloch function at the band edge, $u_{\nu\boldsymbol{0}}(\boldsymbol{r})$, and envelope function, $\psi_{\nu\sigma}(\boldsymbol{r})$. (Adapted from [46]).

where $|\nu'\sigma'\rangle := |\nu'\boldsymbol{0}\rangle \otimes |\sigma'\rangle$ and $c_{n\nu'\sigma'}(\boldsymbol{k})$ are expansion coefficients. By substituting $|n\boldsymbol{k}\rangle$ in Equation (2.17) and multiplying from the left by $\langle\nu\sigma|$:

$$\sum_{\nu',\sigma'} \left\{ \left[E_{\nu'}(\boldsymbol{0}) + \frac{\hbar^2 k^2}{2m_0} \right] \delta_{\nu\nu'}\delta_{\sigma\sigma'} + \frac{\hbar}{m_0}\boldsymbol{k}\cdot\boldsymbol{P}^{\nu\nu'}_{\sigma\sigma'} + \Delta^{\nu\nu'}_{\sigma\sigma'} \right\} c_{n\nu'\sigma'}(\boldsymbol{k}) = E_n(\boldsymbol{k}) c_{n\nu\sigma}(\boldsymbol{k}), \tag{2.20}$$

where

$$\boldsymbol{P}^{\nu\nu'}_{\sigma\sigma'} := \langle\nu\sigma|\boldsymbol{\pi}|\nu'\sigma'\rangle \qquad \text{and} \qquad \Delta^{\nu\nu'}_{\sigma\sigma'} := \frac{\hbar}{4m_0^2c^2}\langle\nu\sigma|\boldsymbol{p}\cdot\boldsymbol{\sigma}\times(\nabla V_0)|\nu'\sigma'\rangle \tag{2.21}$$

arise from the SOI and are called momentum matrix elements and SO energies, respectively. They are generally chosen in order to obtain the best agreement with experimental data such as cyclotron resonance experiments [47].

Envelope function approximation. Since semiconductors are often characterised by applying external electric or magnetic fields, it is necessary to introduce the envelope function approximation (EFA). The EFA considers the effect of these external fields by assuming that they vary slowly in comparison to the lattice constant of the considered semiconductors. In the EFA, the Schrödinger equation is given by [46]:

$$\left[\frac{(-i\hbar\nabla + e\boldsymbol{A})^2}{2m_0} + V_0(\boldsymbol{r}) + \frac{\hbar}{4m_0^2c^2}(-i\hbar\nabla + e\boldsymbol{A})\cdot\boldsymbol{\sigma}\times(\nabla V_0) + \right.$$
$$\left. + V(\boldsymbol{r}) + \frac{g_0}{2}\mu_B\boldsymbol{\sigma}\cdot\boldsymbol{B} \right]\Psi(\boldsymbol{r}) = E\Psi(\boldsymbol{r}). \tag{2.22}$$

Here $V(\boldsymbol{r})$ is the external electric field, $\boldsymbol{A} = \boldsymbol{A}(\boldsymbol{r})$ is the vector potential which results in a magnetic field $\boldsymbol{B} = \nabla\times\boldsymbol{A}$, $\mu_B = e\hbar/(2m_0)$ is the Bohr magneton and $g_0 = 2$ is the g-factor for free electrons. As within the $\boldsymbol{k}\cdot\boldsymbol{p}$-theory and the expansion in Equation (2.19), the new functions $\Psi(\boldsymbol{r})$ can be expanded in terms of the band-edge Bloch functions as:

$$\Psi(\boldsymbol{r}) = \sum_{\nu',\sigma'} \psi_{\nu',\sigma'}(\boldsymbol{r}) u_{\nu',\boldsymbol{0}} \left|\sigma'\right\rangle . \tag{2.23}$$

Figure 2.4 depicts the expansion coefficients $\psi_{\nu',\sigma'}(\boldsymbol{r})$ which are referred to as *envelope functions*. They slowly modulate the Bloch functions which have the periodicity of the crystal potential $V_0(\boldsymbol{r})$. By setting $\hbar\boldsymbol{k} = -i\hbar\nabla + e\boldsymbol{A}$, using Equation (2.23) and multiplying from the left by $\langle\sigma|\, u^*_{\nu\boldsymbol{0}}(\boldsymbol{r})$ one obtains the *EFA Hamiltonian* and the respective Schrödinger equation:

$$\begin{aligned}\sum_{\nu',\sigma'} \Bigg\{ \left[E_{\nu'}(\boldsymbol{0}) + \frac{\hbar^2 k^2}{2m_0} + V(\boldsymbol{r}) \right] \delta_{\nu\nu'}\delta_{\sigma\sigma'} + \frac{\hbar}{m_0}\boldsymbol{k}\cdot\boldsymbol{P}^{\nu\nu'}_{\sigma\sigma'} + \\ + \Delta^{\nu\nu'}_{\sigma\sigma'} + \frac{g_0}{2}\mu_B \boldsymbol{\sigma}\cdot\boldsymbol{B}\delta_{\nu\nu'} \Bigg\} \psi_{\nu',\sigma'}(\boldsymbol{r}) = E\psi_{\nu,\sigma}(\boldsymbol{r}),\end{aligned} \tag{2.24}$$

Note that $V(\boldsymbol{r})$ is not involved in the SOI term as the related electric field is much smaller than one from the atomic cores, i.e. $\nabla V(r) \ll \nabla V_0(r)$ [46].

Löwdin perturbation theory. Both Equations (2.20) and (2.24) consist of an infinite-dimensional set of coupled differential equations from which one can obtain the exact energy dispersion $E_n(\boldsymbol{k})$ and expansion coefficients $c_{n\nu'\sigma'}(\boldsymbol{k})$ or $\psi_{\nu,\sigma}(\boldsymbol{r})$. Generally, as this is quite a complex task, the diagonalisation of Equation (2.20), or Equation (2.24), is first obtained by considering a finite number of adjacent bands ($n = 1, \ldots, N$) for which the $\boldsymbol{k}\cdot\boldsymbol{p}$ and SOI are treated exactly in order to obtain $E_n(\boldsymbol{k})$ close to the expansion point $\boldsymbol{k}_0 = 0$. This results in a $N \times N$ Hamiltonian where the coupling between the N-bands is described by the off-diagonal terms H_{ij}. In a second step, the interaction between these bands with other bands, referred as *remote bands*, is obtained by treating the respective $\boldsymbol{k}$-dependent terms as small perturbations following the method introduced by Löwdin [48]. This results in perturbed off-diagonal components [39]:

$$H'_{ij} = H_{ij} + \sum_{r\neq i,j} \frac{H_{ir}H_{rj}}{E_i - E_k} + \ldots, \tag{2.25}$$

where $i, j = 1, \ldots, N$, and k denotes the index for the remote bands.

Theory of invariance and extended Kane model. In order to give an example of SOI splitting for the conduction and VBs, as well as their mutual coupling, the

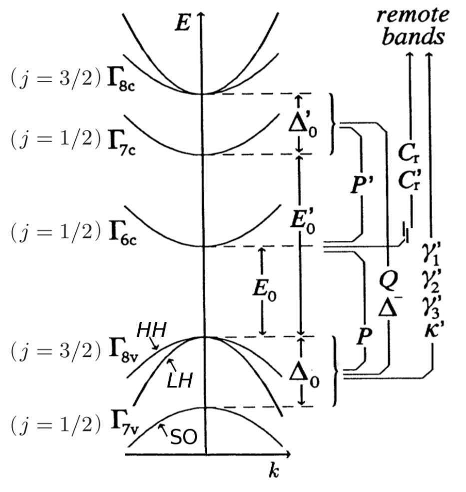

Figure 2.5: Scheme of the resulting splitting and coupling between the 14 states and remote bands, together with all the coupling terms, according to the Kane model. (Adapted from [49])

.

following introduces the use of the EFA Hamiltonian to calculate the band structure of GaAs by means of the extended Kane model. This considers the topmost bonding p-like (l=1) VB states (with eigenfunctions $|X\rangle, |Y\rangle, |Z\rangle$), the antibonding s-like ($l = 0$, $|S\rangle$) and p-like states ($|X'\rangle, |Y'\rangle, |Z'\rangle$) in the lowest CB, see Figure 2.2 (b). In relation to the number of respective projections m_j for different bands listed above, Equation (2.24) results in a set of 14 coupled differential equations for 14 envelope functions. The corresponding 14×14 Hamiltonian is given by [49]:

$$H_{14\times14} = \begin{pmatrix} H_{\Gamma_{7v}\Gamma_{7v}} & H_{\Gamma_{7v}\Gamma_{8v}} & H_{\Gamma_{7v}\Gamma_{6c}} & H_{\Gamma_{7v}\Gamma_{8c}} & H_{\Gamma_{7v}\Gamma_{7c}} \\ H_{\Gamma_{8v}\Gamma_{7v}} & H_{\Gamma_{8v}\Gamma_{8v}} & H_{\Gamma_{8v}\Gamma_{6v}} & H_{\Gamma_{8v}\Gamma_{8c}} & H_{\Gamma_{8v}\Gamma_{7c}} \\ H_{\Gamma_{6c}\Gamma_{7v}} & H_{\Gamma_{6c}\Gamma_{8v}} & H_{\Gamma_{6c}\Gamma_{6c}} & H_{\Gamma_{6c}\Gamma_{8c}} & H_{\Gamma_{6c}\Gamma_{7c}} \\ H_{\Gamma_{8c}\Gamma_{7v}} & H_{\Gamma_{8c}\Gamma_{8v}} & H_{\Gamma_{8c}\Gamma_{6v}} & H_{\Gamma_{8c}\Gamma_{8c}} & H_{\Gamma_{8c}\Gamma_{7c}} \\ H_{\Gamma_{7c}\Gamma_{7v}} & H_{\Gamma_{7c}\Gamma_{8v}} & H_{\Gamma_{7c}\Gamma_{6c}} & H_{\Gamma_{7c}\Gamma_{8c}} & H_{\Gamma_{7c}\Gamma_{7c}} \end{pmatrix}, \tag{2.26}$$

where the double group notation introduced in Section 2.1 assures the invariance of the total Hamiltonian under all symmetry operations (theory of invariance). The advantage of this approach is due to the fact that one can decide - using symmetry arguments - which term vanishes in $H_{14\times14}$. Every H_{ij} within Equation (4.3) can be obtained through an expansion of invariants I_l^{ij} - i.e. those Bloch functions which are invariant under particular symmetry operations - weighted by expansion coefficients a_l^{ij}, as:

$$H_{\mathrm{ij}} = \sum_l a_l^{ij} I_l^{ij}. \tag{2.27}$$

Figure 2.5 shows a scheme of the CBs and VBs obtained from the extend Kane model together with all the momentum matrix elements (P, P', Q, Δ^-), SO-energies (Δ_0, Δ_0') and energy gaps (E_0, E_0'). These terms - which are of higher order in $\boldsymbol{k}$ - are obtained exactly by solving the EFA Hamiltonian in Equation (2.24), depend on the considered material and are also important in the determination of the bulk inversion asymmetry (BIA) and structural inversion asymmetry (SIA) spin-splitting presented later in Section 2.3. For Ge, the symmetry of the diamond crystal leads to $P' = \Delta^- = 0$ and results in absent BIA spin splitting [46]. The coupling with the remote bands is instead described by the Wermann-Weisbuch (C_r and C'_r, for the coupling with CBs) and the reduced Luttinger parameters ($\gamma'_1, \gamma'_2, \gamma'_3$, κ' for the coupling with the VBs) [49]. For clarity, these reduced parameters are corrections to the Luttinger's Hamiltonian $H_\mathrm{L}(\gamma_1, \gamma_2, \gamma_3, \kappa)$, which is often used to obtain the energy dispersion of the VBs [39].

2.1.2 The heavy and light hole bands

Figure 2.5 shows the splitting of the topmost VB in heavy hole (HH), light hole (LH) and split-off (SO) bands. Within the $\boldsymbol{k} \cdot \boldsymbol{p}$-method and the EFA an analytical expression for the HH- and LH-bands is given by [45, 39, 47]:

$$E_\mathrm{HH,LH} = -Ak^2 \pm [B^2k^4 + C^2(k_x^2k_y^2 + k_y^2k_z^2 + k_z^2k_x^2)]^{1/2}, \tag{2.28}$$

where the coefficients A, B and C can be written as a function of the Luttinger paramaters which are listed for different semiconductors [39]. Constant energy surfaces obtained from Equation (2.28) are depicted in Figure 2.6 (a) and are referred to as *warped* spheres. This proves that electronic properties of SCs, such as the effective mass and therefore the mobility in Equation (2.10), depend on the considered direction. According to the definition in Equation (2.8), since the effective mass is proportional to the inverse of the second derivative of the energy dispersion, a steeper energy dispersion corresponds to lighter effective masses. By considering $k \| (100)$ and substituting Equations (2.28) into Equation (2.8), the effective mass for the HH- and LH-bands are:

$$m^*_\mathrm{HH} = \frac{\hbar^2}{2}\frac{1}{(-A+B)} \quad \text{and} \quad m^*_\mathrm{LH} = \frac{\hbar^2}{2}\frac{1}{(-A-B)}. \tag{2.29}$$

Since experimentally $B < A$, one obtains that $m^*_\mathrm{HH} > m^*_\mathrm{LH}$ which justifies the definition of heavy and light hole bands.

2.1.3 Strain effects for HHs and LHs in germanium

The strain can modify the periodicity of the crystal by changing the relative distance between atoms in a certain direction. This change affects the band structure and,

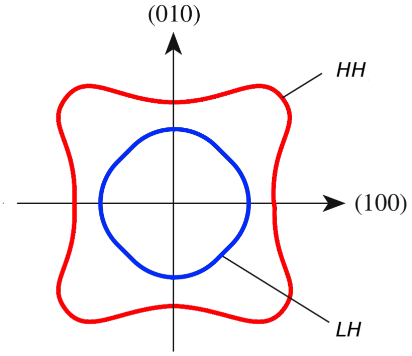

Figure 2.6: Constant energy surface obtained from Equation (2.28) for HH and LH. These warped spheres indicate that transport properties, as effective mass and then mobility, change along different directions.

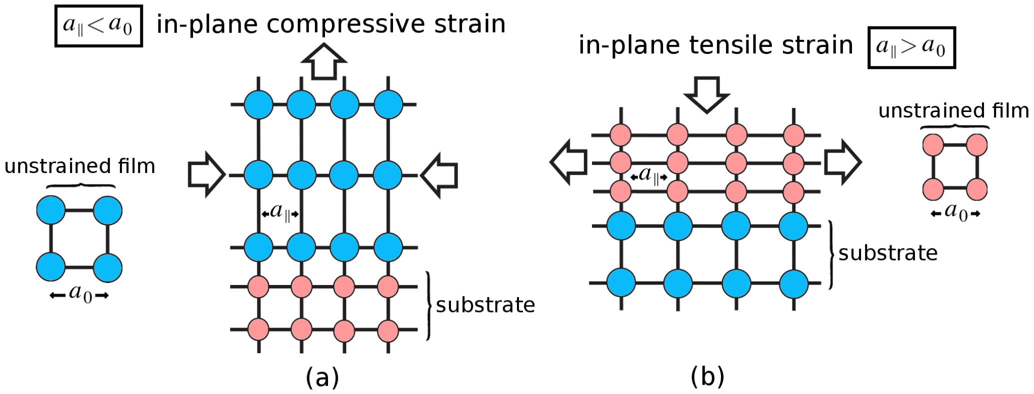

Figure 2.7: Example of in plane compressive (**a**) and tensile (**b**) strain due to the lattice mismatch between a film with lattice constant a_0 and a substrate with in-plane lattice constant $a_\parallel$.

therefore, the effective mass and mobility within a crystal.

Strain tensor. The strain due to the lattice constant mismatch can be explained by referring to Figure 2.7. For instance, by depositing cubic structure materials with lattice constants a_0 onto a substrate with an in-plane lattice constant $a_\parallel$, the deposited material will adapt its structure giving rise to a strained film. The in-plane biaxial strain is considered by means of the related component of the strain tensor:

$$\epsilon_\parallel = \frac{a_\parallel - a_0}{a_0}. \tag{2.30}$$

In relation to the smaller or higher lattice constant of the substrate, the strain can be distinguished between in-plane biaxial *compressive* ($\epsilon_\parallel < 0$) in Figure 2.7 (a) and biaxial *tensile* ($\epsilon_\parallel > 0$) strain in Figure 2.7 (b), respectively. In the following, the in-plane direction refers to the plane orthogonal to the (001) direction, such that $\epsilon_\parallel = \epsilon_{xx} = \epsilon_{yy}$.

Fischetti and Laux theoretically investigated the effects of strain on the band structure of Ge by means of the so called *nonlocal pseudopotentials* (NPP) [50]. This is a correction to the PP method which leads to more accurate results. In fact, the NPP method takes into account that the pseudopotential must be perceived differently by electrons with different angular momentum. The pseudopotential form factor, in their work, takes into account the effect of the *deformation potential* due to the strain, i.e. a deformed potential related to the strained crystal scructure. The obtained energy bands for Ge, at $k = 0$ and as a function of the lattice mismatch, is reported later in Section 3.4.1 in order to present the samples characterised in this thesis. The strain results in degeneracy removal with split HH- and LH-bands for both compressive ($a_{\|}/a_0 < 1$) and tensile strain ($a_{\|}/a_0 > 1$). Beside this splitting, strain also lowers the HH effective mass as shown in Figure 2.8 (a).

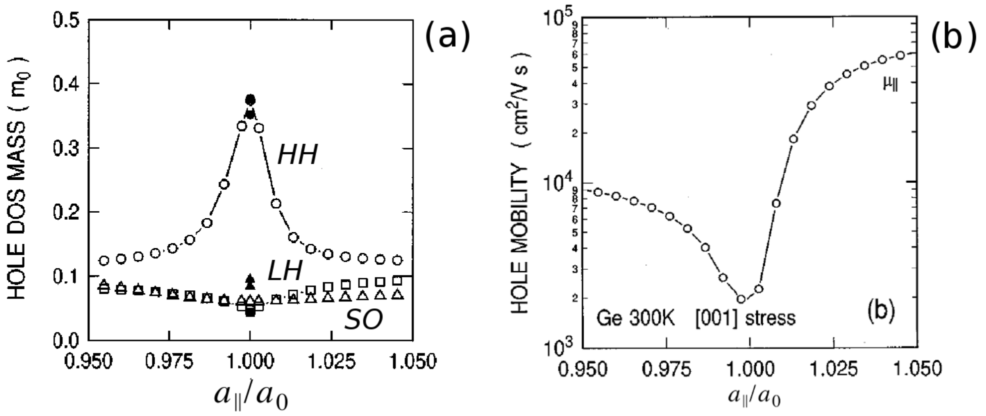

Figure 2.8: (**a**) Decreasing of the DOS effective masses in Ge for compressive and tensile strain. (**b**) Increasing of hole mobility at room temperature in Ge. (Adapted from [50]).

The broken degeneracy of the VBs leads to a lower interaction between holes in HH- and LH-band (intervalley scattering). The combination of lower effective mass and longer lifetime, as reported in Figure 2.8 (b), results in an improved hole mobility for both compressive and tensile in-plane strain. This, as outlined in Section 1.2.1, has been extensively exploited to increase the speed of electronic devices in CMOS-technology.

Detailed band-calculations for the VBs in Ge - for different crystal directions and by also considering the effect of strain - are presented later in Section 6.1.

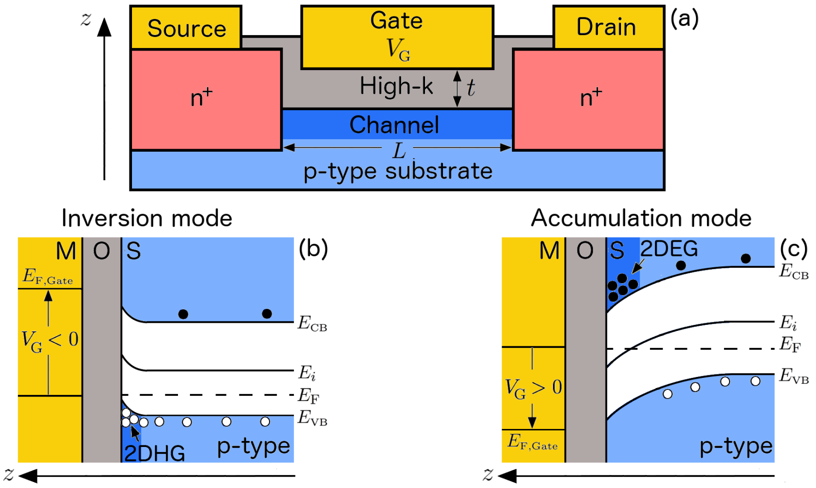

Figure 2.9: (**a**) scheme of a p-type MOSFET. (**b**) inversion mode. (**c**) accumulation mode.

2.2 Two-dimensional systems

As outlined in Chapter 1, 2D-systems are widely used for the realisation of devices in CMOS technology. Generally speaking, the advantage of confining carriers, in one or more dimensions, is linked to the possibility of altering the band gaps as well as transport properties.

Metal-Oxide-Semiconductor. The building-block of the most common devices in CMOS-technology (such as memories and microprocessors) is the metal-oxide-semiconductor field-effect transistor (MOSFET). The general structure of a MOSFET is depicted in Figure 2.9(a). This is a three terminal device which consists of source, gate and drain contacts. The body is formed by a lightly-doped substrate while the source and the drain contact heavily-doped regions with opposite doping to that of the substrate. The main purpose of a MOSFET is allowing, or not, the creation of a conductive 2D-channel between the source and the drain by applying a gate voltage V_G. The 2D-channel is formed at the oxide-semiconductor interface and can be easily understood by considering the band structure of the active area of a MOSFET, that is the metal-oxide-semiconductor capacitor (MOS).

At the equilibrium, the chemical potential (or Fermi energy) assumes the same value within the gate and the substrate ($E_F = E_{F,Gate} = E_{F,Sub}$). As shown in Figure 2.9(b,c), by applying V_G, the Fermi energy assumes different values in the gate and p-type substrate, leading the VB and CB to bend upwards, or downwards, depending on the sign of V_G. If V_G is positive, when $E_{F,sub}$ crosses the VB, the MOS is in the *accumulation* mode and a 2DHG-channel is formed between the source

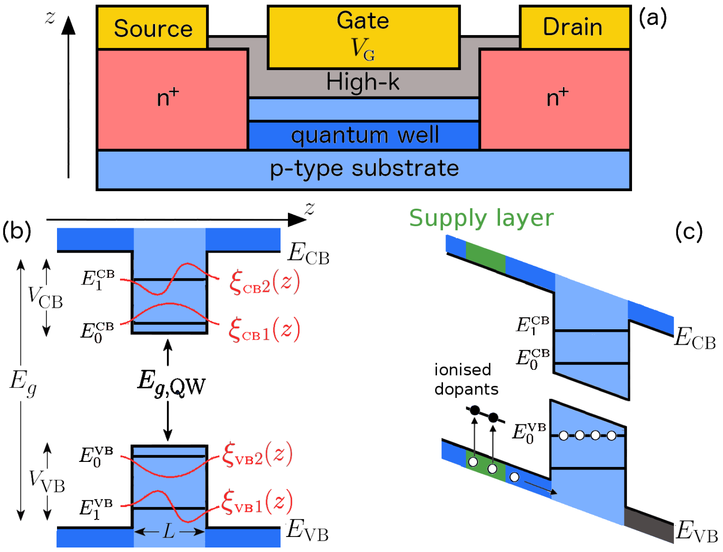

Figure 2.10: (**a**) scheme of a QW-FET. (**b**) square QW. (**c**) Modulation doped QW.

and drain. Viceversa, by applying a negative V_g, the creation of a 2DEG-channel is achieved as soon as $E_{F,sub} > E_i$, with $E_i = E_G/2 = (E_{CB} - E_{VB})/2$. In this latter case the MOS is said to be in *inversion* mode. Note that inversion and accumulation modes are inverted in n-type MOSFET, i.e. one needs a positive $V_G > 0$ to obtain the inversion mode and then the formation of a 2DHG-channel for a n-doped substrate.

As outlined in Section 1.1, the main aim of the Si-CMOS industry is to reduce the size of MOSFETs - the channel length L and the oxide thickness t in Figure 2.9(a) - in order to integrate more MOSFETs in the same area, leading to higher storage capability or faster devices whilst maintaining the cost.

Quantum wells. In Section 1.1.1 the quantum well FET (QW-FET)[21] has been introduced as an alternative device to maintain Moore's law. A scheme of a QW-FET is depicted in Figure 2.10(a). The QW channel is buried and far from the gate oxide, leading to reduced scattering and recombination with surface traps. Furthermore, as generally QWs are made of undoped material, the scattering with dopants is absent. While the characterisation of normal MOSFETs requires the creation of the whole device in order to evaluate the mobility, in QWs this can be straightforwardly obtained by using a Hall bar (see Figure 2.20) or, as presented in the following thesis, by optical methods such as THz-TDS which can evaluate the mobility of bare samples without the need for any further post-deposition processes.

Moreover, characterising QWs gives an estimation of their intrinsic mobility, i.e. not affected by other mechanisms related to the realisation of the QW-FET.

Figure 2.10(b) shows the main example of quantum confinement, namely square-QWs. Square-QWs are obtained from a double junction of a certain material sandwiched by a different material with a similar lattice constant to that of the QW but with a higher energy gap. This, as in the case of the MOS structure, creates an energy potential which confines carriers along the z-direction but allows motion along the xy-plane. Generally carriers are provided - so called *modulation doping* (MOD) - by a thin doped layer created at a certain distance from the QW, see Figure 2.10(c) in the case of p-doped QWs. Since the dopant atoms remain ionised after the carriers are confined within the QW, the resulting electric field bends the CB and VB. This condition is referred to as *structural inversion asymmetry* (SIA). Section 2.3 will introduce SIA as responsible for spin-splitting at zero magnetic fields.

Beside the mobility enhancement due to the increased energy difference between close bands in 2D, a further result of quantum confining is the chance to manipulate the energy gap in relation to the QW thickness. As in the case of single atoms, the confined carriers present, as depicted by red lines in Figure 2.10(b,c), quantised energy states which are higher (for the CB) or lower (for the VB) than states of bulk materials.

2.2.1 Band-structure in quantum wells

Effective mass approximation. To describe the effects of confining carriers along a certain crystallographic direction, a convenient approach relies on using the *effective mass approximation* (EMA). This considers a second-order Löwdin perturbation theory for a nondegenerate, isotropic and parabolic band. Along the EMA, electrons in the m-th band are treated as free particles but, as a consequence of the crystal periodicity, with an *effective mass* m_m^* and *effective g-factor* g_m^*. With these assumptions, the Hamiltonian in Equation (2.24) becomes the so called *effective-mass Hamiltonian* which reads [46]:

$$H = \frac{(-i\hbar\nabla + e\boldsymbol{A})}{2m_m^*} + V(\boldsymbol{r}) + \frac{g_m^*}{2}\mu_B \boldsymbol{\sigma} \cdot \boldsymbol{B}. \tag{2.31}$$

Note that the index m indicates the particular band of the bulk material (such as the HH- or LH-bands).

2D-systems. In order to describe a 2D-system, one can assume a potential along the z-direction, $V(\boldsymbol{r}) = V(z)$, which gives rise to an electric field $\mathcal{E}_z = -dV(z)/dz$. Without any further assumptions on $V(z)$, and by considering $\boldsymbol{B} = 0$, the n-th solution of Equation (2.31) is the following wave function [46]:

$$\psi_{mn\boldsymbol{k}_\parallel}(\boldsymbol{r}) = \eta_{mn}(x)\chi_{mn}(y)\xi_{mn}(z) = \frac{\mathrm{e}^{i\boldsymbol{k}_\parallel \cdot \boldsymbol{r}_\parallel}}{2\pi}\xi_{mn}(z), \tag{2.32}$$

with the respective *subband energy*:

$$E_{mn}(\boldsymbol{k}_\parallel) = E_{mn} + \frac{\hbar^2 k_\parallel^2}{2m_m^*}. \tag{2.33}$$

Here $\boldsymbol{k}_\parallel = (k_x, k_y, 0)$, $\boldsymbol{r}_\parallel = (x, y, 0)$ and $\eta_{mn}(x), \chi_{mn}(y), \xi_{mn}(z)$ are envelope functions along different directions. Differently from the z-dependent term in the middle equivalence of Equation (2.32), which depends on the shape of the potential, $\eta_{mn}(x)$ and $\chi_{mn}(y)$ are instead plane waves describing *free particles* along the x- and y-direction [45], respectively.

Square wells. An expression for the term E_{mn} in Equation (2.33) can be obtained by considering a specific potential $V(z)$. This, for instance, can be a square potential, as in the case of the QW in Figure 2.10 (b). Here $V(z)$ can be either the energy difference between the conduction band of the barriers and of the quantum well, or the energy difference between the valence bands, see V_{CB} and V_{VB}. By assuming $V(-L/2) = V(L/2) = \infty$, an expression for the dispersion relation within the QW can be obtained. This reads [1]:

$$E_{mn}(\boldsymbol{k}_\parallel) = \frac{\hbar^2}{2m_m^*}\left(\frac{n\pi}{L}\right)^2 + \frac{\hbar^2 k_\parallel^2}{2m_m^*}. \tag{2.34}$$

The above energy dispersion results in a quantisation of the bulk energy states α in confined states with energy difference $\Delta E \propto (2n+1)$. Moreover, for $n = 1$ the energy of the CB is increased while the VB energy is decreased. This leads to the possibility of tuning the QW's energy gap with the thickness L. A further important consideration concerns the wave functions $\xi_{mn}(z)$, depicted in red for both CB- and VB-subbands. In the case of an infinite square potential the envelope functions result to be zero at $z = -L/2, L/2$ while, in reality, they penetrate the region of the surrounding semiconductor. Equation (2.34) is widely used for modelling experiment results and it will be used in Chapters 4 and 5 for the calculation of the Landau levels.

2.2.2 Density of states and Fermi energy in 2D.

A general definition of the DOS has been presented in Section 2.1. Contrary to the case of free electron model in 3D, the Fermi energy in 2D defines a circle in the reciprocal space given by πk_{F}^2. By considering $g^{2D}(k_{\|}) = 2/(2\pi)^2$ and the parabolic energy dispersion for free carriers - such that $k = (2m^*E/\hbar^2)^{1/2}$ - the number of states at a certain energy E is:

$$G(E) = g^{2D}(k_{\|}) \times \pi k_{\mathrm{F}}^2 = \frac{m^*E}{\pi\hbar}, \tag{2.35}$$

while the respective DOS is:

$$g^{2D}(E) = \frac{dG(E)}{dE} = \frac{m^*}{\pi\hbar}. \tag{2.36}$$

From Equation (2.6) at $T = 0$, the density of confined carriers in 2D is given by:

$$N_s = \int_0^{E_{\mathrm{F}}} g^{2D}(E)dE = \frac{m^*E_{\mathrm{F}}}{\pi\hbar}. \tag{2.37}$$

This equation is widely used to estimate (by knowing N_s) the Fermi vector and energy which are, respectively, given by:

$$k_{\mathrm{F}}^{\mathrm{2D}} = \sqrt{2\pi N_s} \quad \text{and} \quad E_{\mathrm{F}} = \frac{\hbar^2\pi N_s}{m^*}. \tag{2.38}$$

The relation between the sheet density and Fermi wavevector will be used in Chapter 4 to evaluate the Rashba spin-splitting energy (which will be introduced in the next section), while the density-dependence of E_{F} will be used to model the experimental cyclotron resonances in Chapters 4 and 5.

2.3 Spin-split states at B=0 in 2D-systems

Section 2.1.1 described the importance of symmetry considerations and SOI in calculating the band structure of semiconductors in order to model experimental data. However, the bulk calculation presented so far did not distinguish the intrinsic spin of carriers (s) and the presented energy dispersions considered $E(\boldsymbol{k}_\downarrow) = E(\boldsymbol{k}_\uparrow)$. Generally spin-split states can be resolved by applying an external magnetic field which, because of the Zeeman effect, removes spin-degeneracy and increases (decreases) the energy of spin-up (spin-down) states. The effect of the Zeeman splitting will be discussed later in Section 2.5. The following describes the spin-splitting of energy states in 2D-systems due to an effective, intrinsic, magnetic field arising when carriers move in an inversion-asymmetric potential [46].

Within the theory of invariance, by means of Equation (2.27), one can describe the Hamiltonian matrix elements of the extended Kane-model in order to implicitly consider the symmetric properties of Bloch-functions. The inversion-asymmetric potential can be due to: i) the intrinsic asymmetry of the crystal (as in zincblende structures) and defined as bulk inversion asymmetry (BIA) or ii) the asymmetry of a confining potential - as in modulation doping quantum wells or at interfaces - and defined as structural inversion asymmetry (SIA) which, interestingly, can be also tuned by external electric fields [46, 51]. By following Winkler [46] to calculate the effects of BIA and SIA on a particular band ($i = j$), it is fundamental to also consider the mutual coupling between different bands ($i \neq j$). By exploiting the theory of invariance, the effect of SIA and BIA are considered by adding, in the total Hamiltonian, the respective matrix elements which can be expressed as:

$$H_{\mathrm{ij}}^{\mathrm{BIA}} = \sum_l b_l^{ij} \mathcal{B}_l^{ij} \quad \text{and} \quad H_{\mathrm{ij}}^{\mathrm{SIA}} = \sum_l r_l^{ij} \mathcal{E}_z \mathcal{R}_l^{ij}. \tag{2.39}$$

These are expanded in terms of l invariants, $\mathcal{B}_l^{ij}$ and $\mathcal{R}_l^{ij}$, which are usually obtained by a third-order perturbation theory, and weighted by the BIA and SIA coefficients b_l^{ij} and r_l^{ij}, respectively. Note that the above expansion for $H_{\mathrm{ij}}^{\mathrm{SIA}}$ requires a dependence on the electric field $\mathcal{E}_z$.

Bulk inversion asymmetry. For the BIA in 2D-systems confined along the [001] direction, the matrix elements in Equation (2.39) are weighted by:

$$b^{ij} \propto PP'Q. \tag{2.40}$$

This proportionality is obtained by means of the $\boldsymbol{k} \cdot \boldsymbol{p}$-method for the quantum well subbands. Interestingly, for all kind of bands the BIA coefficient depends on the product $PP'Q$. This leads to the same order of magnitude for the BIA spin-splitting for 2DEGs and 2DHGs. Because of its dependence on P', BIA spin-splitting is absent in diamond structures (as the parity conservation requires $P' = 0$, see page 18). Furthermore, as the matrix elements describe the coupling between different bands - which can be varied with strain - the magnitude of the BIA is expected to be strain-dependent. Since the BIA spin-splitting is not relevant within this thesis (as Ge is centrosymmetric) it will not be considered further. Detailed expressions for the expansion coefficients b^{ij} can be found in [46], together with the calculated

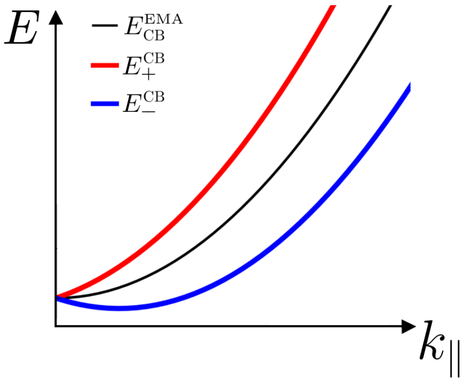

Figure 2.11: Comparison between the energy dispersion for 2DEGs without SIA (black line) and with SIA (blue line for spin-down and red line for spin-up) from Equation (2.44).

k-dependence of the BIA spin-splitting which is cubic in k^3.

Structural inversion asymmetry. A general expression for the SIA Hamiltonian is [52, 46]:

$$H_{\mathrm{ij}}^{\mathrm{SIA}} = r^{ij} \boldsymbol{\sigma} \cdot \boldsymbol{k} \times \boldsymbol{\mathcal{E}}. \tag{2.41}$$

This is essentially an SO-coupling as in Equation (2.15) and, by including the electric field strength within r_{ij}, it is often defined as $H_{ij}^{\mathrm{SIA}} = (r^{ij}/\hbar)(\boldsymbol{z} \times \boldsymbol{p}) \cdot \boldsymbol{\sigma}$ [51]. The following thesis investigated 2DHGs within strained germanium QWs, therefore, it is necessary to highlight how the SIA differently affects 2DEGs and 2DHGs.

Using the theory of invariance for electrons in Γ_{6c}, the expansion in Equation (2.39) leads to:

$$H_{6c6c}^{\mathrm{SIA}} = r^{6c6c} \mathcal{E}_z i(k_- \sigma_+ - k_+ \sigma_-) = r^{6c6c} \mathcal{E}_z \begin{pmatrix} 0 & ik_- \\ -ik_+ & 0 \end{pmatrix}. \tag{2.42}$$

Here the matrix form is obtained with $k_\pm = k_x \pm ik_y$ and $\sigma_\pm = 1/2(\sigma_x \pm i\sigma_y)$. Beside the linear dependence on the electric field $\mathcal{E}_z$, the SIA significantly differs for different bands. For 2DEGs in Γ_{6c}, expansion coefficients depend on the considered subband [46]. This, by means of the 8×8 Kane model for the lowest subband, results in:

$$r^{6c6c} \propto eP^2 s_{\mathrm{QW}}, \tag{2.43}$$

where s_{QW} is a factor which depends on the shape of the quantum well. In contrast to the BIA, $P' = 0$ does not exclude SIA effects in the conduction band for centrosymmetric crystals.

By adding this SIA term H_{6c6c}^{SIA} in Equation (2.42) into the EMA Hamiltonian in Equation (2.31) (without any magnetic fields) the energy dispersion, and the spin-

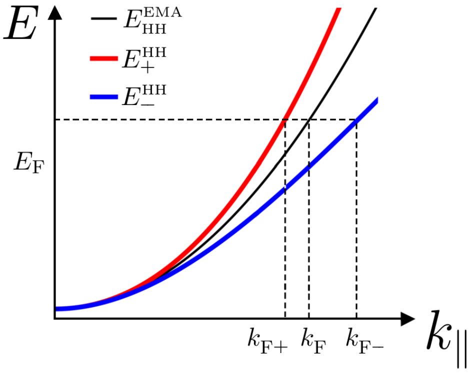

Figure 2.12: Comparison between the energy dispersion for 2DHGs in HH-band without SIA (black line) and with SIA (blue line for spin-down and red line for spin-up) from Equation (2.48). At the Fermi energy E_{F} the two spin-split subbands have different Fermi vector $k_{\mathrm{F}\pm}$ resulting in spin-split density as in Equation (2.50).

splitting energy, for 2DEGs results:

$$E_{\pm}^{\mathrm{CB}}(\boldsymbol{k}_{\|}) = E_{\mathrm{CB}}^{\mathrm{EMA}} \pm \alpha k_{\|} \qquad \text{and} \qquad \Delta_{\mathrm{CB}} = \alpha k_{\| } \tag{2.44}$$

respectively, where $E_{\mathrm{CB}}^{\mathrm{EMA}}$ is, as in Equation (2.33), for any n-th subband. The term $\alpha = \langle r^{6c6c}\mathcal{E}_z \rangle$ is the *Rashba coefficient* for the conduction band and considers the average value of $r^{6c6c}\mathcal{E}_z$ for the two materials at the interface. The main result of the SIA spin-splitting, for the 2DEG's energy dispersion in Equation (2.44), is the linear dependence on $k_{\|}$. An example of SIA spin-split bands, and a comparison with the degenerate dispersion of Equation (2.33), is shown in Figure 2.11.

2.3.1 Structural inversion asymmetry for HHs and LHs

The $H_{\mathrm{ij}}^{\mathrm{SIA}}$ in Equation (2.39) for the VBs Γ_{8v}, by means of third-order perturbation theory and considering $\boldsymbol{\mathcal{E}} = (0, 0, \mathcal{E}_z)$, contains three different expansion coefficients r_l^{8v8v} [46]. Along these, the strongest term for HHs and LHs are:

$$r^{8v8v} = -\frac{eP^2}{3E_0^2} + \frac{eQ^2}{9}\left[\frac{10}{E_0'^2} - \frac{7}{(E_0' + \Delta_0')^2}\right], \tag{2.45}$$

with the matrix:

$$H_{8v8v}^{\mathrm{SIA}} = r^{8\mathrm{v}8\mathrm{v}}\mathcal{E}_z \begin{pmatrix} 0 & \frac{i\sqrt{3}}{2}k_- & 0 & 0 \\ -\frac{i\sqrt{3}}{2}k_- & 0 & -ik_- & 0 \\ 0 & -ik_+ & 0 & \frac{i\sqrt{3}}{2}k_- \\ 0 & 0 & -\frac{i\sqrt{3}}{2}k_- & 0 \end{pmatrix}. \tag{2.46}$$

While for LHs this Hamiltonian can be simplified, as in the case of electrons in the CB, for HHs one obtains [53]:

$$H_{\text{HH}}^{\text{SIA}} = r^{8\text{v}8\text{v}}\mathcal{E}_z i(k_+^3\sigma_- - k_-^3\sigma_+). \tag{2.47}$$

Again, by adding the relative SIA-Hamiltonian in Equation (2.31), the associated energy dispersions for the HH and LH bands result:

$$E_\pm^{\text{HH}}(\boldsymbol{k}_\parallel) = E_{\text{HH}}^{\text{EMA}} \pm \beta_{\text{HH}} k_\parallel^3 \quad \text{and} \quad E_\pm^{\text{LH}}(\boldsymbol{k}_\parallel) = E_{\text{LH}}^{\text{EMA}} \pm \beta_{\text{LH}} k_\parallel, \tag{2.48}$$

where $\beta_{\text{HH}} = \langle r^{8\text{v}8\text{v}}\mathcal{E}_z\rangle$ and β_{LH} are the *cubic Rashba coefficient* for the HH-bands and the linear Rashba coefficient for the LH-bands, respectively, with associated spin-splitting energy:

$$\Delta_{\text{HH}} = \beta_{\text{HH}} k_\parallel^3 \quad \text{and} \quad \Delta_{\text{LH}} = \beta_{\text{LH}} k_\parallel. \tag{2.49}$$

From the above expressions, as the former is cubic in $k_\parallel$, the splitting for HH-subbands clearly differs from the one in the LH-subbands. The linear dependence is equivalent to the one of electrons in CB, in agreement with $m_{j,\text{CB}} = m_{j,\text{LHs}} = \pm 1/2$. As previously for 2DEG, Figure 2.12 shows the energy dispersion affected by the cubic SIA for HHs in 2D. Since k depends on the carrier density within a quantum well, it is worth noting that the linear splitting is then important at lower density, whereas at higher density the cubic dependence becomes dominant. However, by introducing holes within a quantum well, the first occupied energy states are the HH-subbands and, as in the case of SIA for 2DEGs, the effect of the Rashba spin-splitting depends on the particular subband m [46].

Spin-split density. By still referring to Figure 2.12, for $E = E_{\text{F}}$ the two spin-split subbands correspond to two different Fermi wavevectors $k_{\text{F}\pm}$. These define the density for spin-up and spin-down states, that are $N_\pm = k_{\text{F}\pm}^2/4\pi$ [46]. By considering that $E_{\text{F}} = E(k_{\text{F}+}) = E(k_{\text{F}-})$ and $N_s = N_+ + N_-$ the spin-split densities can be written as a function of the cubic Rashba coefficient, i.e.:

$$N_\pm = \frac{N_s}{2} \mp \frac{2m_{\text{HH}}^* N_s}{\hbar^2\sqrt{2X}}\beta_{\text{HH}}\sqrt{\pi N_s(6 - 4/X)}, \tag{2.50}$$

with:

$$X = 1 + \sqrt{1 - 4\pi N_s(2m_{\text{HH}}^*\beta/\hbar^2)^2}. \tag{2.51}$$

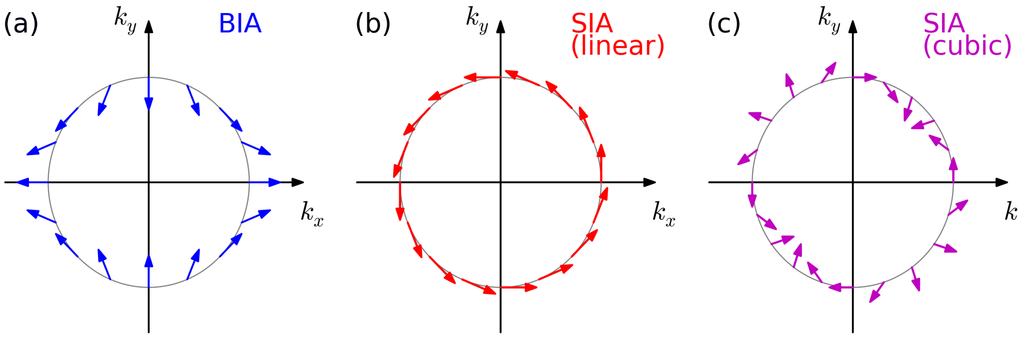

Figure 2.13: Effective magnetic fields in Equations (2.53), (2.54) and (2.55) for the BIA (**a**), linear SIA for electrons and LHs (**b**) and cubic SIA for HHs (**c**). Gray circles are constant energy surfaces at the Fermi energy.

Vice versa, by knowing the two spin-split densities $N_\pm$, it is possible to estimate the cubic Rashba coefficient through:

$$\beta_{\mathrm{HH}} = \sqrt{\frac{2}{\pi}} \frac{\hbar^2}{2m^*_{\mathrm{HH}}} \frac{N_s(N^*_+ - N^*_-) + \Delta N(N^*_+ + N^*_-)}{6N_s^2 + 2(\Delta N)^2}, \tag{2.52}$$

where $\Delta N = |N_+ - N_-|$ and $N^*_\pm = \sqrt{N_s \pm \Delta N}$. This result is used in Chapter 4 to get β_{HH} from the experiments and, therefore, evaluate Δ_{HH} from Equation (2.49).

The effective magnetic field for BIA and SIA. As discussed in Section 2.3, the SOI effects are due to an effective magnetic field experienced by carriers moving inside crystals. Since BIA effects are cubic in k, the related effective magnetic field depends on the crystallographic direction, i.e. the related k, along which the carriers move. For 2D-systems, this critically depends on the confining direction (z-axis) and, in the case of $z \parallel [001]$, is given by [54, 28, 55, 51]:

$$\boldsymbol{B}^{\mathrm{BIA}}(\boldsymbol{k}_\parallel) = \frac{\gamma}{\hbar} \langle k_z^2 \rangle \, (k_x, -k_y, 0). \tag{2.53}$$

where γ is the Dresselhaus coefficient related to the BIA expansion coefficient in Equation (2.40) and $\langle k_z^2 \rangle$ is the averaged squared vector along the growth direction which can be varied by changing the quantum well thickness. Conversely, the SIA is due to the electric field $\mathcal{E}_z$ and the coefficient α (for electrons) β_{LH} (for LHs) and β_{HH} (for HHs). For electrons and LHs the effective magnetic field is given by:

$$\boldsymbol{B}^{\mathrm{SIA}}_{e^-}(\boldsymbol{k}_\parallel) = \frac{\alpha}{\hbar}(-k_y, k_x, 0), \quad \text{and} \quad \boldsymbol{B}^{\mathrm{SIA}}_{\mathrm{LH}}(\boldsymbol{k}_\parallel) = \frac{\beta_{\mathrm{LH}}}{\hbar}(-k_y, k_x, 0), \tag{2.54}$$

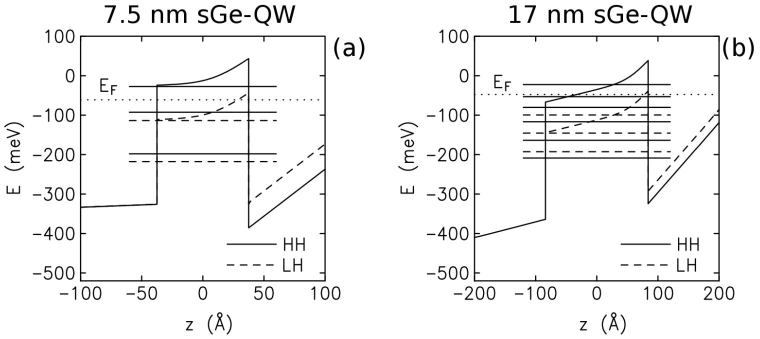

Figure 2.14: (**a,b**) Potential profile along the growth-direction z with relative energy subbands, at $k = 0$, for HHs and LHs within strained Ge-QWs. Reproduced from [57].

respectively. For HHs, as in the case of $\boldsymbol{B}^{\mathrm{BIA}}(\boldsymbol{k}_{\parallel})$, the cubic dependence on $\boldsymbol{k}_{\parallel}$ gives rise to an effective magnetic field which depends on the orientation of $\boldsymbol{k}$ as [56]:

$$\boldsymbol{B}^{\mathrm{SIA}}_{\mathrm{HH}}(\boldsymbol{k}_{\parallel}) = \frac{\beta_{\mathrm{HH}}}{\hbar}(k_y \sin 3\theta, -k_x \cos 3\theta, 0), \tag{2.55}$$

where θ is the angle between $\boldsymbol{k}$ and the k_x-axis. The (k_x, k_y)-dependence of the effective magnetic field is shown in Figure 2.13 where the substantial difference between the linear and cubic Rashba spin-splitting is clearly noticeable. By considering a simple density of states for 2D-systems with respective Fermi surface depicted by coloured circles in Figure 2.13, $\boldsymbol{B}^{\mathrm{SIA}}_{\mathrm{LH}}(\boldsymbol{k}_{\parallel})$ is always parallel to the Fermi surface, whereas $\boldsymbol{B}^{\mathrm{SIA}}_{\mathrm{HH}}$ rotates as 3θ.

Common experiments for the determination of the SIA spin-splitting use the application of an external magnetic field B. Since the effects of B in 2D-systems will be outlined later in Section 2.5, these experiments, and the reported value of $B = 0$ spin-splitting for different systems, will be given later in Section 2.5.2.

2.3.2 2DHGs in strained MOD Ge-QWs

In line with the background presented so far, and since this thesis focuses on the characterisation of strained germanium quantum wells (sGe-QWs), the following describes calculations performed by Winkler *et al.* [57] in order to simulate and interpret CRs data - obtained by means of Fourier transform spectroscopy [58] - for two p-type MOD Ge/SiGe heterostructures (strained Ge-QWs). The following merely outlines the band calculations from Winkler *et al.*, while CRs simulations will be presented later in Section 2.6.1.

Figure 2.14(a,b) shows the self consistent potential profiles, at $k_{\parallel} = 0$, with corresponding subband energies of HHs and LHs. The modulation doping - which

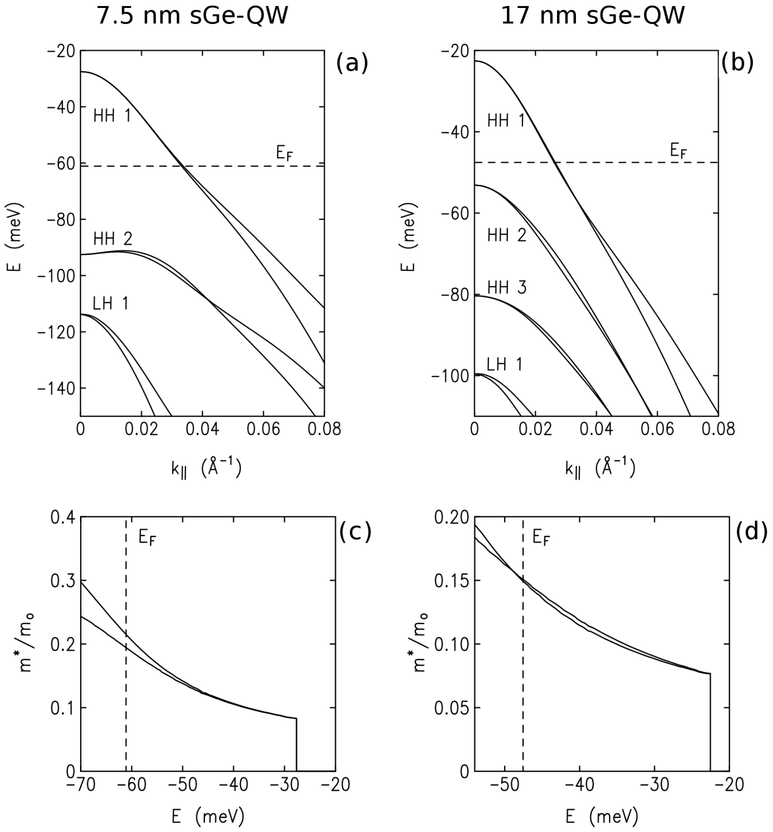

Figure 2.15: (**a,b**) Subband energy dispersion as a function of $k_{\|}$ showing the spin-splitting due to SIA for sGe-QWs in Figure 2.14. (**c,d**) DOS effective mass. Reproduced from [57].

arises from a Ga δ-doping (5×10^{12} cm^{-2}) - results in a bent VB. The related E_{F} is shown as dashed line and its value, related to the hole density within the QW, assures that only the topmost HH-band is occupied in both cases. The energy dispersion, obtained by considering a 6×6 $\boldsymbol{k} \cdot \boldsymbol{p}$ Hamiltonian for the topmost valence bands $\Gamma_{8\mathrm{v}}$ and $\Gamma_{7\mathrm{v}}$, is reported in Figure 2.15(a,b) where spin-split states due to the Rashba effect are clearly noticeable. In both cases, these are resolved at lower $k_{\|}$ for the LH-bands due to the linear dependence on $k_{\|}$ [see Equation (2.48)]. Moreover, as shown in Figure 2.15(c,d), the nonparabolic dispersion leads to an energy dependence of the DOS effective mass.

Cubic Rashba coefficient for HHs in a sGe-QW and strain dependence. One of the approaches that estimates the SIA splitting looks for weak antilocalisation (WAL) features in measuring the magnetoconductivity. An example is given in Figure 2.16(b) for a Ge/Si$_{0.5}$Ge$_{0.5}$-QW reported by Moriya *et al.* [59]. The dif-

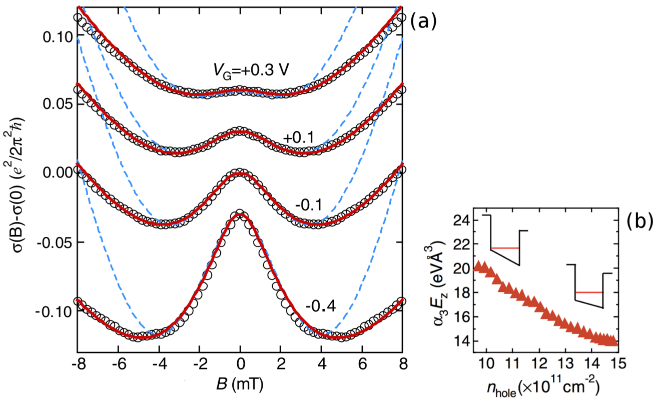

Figure 2.16: (**a**) WAL measurements of 2DHG in a Ge/$\mathrm{Si_{0.5}Ge_{0.5}}$-QW at different gate voltage V_{G}. Coloured lines depict fits considering linear (blue) and cubic (red) SIA spin splitting (see text). (**b**) Density (or V_{G}) dependence of the Rashba coefficient obtained from Equation (2.56). Reproduced from [59].

ference between the conductivity σ_{xy} at $B = 0$ and the one measured at low-B is plotted, as a function of B, at different gate-voltages V_{G}. By increasing V_{G} towards positive values, WAL-features disappear, as the electric field assures the reduction of SIA [60]. Red and dashed-blue curves depict fits obtained by considering a model for the cubic- and linear-SIA, respectively. Fit parameters are the SIA effective magnetic field given in Equation (2.54) for LHs, and Equation (2.55) for HHs. The disagreement of the blue fits with data confirms the dominance of the cubic SIA spin-splitting of HHs in Ge-QWs (as outlined in Section 2.3.1).

Figure 2.16(b) reports the change in the evaluated $\beta_{\mathrm{HH}} = a_3\mathcal{E}_z$ as a function of the HH-density modulated by V_{G}. Here $a_3 \equiv r^{8v8v}$ and $E_z \equiv \mathcal{E}_z$ in Section 2.3.1. This term has been evaluated from the fitted SIA effective magnetic field as:

$$\beta_{\mathrm{HH}} = a_3\mathcal{E}_z = \hbar|\boldsymbol{B}^{\mathrm{SIA}}_{\mathrm{HH}}|/(k^{\mathrm{2D}}_{\mathrm{F}})^3. \tag{2.56}$$

The two schemes within the plot depict the change in the shape of the QW. This results in a lower electric field $\mathcal{E}_z$ at at higher V_{G}, in line with the decreasing β_{HH}.

Furthermore, Winkler *et al.* suggested that β_{HH} must have a dependence on the energy difference, $E_{\mathrm{HH}} - E_{\mathrm{LH}}$, between the HH- and LH-bands [53]. The calculation performed by Moriya *et al.*, by means of a Luttinger Hamiltonian and perturbation method proposed by Ohkawa *et al.* [61], resulted in the following dependence on $E_{\mathrm{HH}} - E_{\mathrm{LH}}$ [59]:

$$\beta_{\mathrm{HH}} = \frac{1}{\mathcal{E}_z}\frac{-3e\hbar^4\gamma_3^2}{2m_0^2(E_{\mathrm{HH}} - E_{\mathrm{LH}})^2}. \tag{2.57}$$

Here γ_3 is one of the Luttinger parameters presented in Section 2.1.1, $\mathcal{E}_z$ is the electric field arising from the supply layer, or the gate voltage, and $E_{\mathrm{HH}} - E_{\mathrm{LH}}$ is the energy difference at $k = 0$. Moriya *et al.* pointed out that the change in $E_{\mathrm{HH}} - E_{\mathrm{LH}}$,

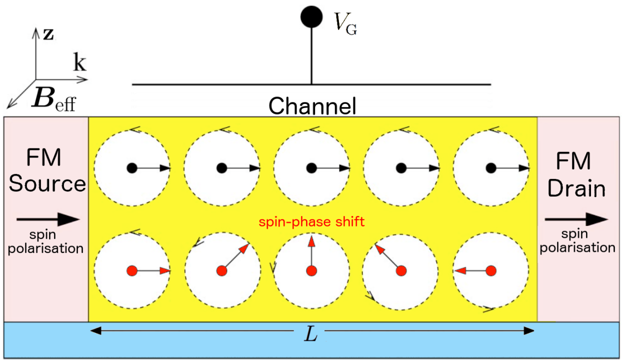

Figure 2.17: Scheme of a spin-FET. The source and drain contacts (pink areas) are ferroelectric materials which inject and detect spin-polarised current. The channel (yellow area) must be chosen in order to allow the flow of a spin-polarised current but also rotate the spin-polarisation in order to avoid any current detection by the drain contact (see text). Adapted from [28]

due to the applied gate voltage, is small compared to the energy separation due to the strain. As outlined in Section 3.4.1 and 2.1.3, this depends on the Ge-content (see Figure 3.4). For compressive strain between 2.1% (Moriya's samples) and 0.8% (samples within this thesis) this energy difference decreases and would result in a increased β_{HH}.

2.4 The application of SIA in spintronics

Insights into the spin-splitting mechanisms due to SIA are fundamental for spintronics [51]. As defined by Žutić and Das: "spintronics is a multidisciplinary field whose central theme is the active manipulation of spin degrees of freedom in solid-state systems" [28]. The following outlines qualitatively the main aims of spintronics: i) finding the right way to generate and control the spin polarisation of carriers; ii) being able to sustain or suppress this polarisation over a certain distance inside materials; iii) detecting the spin-polarisation.

While the spin of carriers is already used in realising magnetic hard disk drives (commercially developed by IBM and based on the giant magnetoresistance effect [28]), one of the most famous ideas in spintronics is the spin field-effect transistor (spin-FET) proposed by Datta and Das in 1990 [62]. A spin-FET scheme is depicted in Figure 2.17 and is reminiscent of the structure of MOSFETs [Figure 2.9(a)] or QW-FETs [Figure 2.10(a)]. The differences in a spin-FET are: i) ferromagnetic source- and drain-contacts and ii) channels which allow the propagation of a spin-polarised current together with the chance to manipulate it by applying a gate voltage. As in ferromagnets (like iron) the density of states for carriers with a certain spin is, at E_{F}, higher than the one of carriers with opposite spin, they can be used to inject and detect a spin-polarised current. Apart from the existence of spin-split states, by referring to Figure 2.17, the main requirement for spin-FET channels is the possibility of sustaining a spin-polarised current (top part of the channel) or depressing it by applying a gate voltage (bottom). This is the case of the SIA spin-splitting in 2D-systems outlined in Section 2.3. As shown in Figure 2.13(b,c) the SIA provides an effective magnetic field which would result in a precession of the carrier's spin along a certain distance L, that is a phase-shift $\Delta\theta(L) = \pi$ in Figure 2.17. From SIA assumptions, Datta and Das obtained the following relation [62]:

$$\Delta\theta = \frac{2m^{*}\phi_{B}(V_{\mathrm{G}})L}{\hbar}, \tag{2.58}$$

where $\phi_B(V_{\mathrm{G}}) \equiv \alpha$ for electrons, β_{LH} for LHs and β_{HH} for HHs, is the electrically tunable Rashba coefficient. Almost 20 years after the idea of Datta and Das, Koo *et al.* demonstrated the control of the spin-precession of a 2DEG within an InAs-QW by means of a gate voltage [63]. As expected from Equation (2.58), at a certain V_{G} the spin-precession resulted in a π-rotation of the spin orientation of a 2DEG and a voltage difference, measured between the two ferromagnetic electrodes, was observed.

As spintronic devices are based on the chance to inject and detect spin polarised carriers, materials are characterised in terms of spin lifetime and diffusion coefficient which define the spin diffusion length. This indicates the scale over which the spin information can be transmitted with negligible loss of spin polarisation [64]. Generally, the range of spin lifetime is ps to μs and is related to the transport lifetime which, in turn, depends on scattering processes with phonon and defects [28].

Elliott-Yafet mechanism (EY). This mechanism assumes that spin-relaxation is due to the SO-coupling with ions in the crystal, owing to a matrix term $V_{\mathrm{SO,ions}} = \hbar^2/mc^2\nabla V_0 \times \boldsymbol{p}\cdot\boldsymbol{\sigma}$ in the Hamiltonian [65], where V_0 is the lattice potential. By considering this further perturbation, carrier's wave functions are described by a mix of spin-up and spin-down states. The $V_{\mathrm{SO,ions}}$ couples states at the same $\boldsymbol{k}$ but with different spin and band indexes, and its combination with the momentum scattering leads to: [28, 59]:

$$\tau_{\mathrm{s}} = \frac{\tau_{\mathrm{tr}}}{(\Delta g)^2}. \tag{2.59}$$

The relation between the spin lifetime τ_{s} and the transport lifetime τ_{tr} scales therefore with $\Delta g = g^{*} - g_0$, where g^{*} is the effective g-factor and $g_0 = 2.022$ is the electron g-factor.

Dyakonov-Perel mechanism (DP). Conversely, this mechanism relies on asym-

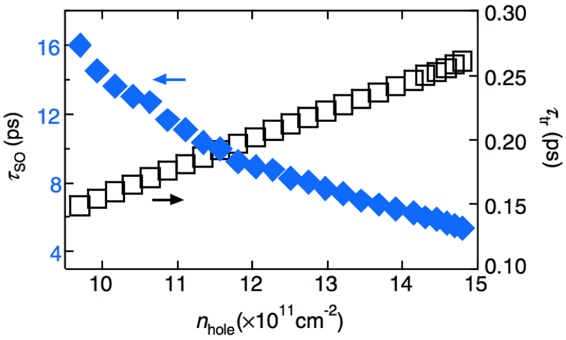

Figure 2.18: Variation of the spin lifetime and transport lifetime for 2DHG in a Ge/$Si_{0.5}Ge_{0.5}$-QW as a function of the hole density (τ_{SO} corresponds to τ_s in the text). Reproduced from [59].

metry assumptions [66] and considers the precession of carriers as a further Hamiltonian term related to the effective magnetic fields in Figure 2.13. Generally, the DP-mechanism is considered in the regime $\tau_s \omega_{\mathrm{eff}} \leq 1$, i.e. when carriers are scattered before completing a full precession around the effective magnetic field $\boldsymbol{B}_{\mathrm{eff}}$ with intrinsic effective Larmor frequency ω_{eff} [28]. The main result is the inverse proportionality in respect of the SIA, or BIA, spin-splitting energy Δ, as well as to τ_{tr}, i.e. [59]:

$$\tau_s \propto \frac{1}{\Delta \tau_{\mathrm{tr}}}. \tag{2.60}$$

Spin lifetime for 2DHG in a sGe-QW. In Section 1.2 experimental values of diffusion and spin lifetime were summarised for bulk Ge which have been linked to the EY-mechanism due to the centrosymmetric structure of Ge. Differently from the bulk case, as the DP-mechanism is related to the SIA [28], in MOD Ge-QWs both mechanisms can contribute to the spin lifetime. From the WAL measurements outlined in the previous section for 2DHG in a sGe-QW, Moriya *et al.* obtained a comparison between τ_s and τ_{tr} which is shown in Figure 2.18. Since the change of the two lifetimes had an opposite behaviour with increasing carrier density, which also enhances Δ, the authors indicated the DP-mechanism as dominant [59].

After estimating τ_{tr} for HHs within the characterised sGe-QWs in Chapter 4, Equations (2.59) and (2.60) will be used in Chapter 4 to qualitatively assign the dominant spin-relaxation mechanism.

2.5 Magnetic field effects in two-dimensional systems

Since generally in 2D-systems the density difference between spin-up and spin-down states is low, it is usually necessary to apply a magnetic field in order to resolve features revealing any contribution for SIA or BIA spin-splitting. As the main goal of this thesis is also the investigation of Rashba spin-splitting, for the argument above, experiments in thesis were performed under the application of a magnetic field. The formalism presented in the following section will be used to perform calculations, as for instance to model the experimentally determined *cyclotron frequencies* later in Chapters 4 and 5. In the classical picture, the application of a magnetic field makes carriers experience an in-plane circular motion - orthogonal to B - characterised by a cyclotron frequency:

$$\omega_{\mathrm{c}} = eB/m^*. \tag{2.61}$$

Therefore, probing cyclotron resonances (CRs) by means of spectroscopic techniques is a direct way to determine the effective mass of electrons (or holes) in solids. By applying an ac electric field perpendicularly to the magnetic field and with a frequency $\omega = \omega_{\mathrm{c}}$ the carriers can absorb energy from the ac-field. To find the resonance condition, both ω and B can be swept, and the effective mass can be evaluated.

Semi-classical description. To classically describe the motion of electrons in a magnetic field $\mathbf{B}$ and electric field $\mathbf{E}$, a rigorous procedure involves the use of the semi-classical Boltzmann equation to determine the current density $\mathbf{J}$ and the complex conductivity tensor, σ. The current density, resulting from the application of $\mathbf{E}$, has a phenomenological form given by:

$$\mathbf{J} = N_s e\mathbf{v} = \sigma\mathbf{E}, \tag{2.62}$$

Here, N is the carrier density, e is the electron charge and $\mathbf{v}$ is the drift velocity.

The conductivity tensor can be determined by means of the semi-classical Drude-model [67]. The formalism starts by considering the motion of carriers under the application of $\mathbf{B}$ and $\mathbf{E}$, which must obey the equation of motion:

$$m^* \frac{d\mathbf{v}}{dt} + m^* \frac{\mathbf{v}}{\tau} = -e(\mathbf{E} + \mathbf{v} \times \mathbf{B}) \tag{2.63}$$

where τ is the scattering lifetime at the Fermi energy. The effect of the lattice in the carrier's motion is taken into account through m^* and τ, which are considered constant. The drift velocity resulting, for instance, from an applied ac-field $\mathbf{E} = \mathbf{E}_0 e^{-i\omega t}$ in optical experiments, can be written as $\mathbf{v} = \mathbf{v}_0 + \mathbf{v}e^{-i\omega t}$ and Equation (2.63) becomes:

$$\mathbf{v} + \mu^*(\mathbf{B} \times \mathbf{v}) = \mu^*\mathbf{E} \tag{2.64}$$

where the short notation $\mu^* = e\tau^*/m^*$ with $\tau^* = \tau/(1 - i\omega\tau)$ are the complex mobility and complex relaxation time, respectively. For a cubic lattice, by using some vector identities, considering $\mathbf{B} = (0, 0, B_z)$ and substituting Equation (2.64) in Equation (2.62), the optical conductivity tensor results:

$$\sigma = \begin{pmatrix} \sigma_{xx} & \sigma_{xy} & 0 \\ -\sigma_{xy} & \sigma_{yy} & 0 \\ 0 & 0 & \sigma_{zz} \end{pmatrix} \tag{2.65}$$

with:

$$\sigma_{xx} = \sigma_{yy} = \frac{\sigma_0}{\tau} \frac{i\omega - 1/\tau}{(\omega + i/\tau)^2 - \omega_\mathrm{c}^2}, \tag{2.66}$$

$$\sigma_{xy} = -\sigma_{yx} = \frac{\sigma_0}{\tau} \frac{\omega_\mathrm{c}}{(\omega + i/\tau)^2 - \omega_\mathrm{c}^2}, \tag{2.67}$$

$$\sigma_{zz} = \frac{\sigma_0}{\tau} \frac{\tau}{(1 - i\omega\tau)}, \tag{2.68}$$

where $\sigma_0 = N_s e^2 \tau / m^*$ is the DC sheet conductivity. The counterpart of the conductivity tensor is the resistivity tensor:

$$\rho = \begin{pmatrix} \rho_{xx} & \rho_{xy} & 0 \\ -\rho_{xy} & \rho_{yy} & 0 \\ 0 & 0 & \rho_{zz} \end{pmatrix} = \frac{1/\sigma_0}{\sigma_{xx}^2 + \sigma_{xy}^2} \begin{pmatrix} \sigma_{xx} & \sigma_{xy} & 0 \\ -\sigma_{xy} & \sigma_{yy} & 0 \\ 0 & 0 & \sigma_{zz} \end{pmatrix}. \tag{2.69}$$

These quantities can be accessed both electrically, for instance through magnetotransport measurements (Section 2.5.1), or optically as in cyclotron resonance spectroscopy (Section 2.6). In fact, Equations (2.66) and (2.67) will be used later to model experimental data and evaluate N_s, ω_c and τ.

Quantum description. To introduce the effect of the application of a perpendicular B to a 2D-system, it is worth considering the EMA Hamiltonian in Equation (2.31) without the contribution of the Zeeman term and external potential $V(\boldsymbol{r})$, i.e. the case of free electrons with effective mass m^*. In this case, by assuming the gauge $\boldsymbol{A} = (0, Bx, 0)$, one obtains the following Schrödinger equation [39, 44]:

$$-\frac{\hbar}{2m^*}\left[\frac{\partial^2}{\partial x^2} + \left(\frac{\partial}{\partial y} + \frac{ieB}{\hbar}x\right)^2 + \frac{\partial^2}{\partial z^2}\right]\psi(x, y, z) = E\psi(x, y, z). \tag{2.70}$$

As the motion along z - with energy $\hbar^2 k_z / 2m^*$ - is not influenced by B, the eigenstates can be decoupled as:

$$\psi(x,y,z) = \Phi(x,y)\xi(z) = u(x)e^{ik_y y}e^{\pm ik_z z}, \tag{2.71}$$

where the term $\Phi(x,y) = u(x)e^{ik_y y}$ describes the xy-plane motion. The substitution of Equation (2.71) into (2.70) leads to:

$$\left[\left(\frac{-\hbar}{2m^*}\right)\frac{\partial^2}{\partial x^2} + \left(\frac{m^*}{2}\right)\left(\frac{eB}{m^*}x + \frac{\hbar k_y}{m^*}\right)^2\right]u(x) = E'u(x) \tag{2.72}$$

with $E' = E - E_z$. The Hamiltonian in Equation (2.72) corresponds to a one-dimensional oscillator with frequency $\omega_\mathrm{c} = eB/m^*$, equilibrium position:

$$x_0 = \frac{\hbar k_y}{m^*\omega_\mathrm{c}} = \frac{\hbar k_y}{eB} = k_y {\lambda_c}^2 \tag{2.73}$$

and energies:

$$E' = (\mathcal{N} + 1/2)\hbar\omega_\mathrm{c} \qquad [\mathcal{N} = 1, 2, \ldots, \infty]. \tag{2.74}$$

These energy states are called Landau levels (LLs) while the term $\lambda_c = \sqrt{\hbar/eB}$, in Equation (2.73), is the *magnetic length.* By assuming an area $L_y \times L_x$, the motion along x obeys Equation (2.73) while the periodic boundary conditions along y leads to $k_y = (2\pi/L_y)j$, where j is an integer. Substituting this into Equation (2.73) results in $x_0 = \hbar k_y/(eB) = 2\pi\hbar j/(eBL_y)$ and, as the motion along x requires the condition:

$$0 < \frac{2\pi\hbar j}{eBL_y} < L_x \quad \text{or} \quad 0 < j < \frac{eBL_xL_y}{h}, \tag{2.75}$$

one obtains the allowed number of states per unit area in every LL, which is given by:

$$2n_B = \frac{2eB}{h} = \frac{eB}{\pi\hbar} = \frac{1}{\pi\lambda_c^2}. \tag{2.76}$$

Here, the factor 2 considers the spin-degeneracy. Equation (2.76) can be interpreted as if each LL occupies, in reciprocal space, an area $A_\mathrm{LL} = 2\pi\lambda_c^2 = h/eB$. This decreases on increasing the magnetic field and allows more carriers to occupy the same LL. Such an important result is fundamental in understanding the integer quantum Hall effect (IQHE), which is the quantum counterpart of the classical Hall effect.

2.5.1 Magneto-transport and the quantum Hall effect

By means of magnetotransport experiments, one can explore - with devices such as Hall bars with dimension L_x, L_y depicted in Figure 2.20(c,d) - the longitudinal and transverse resistance, R_{xx} and R_{xy}, respectively, of 2D-systems under the application of a perpendicular $\boldsymbol{B} = (0, 0, B_z)$. In the classical picture - i.e. what happens at room temperature or at low magnetic field - measuring R_{xy} reveals the Hall effect, which consist of the linear relation:

$$\rho_{xy} = R_{xy}/L_x L_y = R_{\mathrm{H}}^C B_z, \quad \text{where} \ \ R_{\mathrm{H}}^C = \frac{E_y}{J_x B_z} = \frac{V_y}{I_x B_z} = -\frac{1}{N_s e} \tag{2.77}$$

is the classical Hall resistance. The Hall effect allows the determination of the 2D density, or *sheet density*, N_s by determining the B-dependent slope of R_{xy}. This is shown, at low magnetic field in Figure 2.19(a), where, conversely, the longitudinal resistance R_{xx} presents a constant value. At low temperature, high magnetic fields, and for material with high carrier mobility, the B-dependence of R_{xy} and R_{xx} deviates from the classical case and, as depicted in Figure 2.19(a), results in the integer quantum Hall effect (IQHE). While R_{xy} is characterised by constant values (plateaux) in certain B-ranges, the latter suddenly increases when R_{xx} has an abrupt change from one plateau to the next. The R_{xx} oscillations with B are known as Shubnikov-de Haas (SdH) oscillations. The coloured vertical lines will be used later as a reference to explain the IQHE.

By knowing N_s, the particularity of the IQHE is obtained by plotting, as in Figure 2.19(b), $(h/e^2)/R_{xy}$ against the so called *filling factor*:

$$\nu = \frac{hN_s}{eB} = N_s/n_B. \tag{2.78}$$

Here the last equality comes from Equation (2.76) and gives the physical meaning of ν. It defines how carriers are distributed between different LLs at a certain B, that is the number of occupied LLs. The blue curve depicts the classical effect for $R_H = R_{\mathrm{H}}^C$ defined in Equation (2.77). In the IQHE, plateaux, at $R_{xy}^{-1} = \nu(h/e^2)$, are centred at B-values such that ν from Equation (2.78) is an integer. The observation of plateaux at these multiples of (h/e^2) does not depend on the particular material or type of carriers forming the 2D-system (electrons or holes).

LLs in quantum wells. In order to explain the IQHE, the magnetic field's influence on the energy dispersion for 2D-systems has to be considered. As outlined in the previous section, energy bands under the influence of B are described in terms

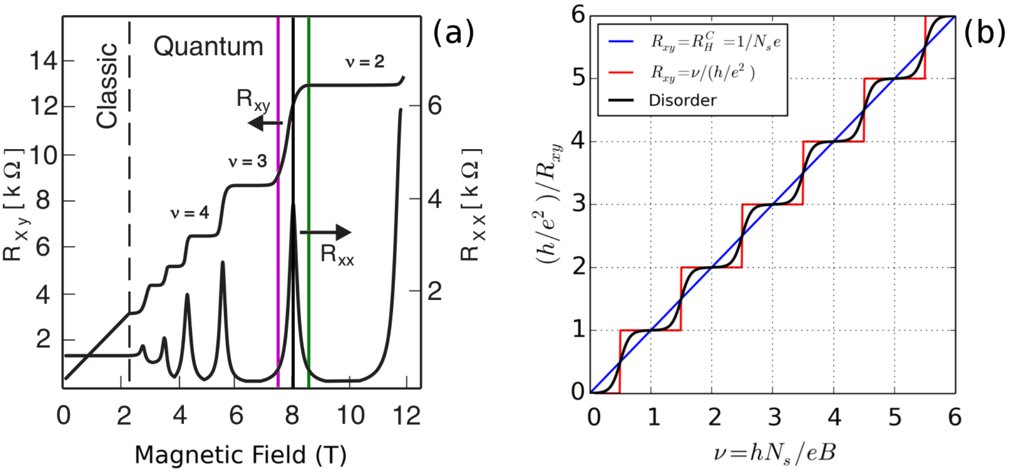

Figure 2.19: (**a**) Difference between the classical and the quantum regime in magneto-transport measurements. At high B the integer quantum Hall effect results in a particular evolution of R_{xx} and R_{xy} (see text). Reproduced from [68]. (**b**) Dependence of R_{xy} with the filling factor ν: in the classical regime (blue line), ideal quantum regime (red line) and ideal regime with considering disorder (black line).

of LLs. In the case of a confined 2D-system, LLs evolve from the quantised energies arising from the confining potential $V(z)$. It is then convenient to introduce the symmetric gauge $\boldsymbol{A} = B/2(-y, x, 0)$ and define the creation and annihilation operators:

$$a^\dagger = \lambda_c k_+/\sqrt{2} \qquad \text{and} \qquad a = \lambda_c k_-/\sqrt{2}, \tag{2.79}$$

repsectively. With these assumptions, the resulting Hamiltonian (EMA) for the bulk band m, and the n-th subbands of the 2D-system, reads:

$$H_{mn\sigma} = -\frac{\hbar}{2m_m^*}\frac{\partial^2}{\partial z^2} + V(z) + E_{mn} + \hbar\omega_c\left(a^\dagger a + \frac{1}{2}\right) + \frac{g_m^*}{2}\sigma\mu_B B. \tag{2.80}$$

$$\psi_{mn\mathcal{N}} = |\mathcal{N}\rangle\,|\sigma\rangle\,\xi_{mn}(z). \tag{2.81}$$

Here $|\mathcal{N}\rangle$ are eigenstates of the operator $aa^\dagger$, such that $aa^\dagger\,|\mathcal{N}\rangle = \mathcal{N}\,|\mathcal{N}\rangle$, with Landau quantum number $\mathcal{N} = [0, 1, \ldots]$. The LLs are then given as:

$$E^{\pm}_{mn\mathcal{N}}(B) = E_{mn}(\boldsymbol{k}_0) + \hbar\omega_c\left(\mathcal{N} + \frac{1}{2}\right) \pm \frac{g_m^*}{2}\mu_B B, \tag{2.82}$$

where σ has been replaced with "±" and $E_{mn}(\boldsymbol{k}_0)$ is the *subband edge* - i.e. Equation (2.34) at $k_\parallel = 0$. The magnetic dependence of n_B and $E^{\pm}_{mn\mathcal{N}}$, and therefore the evolution of μ_F, explains the quantised values of R_{xy} in Figure 2.19(a), or Figure

3.5(a) for a 2DHG in Ge-QW. Figure 2.20(a) shows calculated LLs for a 2DHG in a square QW by means of Equation (2.82). Blue and red lines correspond to spin-split LLs due to the Zeeman effect, which acts through the term $g^*_m \mu_B B/2$, while vertical dashed lines depict B-values for integer ν. The chemical potential (thick black line) is calculated by considering a constant carrier density which yields, at different magnetic fields, to the occupation of a certain number of LLs due to the change in n_B. This can be obtained through the condition:

$$N_s = \int_0^{\mu_{\mathrm{F}}(B)} g_B(E) dE, \tag{2.83}$$

where $g_B(E)$ is the LLs-DOS which depends on B.

Density of states and quantum lifetime. Without any scattering processes - from impurities, other electrons or phonons - $g_B(E)$ would be a set of δ-functions at energies $E = E^{\pm}_{mn\mathcal{N}}(B)$ [44]. In reality, by merely considering impurity scattering, which results in the so-called *quantum lifetime* τ_{q}, the LLs are instead broadened with linewidth $\Gamma = \hbar/\tau_{\mathrm{q}}$ [45]. Calculations of LLs-DOS, by taking into account scattering events with short range impurities (range $d < \lambda_c/(2\mathcal{N}+1)^{1/2}$), resulted in LLs with a semi-elliptic form and linewidth Γ [69]. Along these calculations for short range scattering, Γ was found to be independent on the particular LL-index $\mathcal{N}$ but is B-dependent as:

$$\Gamma = \sqrt{\frac{2\hbar^2 eB}{\pi m^*_b \tau_{\mathrm{tr}}}}, \tag{2.84}$$

where m^*_b is the effective mass at the band edge. The LL's broadening Γ, for 2DHGs in sGe-QWs, are determined by means of cyclotron resonance experiments within this thesis and Equation (2.84) will allow the evaluation of τ_{tr}. Evaluating this parameter is fundamental in order to estimate the carrier mobility and, therefore, to compare results of this thesis with those obtained by means of magneto-transport experiments.

Chemical potential. The chemical potential in Figure 2.20(a) was calculated by means of Equation (2.83) and assuming LLs with a Lorentzian shape. By multiplying these Lorentzians with the number of states per LL (n_B) the DOS is given by:

$$g_B(E) = n_B \sum_{\mathcal{N}} \frac{1}{\pi} \frac{\Gamma/2}{(E - E_{\mathcal{N}})^2 + (\Gamma/2)^2}. \tag{2.85}$$

The obtained LL ($\mathcal{N} = 3$) is shown in Figure 2.20(b), where the coloured vertical

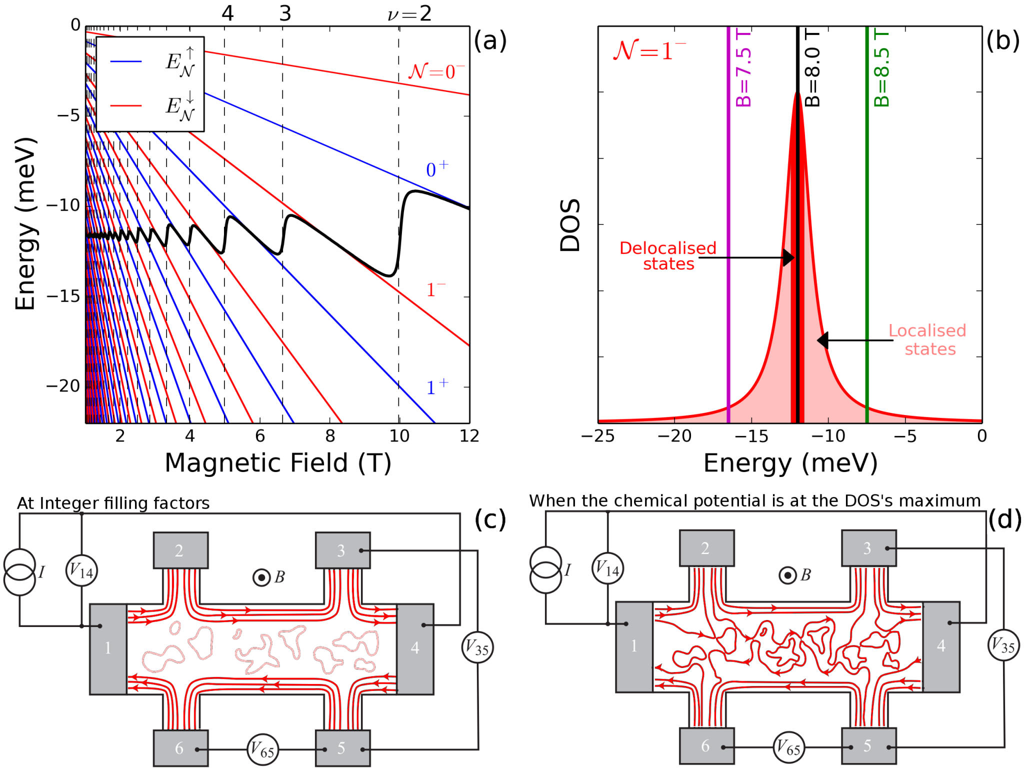

Figure 2.20: (**a**) LLs for spin up states (+, blue lines) and spin down states (−, red lines) calculated from Equation (2.82) [$N_s = 4.8 \times 10^{11}\,\mathrm{cm}^{-2}$, $m^* = 0.10\,m_0$]. Vertical dashed lines are values of the magnetic field for which the filling factor in Equation (2.78) is an integer. The thick black line is the chemical potential μ_F obtained, at different magnetic fields, from Equation (2.83) and (2.85). (**b**) DOS for the LL $N = 1^-$ obtained from Equation (2.85) which assumes a Lorentzian shape. Vertical coloured lines depict the different position of the μ_F with the magnetic field. Localised and delocalised states are indicated. (**c**) Hall bar at integer filling factors for which R_{xy} presents a plateau. (**d**) Hall bar showing that localised states contribute to R_{xx} when the chemical potential is at the DOS maximum in (**b**). (**c,d**) adapted from [45].

lines depict the evolution of the chemical potential at the indicated magnetic field. The bright and dark red regions within the LL depict *localised* and *delocalised* states [39]. These are used to explain the IQHE as in the following.

Localisation length and the Landauer-Büttiker picture. In Figure 2.20(a), the chemical potential at 10 T lies between two LLs with indexes $\mathcal{N} = 0^+$ and $\mathcal{N} = 1^-$. This is the B-region over which R_{xy} presents a plateau in Figure 2.19(a). By going down in magnetic field, for instance at $B = 8.5\,\mathrm{T}$ in Figure 2.20(a), the chemical potential starts to cross the LL $\mathcal{N} = 1^-$, as also shown in Figure 2.20(b). This, in Figure 2.19(a), corresponds to the decrease of R_{xy} and corresponding sharp increase of R_{xx}. Looking at Figure 2.20(b), at 8.0 T the chemical potential lies on the centre of the LL $\mathcal{N} = 3$ and, while R_{xy} in Figure 2.19(a) is varying, R_{xx} presents its local maximum, decreasing again at $B = 7.5\,\mathrm{T}$. The same concept can be extended by going down in magnetic field until LLs start to overlap and the system enters the classical regime.

As explained above, it is clear that plateaux in R_{xy}, and minima in R_{xx}, emerge when μ_{F} lies between LLs, while sharp features in R_{xx} appear when μ_{F} crosses a certain LL. The explanation relies, according to the Landauer-Büttiker picture, on understanding how localised and delocalised states contribute to the two resistances. Within the scaling theory, localised and delocalised states are distinguished in accordance with their different localisation length [70, 71]:

$$\mathcal{L} \propto |E - E_c|^{-s}, \tag{2.86}$$

where E_c is the energy at the centre of the LL and s is a critical exponent [72]. The Landauer-Büttiker picture can be explained by referring to Figure 2.20(c,d). Close to integer filling factor, as depicted in Figure 2.20(c), states far away from the edge of the Hall bar (bright red) are localised and do not contribute to R_{xx} and R_{xy}; there are not empty states for the localised states in order to contribute to the current [45]. Conversely, delocalised states at the edge of the Hall bar (darker red lines) contribute to the current. When, instead, μ_{F} starts to cross the LL, the localised states start to contribute to the current, changing both R_{xx} and R_{xy}. In particular, by referring to Figure 2.20(d), when μ_{F} is at the maximum of the LL in Figure 2.20(b), all the states at the Fermi level are delocalised, giving rise to the maximum in R_{xx} and to the change in R_{xy}.

2.5.2 Shubnikov-de Haas oscillations and SIA

The analysis of SdH oscillations is commonly used for QW characterisation but it can also provide information about the SIA and BIA spin-splitting [46]. Generally, the temperature and magnetic field dependence of the SdH oscillations amplitude is modelled in order to estimate fundamental parameters such as the effective mass, density and the *Dingle ratio* $\alpha_{\mathrm{D}} = \tau_{\mathrm{tr}}/\tau_{\mathrm{q}}$. According to its definition, the Dingle ratio gives information about the quantum lifetime τ_{q} and, as introduced in the previous section, the broadening of LLs [73].

In contrast with classic regime in the scheme of Figure 2.19(a), or for 2D-systems without SIA or BIA, Figure 2.21 shows an example of beating patterns

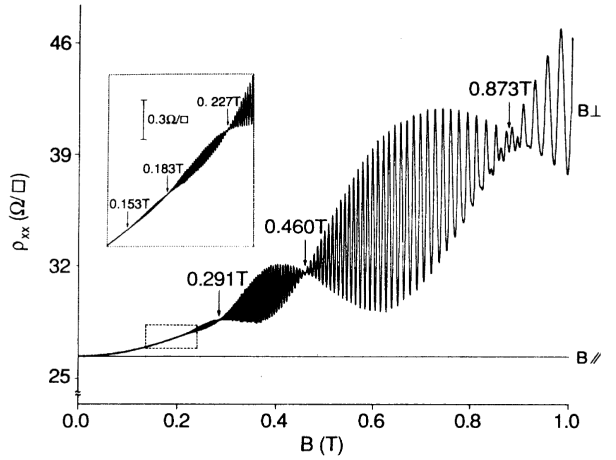

Figure 2.21: Beating effects in the SdH oscillations due to the contribution of spin-split subbands in a InGaAs/InAlAs-QW. Arrows indicate the magnetic field at which the SdH present beating nodes. By evaluating the two different frequencies causing the SdH-beating, the spin-split density of the 2D-systems can be evaluated and used to determine the SOI coefficients, as in the case of Equation 2.52 for HHs. Beatings can also be modelled in order to extrapolate the spin-splitting energy Δ_{SIA} (see text). Reproduced from [74].

in the SdH-oscillation reported, for a 2DEG in a InGaAs/InAlAs-QW, by Das *et al.* [74]. Normally, that is for a single occupied subband, SdH-oscillations, at low-B, arise from the fast evolution of E_{F} between close LLs, as shown in Figure 2.20(a). Conversely, beating patterns appear when two occupied subbands contribute to R_{xx}. These can be thought of as two different subbands due to the confinement effect. However, in their work Das *et al.* assigned the SdH-oscillations to a single SOI split-subband as the reported density was not enough to guarantee the occupation of the second subband of the characterised sample. Even if the BIA splitting would also contribute in non-centrosymmetric InGaAs-QWs, Das *et al.* concluded that the dependence on k^3, at the estimated density, makes it negligible in comparison to the linear dependence of the SIA splitting (see Section 2.3). By determining the two frequencies, $f_{\pm}^{\text{SdH}}$, of the magneto-oscillation of ρ_{xx} (which is the resistance divided by the area of the used device) the split-densities can be evaluated as $N_{\pm} = ef_{\pm}^{\text{SdH}}/(2\pi\hbar)$.

As in the case of QWs without any BIA or SIA spin-splitting contribution, the analysis consisted of fitting the B-dependence of the SdH-oscillation amplitude. Differently from the usual case without SOI, the SIA contribution was considered by adding the spin-splitting energy within the oscillation amplitude as: $A \sim \cos \pi\nu$, where $\nu = \delta/\hbar\omega_{\text{c}}$ is the filling factor and $\delta \simeq \delta_0 + \delta_1\hbar\omega_{\text{c}}$ is the total splitting given by the zero magnetic field splitting (δ_0) and the linear splitting $\delta_1\hbar\omega_{\text{c}}$ (Zeeman). Interestingly, evaluated split-densities from the SdH-oscillation frequencies can also be used to determine the Rashba coefficient α, as in the case of Equation (2.52) for β_{HH} [75, 76] (the dependence on the split density, in the case of the k-linear split for electrons and LHs is not reported in this thesis and can be found in [46]). Table 2.1

outlines the highest values of SIA coefficients and energy spin-splitting reported for different 2D-systems.

Material	Density (10^{11}cm^{-2})	Strain	β (10^{-28}eVm^3)	α (10^{-12}eVm)	Δ (meV)
GaSb/InAs [77]	10	-	-	9	3.5
InGaAs/InAlAs [74]	15-18	-	-	4	1.5-2.5
AlGaN/GaN [78]	80	-	-	8.1	11.6
Ge/Si$_{0.5}$Ge$_{0.5}$ [59]	9.0-15.0	0.8	0.07-0.10	-	0.3-0.4
Ge/Si$_{0.2}$Ge$_{0.8}$ [75]	5.9	2.1	1	-	1.4

Table 2.1: Reported SIA coefficient, density, and spin-splitting energy for 2D-systems within different QWs.

2.6 Cyclotron resonance

Besides MT experiments, insight into the subband structure of 2D-systems is also obtained by means of magneto-optical spectroscopy (MS). The advantages of MS point towards the direct determination of the effective mass and the chance to investigate samples in a contactless way. In 1955, Dresselhaus, Kip and Kittel performed the first CR-experiment to probe the anisotropic response of carriers in Si and Ge by means of circularly-polarised electromagnetic fields in the microwave range [47]. Besides the determination of the anisotropic character of the effective mass (Section 2.1.2), circularly-polarised ac-fields also allow us to distinguish the response of electrons and holes related to the opposite cyclotron motion. Due to Equation (2.61), requirements to observe CR-features in MS-experiments are: (i) the choice of an appropriate frequency range in relation to the expected effective mass and (ii) a high relaxation time, τ, such that $\omega_c\tau > 1$ [79]. In semiconductors, the typical frequency range is the far infrared (FIR).

2.6.1 Absorption and light-polarisation dependence

In the quantum description, when the energy of light matches the energy difference between occupied and unoccupied LLs ($\hbar\omega_c$), photons can be absorbed and excite carriers into empty LLs. The ac-field can be considered by defining the vector potential $\boldsymbol{A} = [E_0/(i\omega)]\boldsymbol{e}e^{i\omega t}$, where $\boldsymbol{e} = (e_x, e_y, e_z)$ is the polarisation vector. Its influence in the Hamiltonian of the system can be considered as a perturbation [46]:

$$H' = H(\hbar\boldsymbol{k} + e\boldsymbol{A}) - H(\hbar\boldsymbol{k}) \simeq e\boldsymbol{A} \cdot \partial H/\hbar\partial\boldsymbol{k} \equiv e\boldsymbol{A} \cdot \boldsymbol{v}, \tag{2.87}$$

where $\boldsymbol{v}$ is the velocity operator. By considering intraband transitions - that is within the same subband n of the bulk band m - between occupied (initial), $|i\rangle \equiv E^{\pm}_{mn\mathcal{N}}$, and unoccupied (final), $|f\rangle \equiv E^{\pm}_{mn\mathcal{N}+1}$, LLs, the perturbation given by Equation (2.87) leads to the transition rate (Fermi's golden rule):

$$W_{if} = \frac{\pi e^2 E_0^2}{2\hbar\omega^2} |\langle i|\boldsymbol{e}\cdot\boldsymbol{v}|f\rangle|^2 [\delta(E_{if} - \hbar\omega) + \delta(E_{if} + \hbar\omega)], \tag{2.88}$$

where $E_{if} = |E^{\pm}_{mn\mathcal{N}+1} - E^{\pm}_{mn\mathcal{N}}|$.

Equation (2.88) also establishes *selection rules.* These arise from the term $|\langle o|\boldsymbol{e}\cdot\boldsymbol{v}|u\rangle|^2$ and differ by considering the spin- and Landau-indices of initial and final states, as well as the light polarisation which enters in the product $\boldsymbol{e}\cdot\boldsymbol{v}$. Experimentally, the aforementioned term can be explored with a combination of light polarisation and different geometries [80]: i) the *Faraday geometry*, where $\boldsymbol{B} \perp$ 2D-system; ii) the *Voigt geometry*, where $\boldsymbol{B} \parallel$ 2D-system. The different kind of transitions, related to specific selection rules, geometries and light polarisations, are summarised in Table 2.2.

To describe standard cyclotron resonances, it is convenient to consider $e_{\pm} = (e_x \pm i e_y)/\sqrt{2}$ in order to include the creation and annihilation operator in Equation (2.79) and describe the system using the LL-formalism in Section 2.5.1. In this case, the absorption coefficient - derived from Equation (2.88) and divided by the energy density of the electromagnetic field - is [46]:

$$\alpha(\omega) = \frac{2\pi}{n}\frac{e^2}{4\pi\hbar c}\sum_{i,f}(f_i - f_f)E_{if}\delta(E_{if} - \hbar\omega) \times |\langle i|e_+ a - e_- a^{\dagger} + e_z\lambda_c k_z|f\rangle|^2, \tag{2.89}$$

where n is the refractive index and f_i, f_f are the occupation factors (Fermi-Dirac function) of the initial and final state, respectively, defined by the chemical potential. By considering the LL-broadening, the δ-function must be replaced with a Lorentzian distribution.

Cyclotron resonance in Ge-QWs. Equation (2.89) has been used by by Winkler

Type	Selection rules	Geometry	Polarisation
Cyclotron resonance	same spin, $\Delta\mathcal{N} = \pm 1$	Faraday	Circular: $\boldsymbol{e} \perp \boldsymbol{B}$
Spin resonance	spin flip, $\Delta\mathcal{N} = 0$	Faraday	Circular: $\boldsymbol{e} \perp \boldsymbol{B}$
Combined resonance	spin flip, $\Delta\mathcal{N} = \pm 1$	Voigt	Longitudinal: $\boldsymbol{e} \perp \boldsymbol{B}$

Table 2.2: Different types of cyclotron resonances with respective selection rules. These can be obtained with the appropriate geometry (see text) and light polarisation [80].

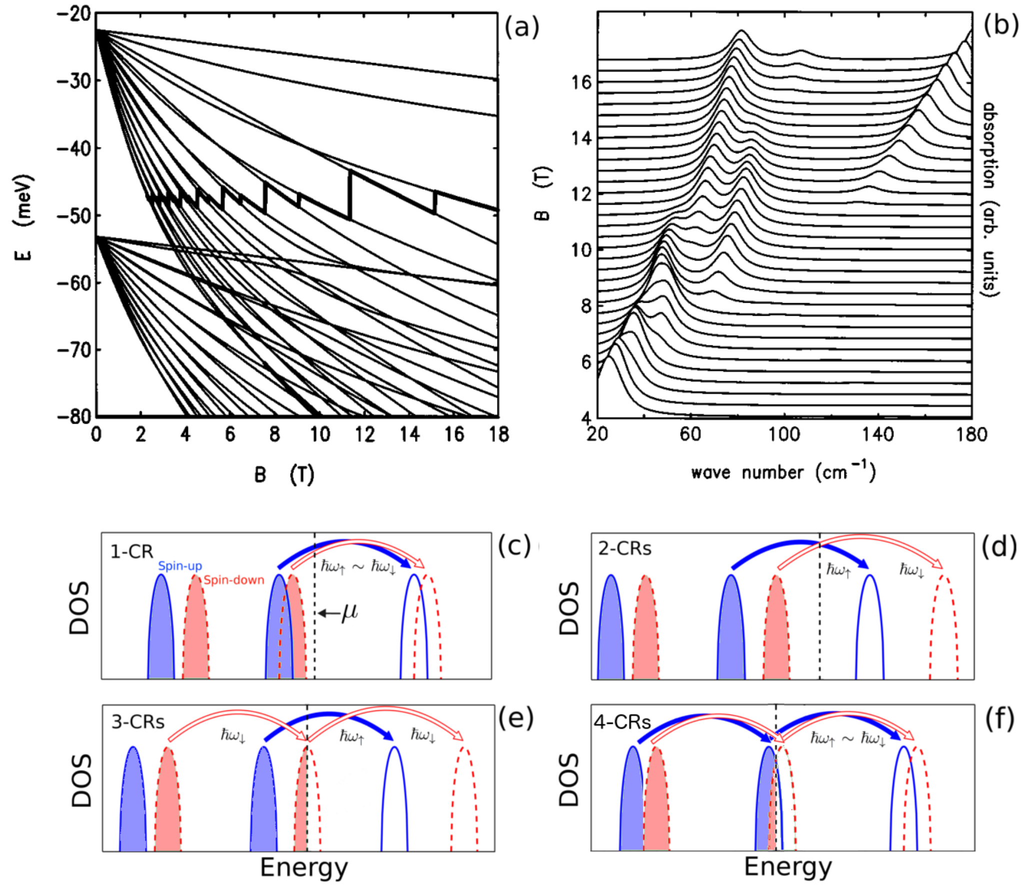

Figure 2.22: (**a**) Calculated LLs for the sGe-QW in Section 2.3.2; (**b**) CRs obtained from Equation (2.89). (adapted from [57]); (**c**) one CR as resulting for totally full, spin-splits and overlapping, LLs; (**d**) two CRs due to not overlapping LLs. (**e**) three CRs appearing for separated LLs with the chemical potential within the LL. (**f**): extreme case of four CRs.

et al. [57] in order to calculate the CR absorption of sGe-QWs presented in Section 2.3.2. Figure 2.22(a) shows the LLs for the first two subbands [see Figure 2.14(b) and 2.15(b)]. In comparison to LLs calculated in Figure 2.20(a), here LLs overlap and deviate from a linear evolution. This is due to the strong non-nonparabolicity of the respective valence subbands in Figure 2.15. As will be shown in Chapter 4, this can be approximated with an energy dependence for the effective mass and g-factor. The evolution of μ with B, and the overlap between adjacent LLs, result in the appearance of one, two or three CRs, as shown in Figure 2.22(b). The linewidth Γ of the different CRs at a certain magnetic field differs as this depends on the occupancy of the initial and final LLs. Overlapping LLs are depicted in Figure 2.22(c), resulting in transition energies $\hbar\omega_{c,\uparrow} \sim \hbar\omega_{c,\downarrow}$. As illustrated in Figure 2.22(d), for non-overlapping LLs two transitions are resolved, i.e. $\hbar\omega_{c,\uparrow} \neq \hbar\omega_{c,\downarrow}$, when the last two LLs are completely occupied. In Figure 2.22(e), three CRs appear for partial LL occupancy. Finally, Figure 2.22(f) depicts the extreme case of four CRs owing to overlapping LLs with chemical potential such that both of them are partially occupied. These are generally not resolved due to their similar frequency.

2.7 Summary

The influence of strain, 2D-confinement, and the SOI due to structural inversion asymmetry have been introduced with particular focus on HH-bands in sGe-QWs. The described magnetic field effects, as well as the nonparabolicity of the HH-bands in Ge, will be used in Chapter 4 and 5 in order to interpret and analyse data obtained by means of THz time-domain magneto-spectroscopy. In particular, the formalism developed in Section 2.5 and 2.6 will be fundamental in estimating important quantities such as effective mass, g-factor and Rashba spin-splitting within the characterised samples.

Chapter 3

Experimental methodology

3.1 Introduction

Most of the spectroscopic techniques record, as a function of the frequency or wavelength, the mean intensity of the electromagnetic radiation, $|\mathbf{E}(\omega)|^2$, losing the time information and therefore the *phase*. By measuring the radiation intensity, reflected and transmitted through a sample, the determination of the optical properties of materials relies on the use of the Kramers-Kronig relations to obtain the *complex refractive index* $\tilde{n}(\omega) = n(\omega) + i\kappa(\omega)$. In contrast, by time-resolving the electric field of an electromagnetic pulse, *time-domain spectroscopy* (TDS) allows the direct measurement of the real and imaginary part of $\tilde{n}(\omega)$. Terahertz (THz)-TDS, i.e. TDS which exploits pulses with sub-picosecond duration (1 ps $= 1 \times 10^{-12}\,$s) and frequencies between 300 GHz and 10 THz (10 to 300 cm^{-1}, 1000 to 30 μm or 1 to 41 meV), is a powerful tool to investigate material properties. This provides insights into the frequency- and time-dependent response of free carriers, fundamental excitations (such as rotations, vibrations), collective modes (phonons, plasma, magnons), energy gaps associated with superconductivity, as well as intra-excitonic transitions [81].

Since the characterisation of sGe-QWs within this thesis is performed by means of THz-TD magneto-spectroscopy (THz-TDMS), i.e. time-resoved cyclotron resonance experiments, the following chapter first introduces (Section 3.2) the general scheme of THz-TDS experiments. THz-pulses are generated from photoconductive emitters (Section 3.2.1) and detected by means of electro-optic sampling. This is described in Section 3.2.2 together with the calibration and detection methods which also considers the response of the adopted electro-optic crystal (ZnTe).

The experimental setup for polarisation resolved TH-TDMS experiments (PR-THz-TDMS) is introduced in Section 3.2.3. Advantages of performing THz-TDS are outlined in Section 3.3, with a particular focus on the chance to directly measure the complex refractive index (of bulk materials) and the complex conductivity for thin conductive materials (Section 3.3.1). The structure of the characterised samples, as well as their general applicability in CMOS technology and spintronics, are presented in Section 3.4. Results of standard magneto-transport (MT) experiments - outlined earlier in Section 2.5.1 - on two of the four sGe-QW samples investigated in the following thesis are finally given in Section 3.4.1.

3.2 Experimental setup

The key of time-domain techniques, as depicted in the top-left inset of Figure 3.1, is the time-delay between two pulses with different duration. The respective path, and therefore the respective arrival time, is varied in order that the shortest pulse - often referred to as the *probe pulse* or *gate beam* - probes the electric field of the longer pulse which is time resolved.

A general scheme of the THz-TDS setup, as used in this thesis, is depicted in Figure 3.1. Femtosecond, linearly-polarised, pulses were provided by a Spectra-Physics MaiTai Ti:Sapphire laser, with $\sim 80\,\mathrm{MHz}$ repetition rate, $\sim 70\,\mathrm{fs}$ duration and energy of $\sim 25\,\mathrm{nJ}$. In Ti-doped Sapphire crystals, due to the interaction of electrons with the Sapphire's phonon modes, the electronic ground states of Ti^{3+} ions are split in two broad vibronic bands defining the ground, and the excited states, of a laser system. The inversion population within the Ti:Sapphire crystal is obtained with a CW-laser ($\lambda = 532\,\mathrm{nm}$) which, together with using an acousto-optic modulator, allows the generation of stable, mode-locked, linearly-polarised fs-pulses [82]. Furthermore, the output wavelength in the MaiTai laser can be tuned (710-910 nm) by means of a sequence of prisms. These spatially separate the broadband pulse wavelengths, which are then chosen by moving a slit.

In the experiments presented in the next chapters, 800 nm fs-pulses are split in two different beams: the former (exciting pulse, purple line in Figure 3.1), is used to generate THz-pulses, while the latter (red line) is the gate beam. The adopted generation and detection methods are described as follows.

3.2.1 THz-Generation

THz pulse sources exploit different physical effects - such as photoconductive (PC) or optical rectification mechanisms [83]. In this work, THz generation relies on a interdigitated PC emitter fabricated on a GaAs substrate. This consists of an array of parallel PC-switches and its general scheme will be presented later in Chapter 6. An example of a PC-switch is depicted in the bottom part of Figure 3.1. The exciting beam (1.55 eV) generates electrons and holes at the surface of the GaAs substrate ($E_g = 1.42$ at RT). Their acceleration, by means of an applied potential between two metallic contacts, leads to an ultrafast change in the photocurrent $J_{ph}(t)$. This, as a consequence of Maxwell's equations, results in the emission of THz pulses with $E_{\text{THz}}(t) \propto dJ_{ph}(t)/dt$ [83]. Since carriers accelerate parallel to the applied potential, the emitted THz-pulse is linearly polarised, i.e. $E_{\text{THz},x} \gg E_{\text{THz},y}$. Emitted pulses are collimated and focused into an Oxford superconducting magnet (0-7.5 T, 2 K to 300 K) by means of a couple of off-axis parabolic mirrors. Samples are placed within the magnet by means of a vertically movable stage which allows us to measure the transmission through different samples mounted on circular slots with dimension bigger than the size of the THz-beam at the focus. In respect of the THz-polarisation and magnetic field orientation, samples are in the Faraday geometry (see Section 2.6.1). After the magnet, a further couple of off-axis parabolic mirrors collimate and focus again the THz pulse on to a ZnTe crystal, which allows us to time-resolve the THz-pulse by means of a delay stage and electro-optic sampling, as follows.

3.2.2 Electro-optic sampling

To measure the THz-pulse amplitude as a function of time, i.e. an electromagnetic *waveform*, experiments in this thesis relied on electro-optic sampling (EOS). The used EOS-scheme is depicted in Figure 3.1 and consists of an EO-crystal - (110)-ZnTe in this case - a quarter-wave-plate (QWP), a Wollaston prism (WL) and two photodiodes (PDs). Other detection methods can be found in Refs. [83, 81].

Calibration. In calibrating the EOS detection, the linear polarisation of the gate beam, after transmitting through the ZnTe and the QWP, is made circular by a proper rotation of the QWP. Wave-plates are birefringent materials characterised by an *extraordinary axis* (or *fast axis*) - with refractive index n_e - and an *ordinary axis* - with refractive index n_o. The difference between n_e and n_o results in different propagation speeds for the light components along the respective axes and,

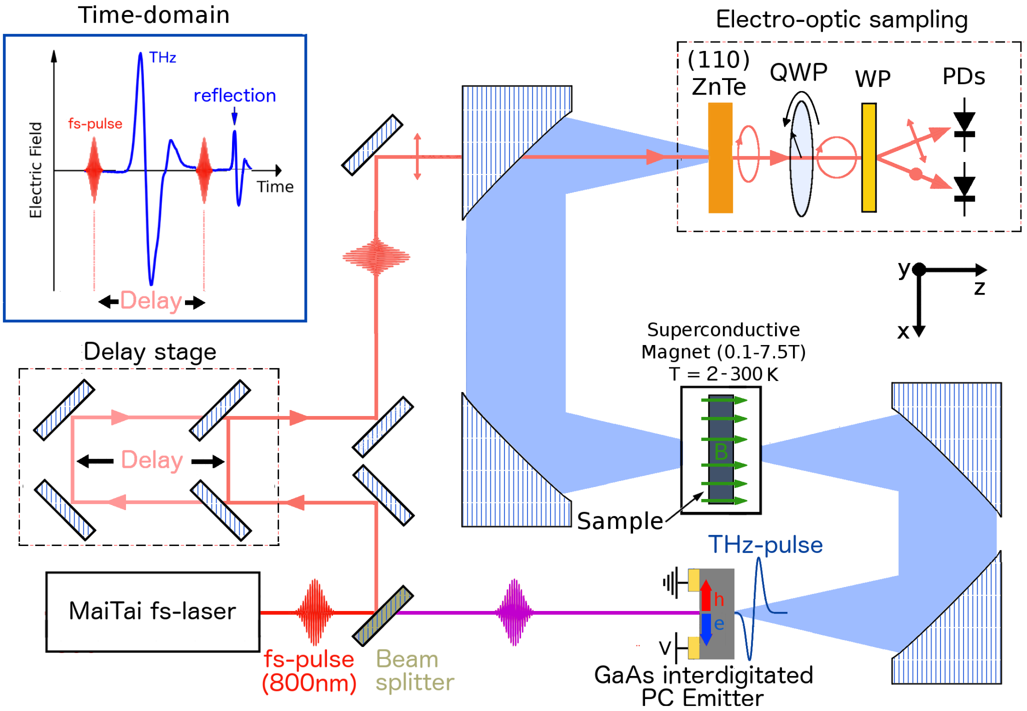

Figure 3.1: Experimental setup used for the characterisation of sGe-QWs in Chapter 4. Femtoseconds pulses are generated from a SpectraPhysics MaiTai Ti:Sapphire laser. A beam splitter is used in order to generate and detect THz-pulses (see text). The blue box (top-left) depicts an example of THz-waveform (blue line) together with the first reflection. The gate, or probe, beam is depicted as red line. The waveform is probed at different time by means of a delay stage. THz-pulses are generated by an interdigitated PC emitter and detected via the electro-optic sampling, which used a $< 110 >$-ZnTe (see text).

therefore, in a phase mismatch [83]:

$$\Delta\phi_{\mathrm{QWP}} = \frac{\omega}{c}(n_e - n_o)d, \tag{3.1}$$

where d is the wave-plate thickness. Half-wave plates (HWPs) are designed such that their thickness d_{HWP} results in $\Delta\phi_{\mathrm{HWP}} = \pi$, therefore in a 90° rotation of the light polarisation when the polarisation of the incident light makes an angle $\theta_{\mathrm{fast}} = \pi/4$ with the fast axis. Conversely, for $\theta_{\mathrm{fast}} = \pi/4$, a d_{QWP}-thick QWP leads to $\Delta\phi_{\mathrm{QWP}} = \pi/2$, making the polarisation of the incident light circular after transmitting through the QWP. Hence, this leads to the same intensity for the two orthogonal components along the x- and y-axis, i.e. $I_x = I_y = I_0/2$, where I_0 is the total intensity of the gate beam, and results in a voltage difference $\Delta V_{\mathrm{PDs}} = 0$ at the PDs.

THz-detection. In the presented setup, the detection of THz-radiation exploits the Pockels effect (or electro-optic effect), i.e. a second-order, electrically induced, susceptibility which results in the birefringent behaviour of EO-crystals [42]. The electric-field provided by the THz-pulse affects the susceptibility of the ZnTe crystal (with thickness d_{ZnTe}) and leads - similar to the case of wave-plates - to a phase mismatch [83]:

$$\Delta\phi^{\mathrm{THz}}(x_{\mathrm{ds}}) \propto \; d_{\mathrm{ZnTe}} E_{\mathrm{THz}}(x_{\mathrm{ds}}), \tag{3.2}$$

which depends on the path difference between THz- and gate-pulses (x_{ds}), controlled by the delay stage. If the gate-pulse travels within the ZnTe when $E_{\mathrm{THz}} \neq 0$, the gate-beam polarisation is slightly changed due to $\Delta\phi_{\mathrm{THz}}$. The two orthogonal components, split by the WP, result in a different intensity, $I_{xy} = I_0[1 \pm \Delta\phi_{\mathrm{THz}}(x_{\mathrm{ds}})]$, which is measured as the voltage difference between the two PDs, i.e.:

$$\Delta V_{\mathrm{PDs}}(x_{\mathrm{ds}}) \propto \Delta\phi_{\mathrm{THz}}(x_{\mathrm{ds}}) \propto E_{\mathrm{THz}}(x_{\mathrm{ds}}). \tag{3.3}$$

Since $\Delta\phi_{\mathrm{THz}}$ is small, EOS requires a lock-in amplifier to detect small changes in ΔV_{PD}. For this reason, the voltage applied on the PC-emitter is modulated with a frequency $\sim$ 10 kHz, which is used as a reference for the lock-in detection and ensures a high signal-to-noise ratio. The delay stage is moved in order to obtain the entire THz-waveform, as depicted in the blue box of Figure 3.1. By considering that moving the delay stage by x_{ds} leads to double the path change for the gate-beam, the conversion from delay-distance (in mm) to delay-time (in ps) is obtained with $t(\mathrm{ps}) = 2x_{\mathrm{ds}}/c \sim x_{\mathrm{ds}}/0.1499$.

ZnTe response. More precisely, the measured THz-signal for a gate beam angular frequency ω, $E^{\mathrm{S}}_{\mathrm{THz}}$, differs from the real E_{THz} and is given by the convolution with the ZnTe response function $F_{\mathrm{ZnTe}}(\omega, \omega_{\mathrm{THz}})$ as [83, 84]:

$$E^{\mathrm{S}}_{\mathrm{THz}}(t) = \int_{-\infty}^{+\infty} E_{\mathrm{THz}}(\omega_{\mathrm{THz}}) F_{\mathrm{ZnTe}}(\omega, \omega_{\mathrm{THz}}) e^{-i\omega_{\mathrm{THz}} t} d\omega_{\mathrm{THz}}, \tag{3.4}$$

whose Fourier transform leads to:

$$E^{\mathrm{S}}_{\mathrm{THz}}(\omega_{\mathrm{THz}}) = E_{\mathrm{THz}}(\omega_{\mathrm{THz}}) F_{\mathrm{ZnTe}}(\omega, \omega_{\mathrm{THz}}). \tag{3.5}$$

As the experimental setup just described used a 2mm-thick (110)-ZnTe, $E_{\mathrm{THz}}(\omega_{\mathrm{THz}})$ is obtained as follows. The ZnTe response is given by three different frequency factors: the autocorrelation of the optical electric field, the second order nonlinear susceptibility and the frequency-dependent velocity mismatch [83, 84]. Within this thesis, the response is considered as merely due to the latter factor which gives rise to a frequency filter function [84]:

$$F_{\mathrm{ZnTe}}(\omega, \omega_{\mathrm{THz}}) = \frac{e^{i\Delta k(\omega,\omega_{\mathrm{THz}})d_{\mathrm{ZnTe}}-1}}{i\Delta k(\omega, \omega_{\mathrm{THz}})}, \tag{3.6}$$

where

$$\Delta k(\omega, \omega_{\mathrm{THz}}) \simeq \frac{\tilde{n}^{\mathrm{THz}}_{\mathrm{ZnTe}}\omega_{\mathrm{THz}}}{c} - \frac{\omega_{\mathrm{THz}}}{v_g(\omega)} \tag{3.7}$$

and $v_g(\omega) = c/[n_{\mathrm{opt}}(\omega) - \partial n_{\mathrm{opt}}/\partial\omega]$ is the optical group-velocity. Here d_{ZnTe} is the ZnTe thicnkess, $n_{\mathrm{opt}}(\omega)$ is the optical refractive index given in Ref. [85] and $\tilde{n}^{\mathrm{THz}}_{\mathrm{ZnTe}}$ is the complex refractive index at THz-frequencies, which is given in Ref. [84] and takes into account the TO-phonon resonance in ZnTe ($\omega^{\mathrm{TO}}_{\mathrm{ZnTe}}/2\pi = 5.32\,\mathrm{THz}$). By considering $\omega = 2\pi c/\lambda_g$ - where $\lambda_g = 800\,\mathrm{nm}$ is the wavelength of the gate beam - the real THz spectrum $E_{\mathrm{THz}}(\omega)$ is obtained from Equation (3.5). The inverse Fourier transform then yields $E_{\mathrm{THz}}(t)$.

3.2.3 Polarisation resolved THz-TDMS

As will be outlined in Section 3.3.1, for conductive materials the THz-pulse transmission T is related to the conductivity σ. In more detail, by focusing onto samples THz-pulse linearly polarised along x, the transmission measured along the same direction is related to the conductivity tensor element σ_{xx}. Without applying a magnetic field $\sigma_{xy} = 0$ and therefore $E_{\mathrm{THz},y}$ will be not affected. Conversely, the application of a magnetic field on a conductive sample leads to the Faraday effect (Section 5.1). This rotates the polarisation of E_{THz} and results in a change of $E_{\mathrm{THz},y}$ which can be measured by using a polarisation-resolved THz-TDS setup.

In principle, one can think to rotate the (110)-ZnTe in order to maximise the signal of $E_{\mathrm{THz},x}$ and, afterwards, rotate the (110)-ZnTe by $\pi/2$ and probe the orthogonal component $E_{\mathrm{THz},y}$. Unfortunately, this simple idea is complicated by the fact that the detection efficiency of THz-pulses critically depends on the respective polarisation of the gate and THz radiation, as well as on their propagation direction and polarisation in respect of the (001)-axis of the (110)-ZnTe [86]. Furthermore, the detection efficiency changes by focusing both THz and gate beam on different parts of the ZnTe, therefore a very precise alignment is needed in order to rotate the ZnTe and focus both gate and THz beams on the same point. A full description of the detection efficiency in respect of different propagation directions - and

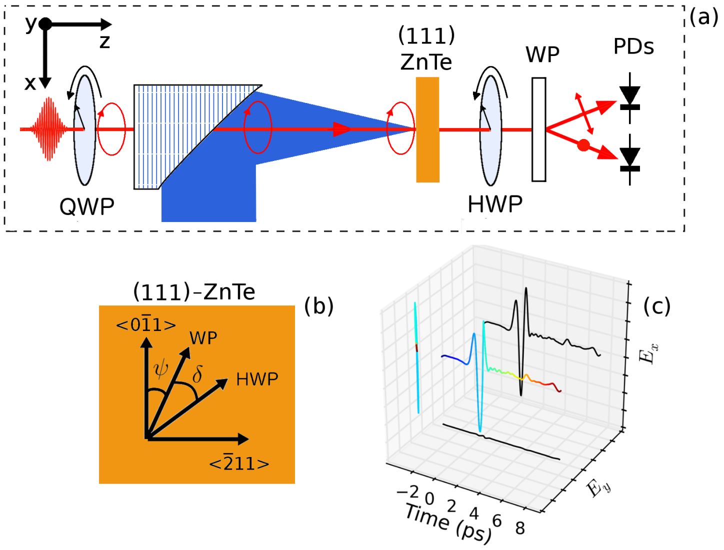

Figure 3.2: (**a**) Modified electro-optic sampling scheme (in comparison with the experimental setup of Figure 3.1) which was used for the characterisation of sGe-QWs in Chapter 5. This allowed to measure the orthogonal components of THz-pulses by using a $< 111 >$-ZnTe crystal depicted in (**b**). (**c**) Orthogonal components of the generated THz-pulse resulting in a linear polarised pulse $E_x \gg E_y$ (see text).

polarisations - of the gate beam within EO-crystals, and independent of the THz propagation direction, is reported in Ref. [87]. This description led van der Valk *et al.* to demonstrate an EOS-scheme which overcomes the issues mentioned above, therefore allowing the detection of the orthogonal components of a THz-pulse [88]. This EOS-scheme was used within this thesis for the experiments reported in Chapter 5 and is depicted in Figure 3.2(a). Differently from the experimental scheme in Figure 3.1, the (110)-ZnTe is replaced with a (111)-ZnTe. The QWP is moved before the EO-crystal and a HWP is positioned before the WP. The QWP, HWP and (111)-ZnTe were mounted on rotation stages, allowing precise and remotely controlled rotation. By using the experimental setup just described, the voltage difference between the two PDs is [88]:

$$\Delta V_{\mathrm{PDs}} \propto [E_{\mathrm{THz}}^{\bar{2}11}\sin(2\psi - 4\delta) + E_{\mathrm{THz}}^{0\bar{1}1}\cos(2\psi - 4\delta)], \tag{3.8}$$

where $E_{\mathrm{THz}}^{\bar{2}11}$ and $E_{\mathrm{THz}}^{0\bar{1}1}$ are the THz-pulse components along the $< \bar{2}11 >$ and the $< 0\bar{1}1 >$ directions of the (111)-ZnTe, ψ is the angle between the WP and the $< 0\bar{1}1 >$-axis and δ is the angle between the HWP and the WP. These angles are schematically depicted in Figure 3.2(b). From Equation (3.3) and Figure 3.2(b), it is clear that the orthogonal components of the THz-pulse can be measured simply with a $\pi/8$-rotation of δ, if $\psi = 0$. This last condition, in fact, leads to $E_{\mathrm{THz}}^{\bar{2}11} = E_{\mathrm{THz},x}$ and $E_{\mathrm{THz}}^{0\bar{1}1} = E_{\mathrm{THz},y}$.

Calibration. In detail, the calibration was performed as follows. Since the probe beam is horizontally polarised, i.e. along x in Figure 3.2(a), $\delta = 0$ was found by minimising its vertical component (i.e. parallel to the y-axis) with a rotation of the HWP, therefore defining an angle $\theta_{\mathrm{HWP}}^{\mathrm{V}}$. In this first step, the QWP was not inserted. In a second step, the QWP was placed before the (111)-ZnTe and the two PDs were balanced by rotating the QWP by an angle $\theta_{\mathrm{QWP}}^{\mathrm{V}}$. Since the PC-emitter was mounted in order to obtain horizontally polarised THz-pulses (along x), the EO-signal was maximised by rotating the (111)-ZnTe in order to get $< 0\bar{1}1 > \parallel x$, therefore finding $\psi = 0$. At this point, measuring the THz-pulse component along y is simply obtained by a $\pi/8$-rotation of the HWP, i.e. $\theta_{\mathrm{HWP}}^{\mathrm{H}} = \theta_{\mathrm{HWP}}^{\mathrm{V}} - \pi/8$. A further rotation of the QWP to balance the PDs results in an angle $\theta_{\mathrm{QWP}}^{\mathrm{H}}$. Hence, this calibration procedure allows us to measure the two orthogonal components of the THz-pulse by simply rotating HWP and QWP at the angles $\theta_{\mathrm{HWP}}^{\mathrm{V}}$ and $\theta_{\mathrm{QWP}}^{\mathrm{V}}$ to probe the vertical component, and $\theta_{\mathrm{HWP}}^{\mathrm{H}}$ and $\theta_{\mathrm{QWP}}^{\mathrm{H}}$ for the horizontal component.

Using the (111)-ZnTe leads to an 18% smaller signal but, conveniently, allows measurements of $E_{\mathrm{THz},x}$ and $E_{\mathrm{THz},y}$ with an equal sensitivity [88]. The two orthogonal THz-pulse components in the time-domain are shown in Figure 3.2(c). Clearly $E_{\mathrm{THz},x} \gg E_{\mathrm{THz},y}$ - with a peak-to-peak ratio value of 52 - indicates a linearly-polarised pulse.

3.3 Optical properties from THz-TDS

As stated in the introduction of this chapter, the advantage of THz-TDS consists of measuring the time evolution of THz-pulses. THz-waveforms in the time-domain can be converted into the frequency-domain by a Fourier transform, providing the real and imaginary part of the THz-radiation. Determining $\tilde{n}(\omega)$ is fundamental in order to describe the electromagnetic response of materials. For non-magnetic materials (magnetic permittivity $\mu = 1$), this is related to the complex dielectric function:

$$\epsilon(\omega) = \tilde{n}^2(\omega) = (n(\omega) + i\kappa(\omega))^2, \tag{3.9}$$

whose form depends on the type of response to the THz-radiation. For conducting materials, $\epsilon(\omega)$ is related to the optical conductivity $\sigma(\omega)$ [89]:

$$\sigma(\omega) = -i\omega\epsilon_0[\epsilon(\omega) - \epsilon_L] \tag{3.10}$$

where ϵ_L is the lattice dielectric function which can be a constant (such as the high-frequency or low-frequency dielectric constant, ϵ_∞ and ϵ_s, respectively) or a function of frequency.

3.3.1 Transmission and complex refractive index

The Fourier-transformed THz-radiation, transmitted - with a normal incidence - through a sample with thickness d and complex refractive index $\tilde{n}_j$, can be written as:

$$E_t(\omega) = t_{ij}t_{ji}E_r(\omega)\exp\left[i\frac{\omega d}{c}(\tilde{n}_j - \tilde{n}_i)\right]\mathrm{FP}_{iji}(\omega), \tag{3.11}$$

where E_r is a reference pulse (no sample), $\tilde{n}_i$ is the complex refractive index of the medium i before and after the sample (i.e. the free space if E_r is measured without sample), $t_{ij} = 2\tilde{n}_i/(\tilde{n}_i + \tilde{n}_j)$ are the Fresnel transmission while FP_{iji} is the Fabry-Perot term which considers multiple internal reflections. The Fabry-Perot term can be considered as FP=1 if the chosen time-window excludes the first internal reflection, whose example is depitcted in the blue box of Figure 3.1. Shorter time-windows with a duration $\Delta t = N_p\delta t$, on the other hand, preclude high frequency resolution (δf), which depends on the time-window as $\delta f = 1/\Delta t$. Here N_p is the number of data points in the time-domain and δt is the time resolution. Since the delay stage can move with a micrometer precision, the time resolution is of the order of fs. Internal reflections can arise from emitters, EO-crystals or the investigated samples. The arrival time of reflections from these different component depends on the refractive index and thickness as $t_r = 2nd/c$. Therefore, for similar refractive indices, thinner materials are likely to be responsible for the first reflection. Data points in the frequency domain can be interpolated in order to resolve features which are not distinguishable otherwise. This is obtained by adding zero points before and after the time-windowed, measured, signal. Since Δt is increased, this method - called *zero padding* - allows finer resolution δf by Fourier transforming the time domain data. To be noticed that the real experimental resolution is not increased.

In THz-TDS, the response of a system to an ac electromagnetic field - i.e. the determination of $\tilde{n}_j$ - is analysed by experimentally determining the transmission:

$$T(\omega) = \frac{E_t(\omega)}{E_r(\omega)}, \tag{3.12}$$

which, by considering Equation (3.11), leads to:

$$T(\omega) = |T|e^{i\phi(\omega)} = t_{ij}t_{ji} \exp\left[i\frac{\omega d}{c}(\tilde{n}_j - \tilde{n}_i)\right] \mathrm{FP}_{iji}(\omega). \tag{3.13}$$

Therefore, the direct determination of $\tilde{n}_j$ is just complicated by the presence of the complex t_{ij} terms and the knowledge of $\tilde{n}_i$. The influence of the t_{ij} terms is usually neglected within the thick- and thin-film approximations [89]. In the former case, and for material without strong absorption in the THz-range ($\alpha = 2\omega\kappa_j c$, with $\kappa_j \ll n_j$), the Fresnel terms are real and - by using the incident THz-pulse as reference ($E_r = E_{\text{inc}}$, such that $\tilde{n}_i = 1$) - Equation (3.13) allows the direct determination of:

$$n_j(\omega) = 1 + \frac{c\omega}{d}\phi(\omega) \quad \text{and} \quad \alpha = -\frac{2}{d}\ln\frac{|T(\omega)|}{|t_{ij}t_{ji}|}. \tag{3.14}$$

In the thin-film limit - as for a QW sandwiched between a material with complex refractive index $\tilde{n}_j$ - by considering a negligible optical thickness ($n_j\omega d/c \ll 1, k_j\omega d/c \ll 1$) and an infinite number of reflections for the FP-term in Equation (3.11), Equation (3.13) leads to:

$$T(\omega) = \frac{2n_i}{2n_i - i(\tilde{n}_j^2 + \tilde{n}_i^2)\omega d/c}. \tag{3.15}$$

which provides a direct measurement of the complex $\tilde{n}_j(\omega)$ of the QW. For a high conductive QW, one can approximate $\tilde{n}_j(\omega) \simeq i\sigma(\omega)/\omega\epsilon_0$ and, by considering Equations (3.9) and (3.10), the direct determination of the QW's conductivity can be obtained from the experimental transmission via [89]:

$$\sigma(\omega) = \frac{2\tilde{n}_i}{Z_0 d}\left(\frac{1}{T(\omega)} - 1\right), \tag{3.16}$$

where $Z_0 = 1/c\epsilon_0$ is the impedance of free space.

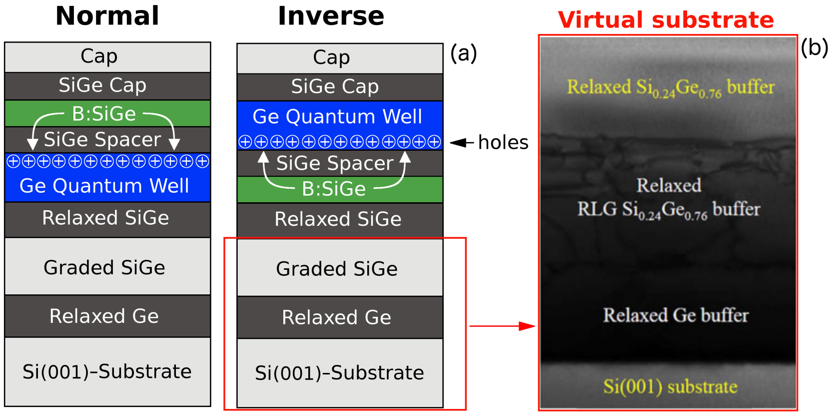

Figure 3.3: (**a**) Sample structure showing the normal and inverse modulation doping structure which refers to the position of the B:SiGe supply layer, above and below the sGe-QW, respectively. The red square enclosed the SiGe virtual substrates. (**b**) XTEM of a SiGe virtual substrate (adapted from [92]).

3.4 Ge-QW Samples

In Section 1.1.1 it was stated that the highest 2DHG mobility, to date, has been reported for sGe-QWs. Since the THz-TDS characterisation of such systems is the main goal of this thesis, the following outlines the general structure of the characterised samples.

Strained Ge-QWs were grown by Maksym Myronov and colleagues on lightly-doped Si (001) substrates using an ASM Epsilon 2000 reduced pressure chemical vapour deposition (RP-CVD) reactor [90]. In comparison with other deposition techniques such as molecular beam epitaxy (MBE) [91], RP-CVD assures very abrupt Ge/SiGe heterointerfaces and presents advantages such as faster deposition and smaller RMS surface roughness. The whole sample's structure is depicted in Figure 3.3(a). The virtual substrate is deposited on Si(001) and consists of a relaxed Ge buffer followed by a reverse linearly graded (RLG) $Si_{1-x}Ge_x$ with x going from 1 to a specific concentration $x < 1$. A relaxed SiGe buffer layer - with the same concentration of the final portion of the RLG buffer - is grown on top, ending the virtual substrate. This is enclosed by a red square in Figure 3.3(a). As an example, a XTEM scan of such kind of virtual substrates is shown in Figure 3.3(b) [92]. Clearly visible dislocations at the top of the RLG buffer are formed as a consequence of the relaxation due to a thickness bigger than the critical value t_c (Section 1.2.1).

Samples differ in regard of the modulation doping structure (Section 2.2). Generally, the MOSFET's channel is doped with impurities to provide carriers. However, as impurities act as sources of scattering, they affect the mobility. Instead,

Sample	Ge-QW Thickness (nm)	Modulation Doping	Si content (%)	Ge content (%)	Strain (%)
SiGe1	11	Inverse	20	80	0.8
SiGe2	22	Normal	20	80	0.8
Ge-10nm	10	Normal	30	70	1.3
Ge-20nm	20	Normal	30	70	1.3

Table 3.1: Structure parameters of the characterised samples.

the modulation doping consists of introducing impurities away from the channel (the QW in this case) to reduce impurity scattering. As depicted in Figure 3.3(a), the creation of the 2DHG within fully strained Ge-QWs is assured by a boron-doped (B:SiGe) supply layer with 20 nm separation from the QW. Its position, in respect of the Ge-QW, defines the inverse or normal modulation doping as depicted in Figure 3.3(a). The asymmetric doping assures an electric field which should provide the SIA (see Section 2.3) within the QW and, therefore, spin split states suitable for spin-FET devices (Section 2.4). In addition, as it is commonly believed that the BIA is absent in structures grown from centrosymmetric material, the SOI is merely due to the SIA in Ge-QWs [93, 94]. Finally, samples were capped with Si to prevent the oxidation of the SiGe layer which can cause the formation of interface traps. This also serves as a support for different processes [95], such as the creation of a Hall bar for magnetotransport (MT) characterisation (Section 2.5.1).

Table 3.1 summarises the general differences of samples which enclose Ge-QWs with different strain, thickness and modulation doping configuration (inverse or normal, see Figure 3.3). Holes within QWs are provided by B:SiGe supply layers doped with a boron concentration of $2 \times 10^{18}\,\mathrm{cm}^{-3}$ which ensures that only the HH sub-band is occupied and, moreover, the electric field necessary for the SIA.

3.4.1 Magnetotransport characterisation

As introduced in Section 2.3.1, differently from the electrons and light holes (LHs), the SIA for HHs results in a spin splitting energy which is cubic in the in-plane wavevector (Section 2.2.1) and related to the cubic Rashba coefficient β. The Ge content within the SiGe buffer layer is varied to provide different in-plane compressive strain according to Equation (1.1). In Figure 3.4(a), the nominal strain of samples is reported (red and blue dots), as a function of $a_{\mathrm{SiGe}}/a_{\mathrm{Ge}}$, together with the strain (2.1%) of a Ge-QW investigated by Moriya *et al.* (black dot) which reported $\beta = 0.1 - 0.07 \times 10^{-28}\,\mathrm{eVm}^3$ [59]. Since the strain is responsible for splitting the LH- and HH-bands with an energy difference $E_{\mathrm{HH}} - E_{\mathrm{LH}}$ (Section 2.1.3), this would affect the mobility of the 2DHG. The energy of LH and HH-bands (green curves) are shown in Figure 3.4(b) as a function of $a_{\mathrm{SiGe}}/a_{\mathrm{Ge}}$ [50]. The difference between these evolves from zero, at $a_{\mathrm{SiGe}}/a_{\mathrm{Ge}} = 1$ to a slightly constant value for $a_{\mathrm{SiGe}}/a_{\mathrm{Ge}} < 0.975$. As the SIA splits the spin-states proportionally to $\beta \propto 1/(E_{\mathrm{HH}} - E_{\mathrm{LH}})^2$ (details in Section 2.3.2), at high Ge contents (and then lower strain), the smaller energy difference between LH- and HH-bands would result in a bigger β than reported by Moriya *et al* [59].

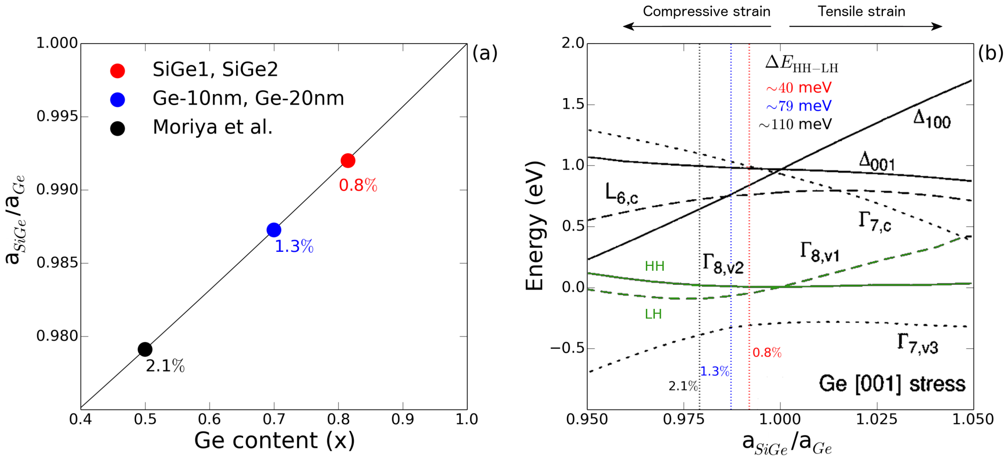

Figure 3.4: (**a**) Lattice mismatch at different Ge content (black line) [96]. Dots represent the lattice mismatch with respective strain [evaluated from Equation (2.30)] for sGe-QWs characterised by Moriya *et al.*[59] (black), and in this work (blue and red). (**b**) Calculated valence and conduction band shifts as a function of the lattice mismatch (adapted from [50]). Green lines are energies for the LH- and HH-bands. Vertical dashed lines depict the lattice mismatch of samples reported in (**a**). The relative split between the HH and LH band, $\Delta E_{\text{HH-LH}}$, is reported with respective colours.

For samples labelled SiGe1 and SiGe2, high resolution x-ray diffraction and XTEM experiments - performed by Chris Morrison and colleagues - confirmed the nominal strain and thickness of the QWs, respectively, as reported in Table 3.1. For samples Ge-10nm and -20nm, strain and thickness values are nominal.

Figure 3.5(a) shows the normalised sheet (or magneto) resistance, (MR, red line) and the Hall resistance (blue line), for the SiGe1 sample at 0.4 K performed by Chris Morrison and colleagues [75]. Clear plateaux in the Hall resistance appear because of the occupation of different Landau levels (LLs) by varying the magnetic field (Section 2.5.1). As shown in Figure 3.5(b), by plotting the MR (showing the Shubnikov-de Haas, SdH, oscillation) up to 2 T, beating patterns are resolved with nodes at approximately 0.65 T and 1.00 T. The inset shows the fast Fourier transform (FFT) of the MR with peaks observed at 11.4 and 13 T. The evaluation

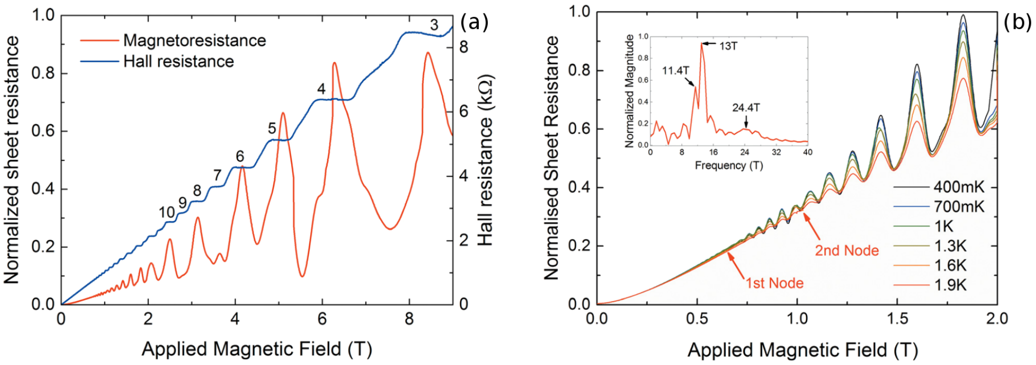

Figure 3.5: (**a**) Magnetotransport measurements of SiGe1 at 0.4K showing the normalised sheet resistance (SdH oscillations, red line) and the Hall resistance (plateaux, blue line) [75]. (**b**) SdH beatings due to the presence of distinct sheet densities for spin-up and spin-down states of HHs within the Ge-QW. The arrows indicate the beating nodes. The inset shows the FFT of the MR from where it is possible to evaluate the spin-split densities (see text). Reproduced from [75].

of these peaks, by following the analysis which was briefly outlined in Section 2.5.2, yields the spin-split sheet densities for HHs within the QW, which were found to be $p_{\uparrow}^{\mathrm{MT}} = 5.53 \times 10^{11}\ \mathrm{cm}^{-2}$ and $p_{\downarrow}^{\mathrm{MT}} = 6.31 \times 10^{11}\ \mathrm{cm}^{-2}$ [75], respectively. Here symbols $\uparrow, \downarrow$ refer to spin-up and spin-down states. From these values, by using Equation (2.52), the cubic Rashba coefficient was found to be $\beta_{\mathrm{MT}} = 1.0 \pm 0.6 \times 10^{-28}$ eVm^3 with a corresponding spin splitting energy $\Delta_{\mathrm{MT}} = 1.4 \pm 0.9\,\mathrm{meV}$ at the Fermi wavevector k_{F}.

For SiGe2, since MT measurements did not show any beating in the SdH oscillations, the evaluation of the Rashba SOI was not possible [97]. A calculation of the SdH beating (using the measured material parameters) resulted in an oscillation of the order of 5% which was not distinguishable because of the instrumental resolution. Nevertheless, signatures of the Rashba-SOI for SiGe2 have been obtained from the temperature dependence of the MR. From 0.4 K to 3 K, the MR was found to be first negative (associated with the Weak Localisation of carriers, WL) to positive (which is instead associated with the Weak Anti-Localisation, WAL, due to the Rashba-SOI). As this transition is opposite to what is expected, i.e. from WAL to WL, it could be associated with the presence of the Rashba SOI but with an opposite WL/WAL behaviour because of the presence of a further conducting layer. This might arise from the normal modulation doping structure of SiGe2 (see Figure 3.3) where, differently from SiGe1, the B:SiGe supply layer is in between the Hall bar - which was realised to perform MT measurements - and the Ge-QW.

No MT experiments have been performed on the Ge-10nm and -20nm sample.

3.5 Summary

The experimental methodology adopted in the following thesis, as well as the analysed sGe-QW samples, have been presented in this chapter. The following chapters will present the experimental data, and relative analysis, as obtained: from THz-TDMS experiments (outlined in Section 3.2) of 0.8% sGe-QWs (Chapter 4) and from PR-THz-TDMS (Section 3.2.3) of 1.3 % sGe-QWs (Chapter 5).

Chapter 4

Transport characterisation and Rashba effect in lower strain Ge-QWs

In this chapter, 0.8% strained germanium quantum wells (sGe-QWs) (sample SiGe1 and SiGe2 in Table 3.1) are characterised by means of THz time-domain magnetotransport spectroscopy (THz-TDMS) which allowed us to track spin-split cyclotron resonances (CRs) on picosecond time scales. The obtained results, in agreement with magnetotransport measurements, emphasise the suitability of the presented experiment and models for the characterisation of sGe-QWs, and more generally for the determination of the Rashba splitting energy Δ.

In Section 4.1, data are presented at different temperatures in order to distinguish between the substrate's and sGe-QW's response. Initially, the transmitted THz pulse through one of the samples, in the time- and frequency-domain at 100 K, is shown and discussed in Section 4.1.1. At high temperatures, where only the substrate contribution is resolved, the simulated transmission in the frequency-domain demonstrates the accuracy of determining effective masses within the substrates (Section 4.1.2). At T=2 K the substrate contribution disappears and the response of the heavy holes confined within the sGe-QWs results in split-CRs (Section 4.1.3). The CRs are analysed in Section 4.2 where the Gabor-Morlet transform of the time-domain waveforms is first presented as a useful method to discern the contribution of CRs with small spacing in frequency compared to the linewidth (Section 4.2.1). Adopted models to fit the time- and frequency-domain data and to estimate densities, effective masses and lifetimes at different magnetic fields, are outlined in

Section 4.2.2. In Section 4.3, the low magnetic field range is examined. In this range, the hole densities and effective masses are obtained (Section 4.3.1) together with a first evaluation of Δ (Section 4.3.2). By calculating the transitions between Landau levels in Section 4.4, the determined CR's frequencies from the time- and frequency-domain fits are well reproduced. This allowed a further determination of Δ, as well as the g-factors, for heavy holes (HHs) within the sGe-QWs. In Section 4.5, the magnetic field evolution of the evaluated THz-lifetimes permitted the estimation of the hole transport lifetimes. Finally, the spin-relaxation mechanism is compared with previous reports in Section 4.6.

The majority of this chapter was published as M. Failla *et al.*, Phys. Rev. B **92**, 045303 (2015).

4.1 Cyclotron response at different temperatures

In the following experiment, linearly polarised THz radiation pulses were focused on samples placed in a superconducting magnet in the Faraday geometry. Further details on the THz-generation and detection methods were given in Section 3.2.

4.1.1 Transmitted THz-pulses in time- and frequency-domain

An example of the transmitted THz-pulse in the time-domain, through the SiGe2 sample at 100 K, is shown without (black line) and with the application of the magnetic field $B = 4\,\mathrm{T}$ (blue line) in Figure 4.1(a). The experimental time-domain window is limited to 13 ps due to internal reflections of the THz pulse in the silicon substrate ($\sim 520\ \mu$m thick), see Section 3.3.1. The effect of the applied B is clearly noticeable: the amplitude of the transmitted pulse at $B = 4\,\mathrm{T}$ is decreased at earlier times while it is increased between 2.5 and 6 ps. As will be explained in Section 4.1.3, this indicates absorption phenomena due to the cyclotron motion of carriers, i.e. CRs which create an induced THz field at later times [98].

Absorption features within samples can be distinguished by converting data into the frequency-domain by means of the discrete Fourier transform, as shown in Figure 4.1 (b). The $B = 0\,\mathrm{T}$ transmitted pulse, black line, is characterised by a frequency range 0-3 THz with maximum amplitude at 0.61 THz. As a consequence of the 13 ps time-domain window, the frequency resolution is $\Delta f = 0.075\,\mathrm{THz}$ (Section 3.3.1). At $B = 4\,\mathrm{T}$, the decreased amplitude of the transmitted THz-pulse indicates that carriers within the sample experience a cyclotron motion with frequencies between 0.25-1 THz.

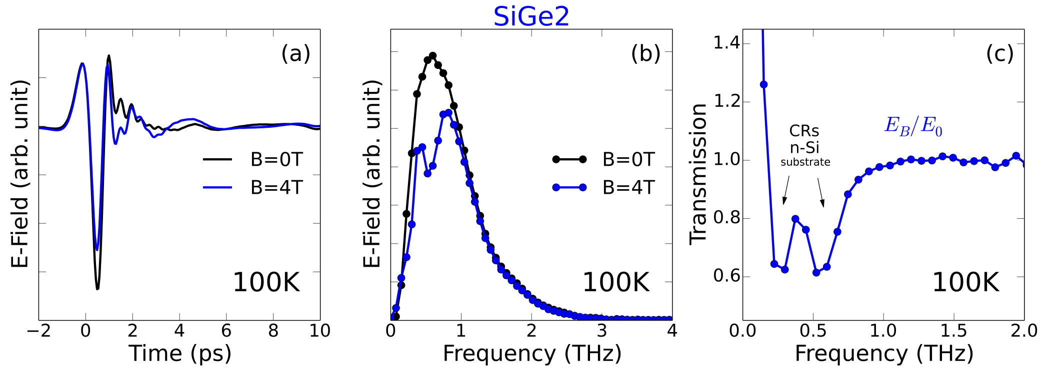

Figure 4.1: Comparison between the THz electric pulses transmitted through the sample SiGe2 at 100 K, with (blue line) and without (black) the application of $B = 4\,\mathrm{T}$, in the time- (**a**) and frequency-domain (**b**). (**c**) The transmission in frequency-domain, defined in Equation (4.1), shows CRs features which are ascribed to the n-Si substrate.

Since the cyclotron frequency is given by $\omega_c = eB/m^*$, the effective mass of carriers, m^*, can be evaluated from the frequency at which the CRs features present a minimum in the transmission spectrum. This is defined by the ratio:

$$T_B(\omega) = \frac{|E_B(\omega)|}{|E_0(\omega)|}, \tag{4.1}$$

and shown in Figure 4.1 (c). By taking into account that free carriers are only within the substrate and the sGe-QW, and since the substrate's carrier volume density is larger than within the QW (substrate thickness of $\sim 520\,\mu$m), the two absorption features are attributed to CRs of carriers in the lightly-doped n-Si substrate.

In order to distinguish the response of the QW and the substrate, the transmission in the temperature range 2-300 K is reported in Figure 4.2(a,b) for both samples. Curves are offset vertically for clarity. Since the magnetic field is kept constant, the CR frequencies ω_c are not altered. Hence, the differences between spectra in the 40-300 K range arise from the decrease - with increasing temperature - of the scattering lifetime, τ_{THz}, which defines the transition linewidth $\Gamma = \hbar/\tau_{\mathrm{THz}}$. This increases with temperature, as a result of the enhanced electron-phonon scattering. With the application of a magnetic field, electrons in Si move along constant energy surfaces (ellipsoids oriented along the [100], [010] and [001]) in the plane perpendicular to B. By considering the angle, θ, between B and the longitudinal axis of these ellipsoids, the effective mass is given by [47]:

$$\frac{1}{m^*} = \frac{\cos^2(\theta)}{m_t^2} + \frac{\sin^2(\theta)}{m_t m_l}, \tag{4.2}$$

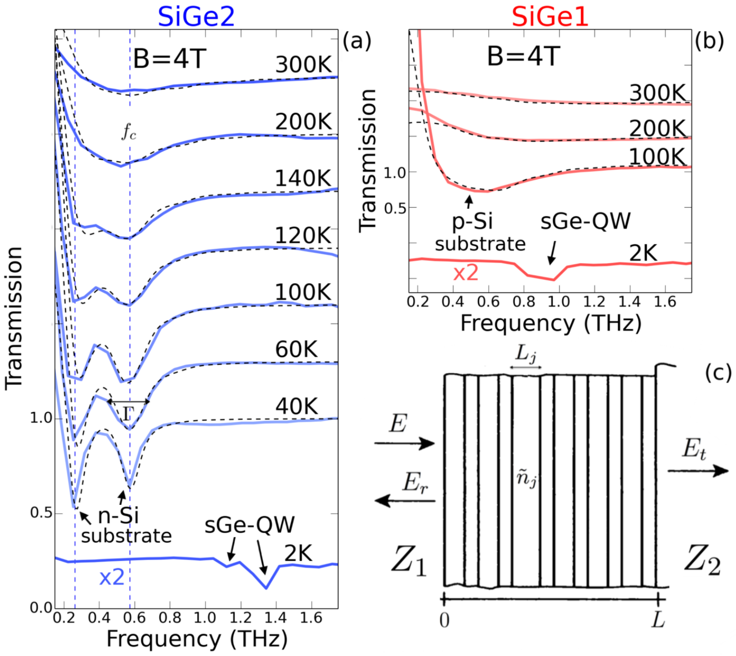

Figure 4.2: Evolution of the transmission spectra with temperature for both samples. Curves are offset vertically for clarity. The high temperature range shows the evolution of CRs arising from the n-Si (**a**) and p-Si (**b**) substrates. Vertical dashed lines depict the CR-frequencies f_c. The CR linewidth, $\Gamma = \hbar/\tau_{\mathrm{THz}}$ increases with temperature. Features of the bottom spectra at 2 K are ascribed to holes within the sGe-QWs. Dashed line are modeled transmissions obtained by considering a stack of dielectrics as depicted in (**c**) (adapted from [99]).

where $m_l = 0.19\, m_e$ and $m_t = 0.98\, m_e$ are the longitudinal and transverse effective mass in Si, respectively. In the case of $B \parallel [001]$ (which is the growth direction of both SiGe1 and SiGe2), $\theta = 0, \pi/2$ and Equation (4.2) leads to two different CRs with effective masses $m_1 \simeq 0.19\, m_e$ and $m_2 \simeq 0.43\, m_e$, as a consequence of the anisotropic character of the conduction band in Si. For the case of the p-Si substrate in SiGe1, CRs arise from holes moving along the warped energy surfaces defined in Equation (2.28) with effective masses $m_1 \simeq 0.16\, m_e$ and $m_2 \simeq 0.49\, m_e$ [47], which are the effective masses for LHs and HHs in Si, respectively [see Table 1.1 and Equation (2.29)]. By comparing the transmission at 100 K for SiGe1 [Figure 4.2(b)] and SiGe2 [Figure 4.2(a)], in the former case two CRs are not resolved due to the lower hole mobility in Si which leads to broader linewidth and undistinguishable CR-features.

At low temperatures, carriers within substrates are frozen-out and CR-features at 2 K, shown in the bottom spectra in Figure 4.2(a,b), are ascribed to holes within the sGe-QWs. The distinction between substrate- and QW-CRs is further confirmed by the fact that a reference sample with just SiGe layers showed no CRs at 2 K.

4.1.2 Simulated transmission: the stack model

The accurate determination of the density, effective mass and scattering lifetime can be achieved by modelling the transmission in the frequency-domain. The black dashed lines in Figure 4.2 (a,b) indicate transmission simulations obtained from a stack model as depicted in Figure 4.2 (c) [99]. By considering $Z_1 = Z_2 = Z_0 \sim 377\Omega$, the transmitted ($E_t$) and reflected ($E_r$) electromagnetic field amplitude, which passes perpendicularly through a stack of dielectrics with complex refractive index $\tilde{n}_j$ and thickness L_j, is described in the frequency-domain by:

$$\begin{pmatrix} 1+E_r \\ 1-E_r \end{pmatrix} = \prod_j \begin{pmatrix} \cos(\tilde{n}_j L_j \omega/c) & -i/\tilde{n}_j \sin(\tilde{n}_j L_j \omega/c) \\ -(i\tilde{n}_j)\sin(\tilde{n}_j L_j \omega/c) & \cos(\tilde{n}_j L_j \omega/c) \end{pmatrix} \begin{pmatrix} E_t \\ E_t \end{pmatrix}. \tag{4.3}$$

Here $\omega = 2\pi f$ is the angular frequency and c is the speed of light in vacuum. Solving Equation (4.3) the transmitted pulse through the whole sample, at a certain B, is:

$$E_{t,B}(\omega) = \frac{2}{A_{11} + A_{12} + A_{21} + A_{22}}, \tag{4.4}$$

where $A_{i,j}$ are the matrix elements given by the product of matrices in Equation (4.3). The simulated transmission is then obtained considering $T_B(\omega) = E_{t,B}(\omega)/E_{t,0}(\omega)$.

While for layers without free carriers the refractive index is a constant, in the presence of free carriers the conductivity tensor σ_j, in the Drude model, results in a frequency-dependent refractive index (see Section 3.3):

$$\tilde{n}_j(\omega) = \sqrt{\epsilon_L(\omega) + i\frac{\sigma_j(\omega)}{\epsilon_0 \omega}}, \tag{4.5}$$

where $\epsilon_L(\omega)$ is the lattice dielectric constant, $\sigma_j(\omega)$ is the frequency-dependent conductivity and ϵ_0 is the vacuum permittivity. Because in the following experiment the transmitted THz pulse has the same polarisation as the incident pulse, i.e. $T_B(\omega) = T_{xx,B}(\omega)$, the conductivity is related to the diagonal elements of the conductivity tensor, $\sigma_{xx} = \sigma_{yy}$, as defined in Equation (2.65). In the most generic case, in which the j-th layer contributes with more than one CR, as clearly evident for the n-Si substrate of sample SiGe2, the conductivity can be written as [100]:

$$\sigma_j(\omega) = \sum_i \sigma_{xx,i}(\omega) = \sum_i \frac{N_i e^2}{m_i^*} \frac{i\omega - 1/\tau_i}{(\omega + i/\tau_\mathrm{i})^2 - \omega_{c,i}^2}, \tag{4.6}$$

Sample	Substrate	m_1^* (m_e)	m_2^* (m_e)
SiGe1	p-Si (001)	0.16 ± 0.02	0.49 ± 0.01
SiGe2	n-Si (001)	0.19 ± 0.02	0.43 ± 0.01

Table 4.1: Effective masses of holes and electrons within the p-Si and n-Si substrates, respectively, obtained from the modeled transmission at $T \geq 40\,\mathrm{K}$.

and the i-th CR contribution is modelled by varying the cyclotron frequency $\omega_{c,i} = eB/m_i^*$, carrier density N_i (per volume), effective mass m_i^*, and scattering lifetime τ_i.

The good agreement of fits in Figure 4.2 with data is obtained with values (see Table 4.1) of effective masses for electrons and holes in Si [47], as reported in the previous section. The increase in carrier density with temperature allowed an activation energy of 9 ± 2 meV to be obtained for the n-Si substrate of sample SiGe2.

4.1.3 Transmission at T=2K

In the previous section it has been demonstrated that, at 2 K, the response of the sGe-QWs can be isolated from the substrate response because of the freezing out of carriers. Examples of transmitted THz-pulses through the SiGe1 sample, at 2 K, with and without a magnetic field of 3 T, are shown in the time-domain in Figure 4.3(a). Dashed lines represent raw data while the green and yellow ones are deconvoluted with the ZnTe crystal frequency-dependent response (Section 3.2.2).

The measured electric field transmitted through the samples under a magnetic field B can be decomposed as [98]:

$$E_B(t) = E_{B=0}(t) + E_{\mathrm{ind},B}(t), \tag{4.7}$$

where $E_{B=0}(t)$ is the transmitted electric field at $B = 0$ and $E_{\mathrm{ind},B}$ is the electric field which arises, in the classical picture, from the holes cyclotron motion induced by the magnetic field. The time-domain CR, or induced electric field, is therefore given by:

$$E_{\mathrm{ind},B}(t) = E_B(t) - E_{B=0}(t). \tag{4.8}$$

This is shown as a red line in Figure 4.3(a) and consists of an exponentially damped waveform with decay time τ. The resulting transmission in the frequency-domain is shown in Figure 4.3(b). Here data are interpolated in order to decrease the space between data points in the frequency domain (from 0.08 to 0.005 THz) by means of

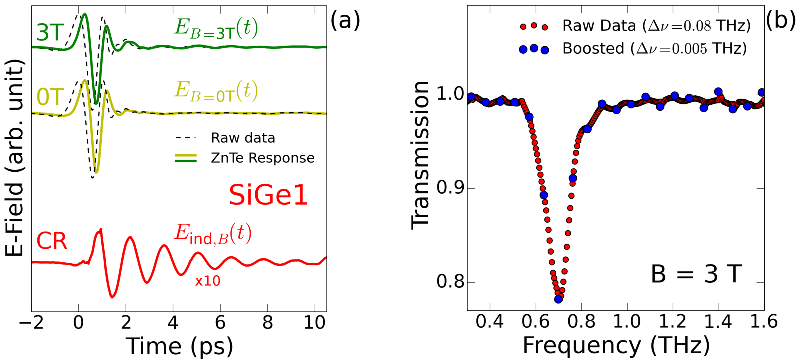

Figure 4.3: (**a**) Transmitted THz-pulses in time-domain through sample SiGe1 at 2 K. Dashed lines are raw data while green and yellow lines are obtained by deconvolving the response of the ZnTe detection crystal, see Section 3.2.2. The red line is the induced electric field ($\times 10$), E_{ind}, see text. (**b**) Transmission in frequency-domain. The resolution is increased by a zero-padding or zero-removal method outlined in Section 3.3.1.

the zero-padding or zero-removal method described in Section 3.3.1. Interpolated points in the frequency domain can make overlapping CRs distinguishable.

In Figure 4.4 the evolution of the CRs with the magnetic field, in the time- (a,c) and the frequency-domain (b,d), is reported for both samples. In the time-domain the damped CR oscillations ($t > 1\,\mathrm{ps}$) can be seen to increase in frequency at higher fields, with a simultaneous reduction in the decay lifetime and the clear presence of beating effects which result from multiple interfering CRs. This can be seen readily in the frequency-domain [Figure 4.4(c,d)]: multiple CRs are distinctly resolved at $B \geq 4.0\,\mathrm{T}$ for SiGe1 and SiGe2. In comparison with sample SiGe1, the weaker CR-absorption in SiGe2 is ascribed to the lower hole density. Moreover, for SiGe2, the CR-waveforms clearly deviate from a single exponential decay even at $B \leq 3\,\mathrm{T}$. This will be demonstrated in Section 4.3.

In a two-dimensional system, cyclotron resonance transitions are permitted between adjacent Landau levels (inter-Landau-level, transitions, $\Delta N = \pm 1$) with the same spin state and with energies $E_{\mathrm{CR}}^{\uparrow\downarrow} = E_{N+1}^{\uparrow\downarrow} - E_{N}^{\uparrow\downarrow}$. The appearance of two distinct CRs, at high B, is direct evidence of the nonparabolicity of the HH-band in Ge-QWs [46]. As mentioned in Section 2.6.1, without Rashba spin-orbit coupling ($\Delta = 0$), the Zeeman splitting of Landau levels (LLs) does not lead to spin-split CRs energies (i.e. $E_{\mathrm{CR}}^{\downarrow} = E_{\mathrm{CR}}^{\uparrow}$) for a *parabolic* band. Conversely, in a *nonparabolic* band, even without the Rashba SOI, both m^* and g^* can differ between adjacent LLs, leading to split-CRs which can be resolved at high magnetic field [58]. In the transmission spectra of both samples at high B, the higher energy CRs ($E_{\mathrm{CR}}^{\downarrow}$)

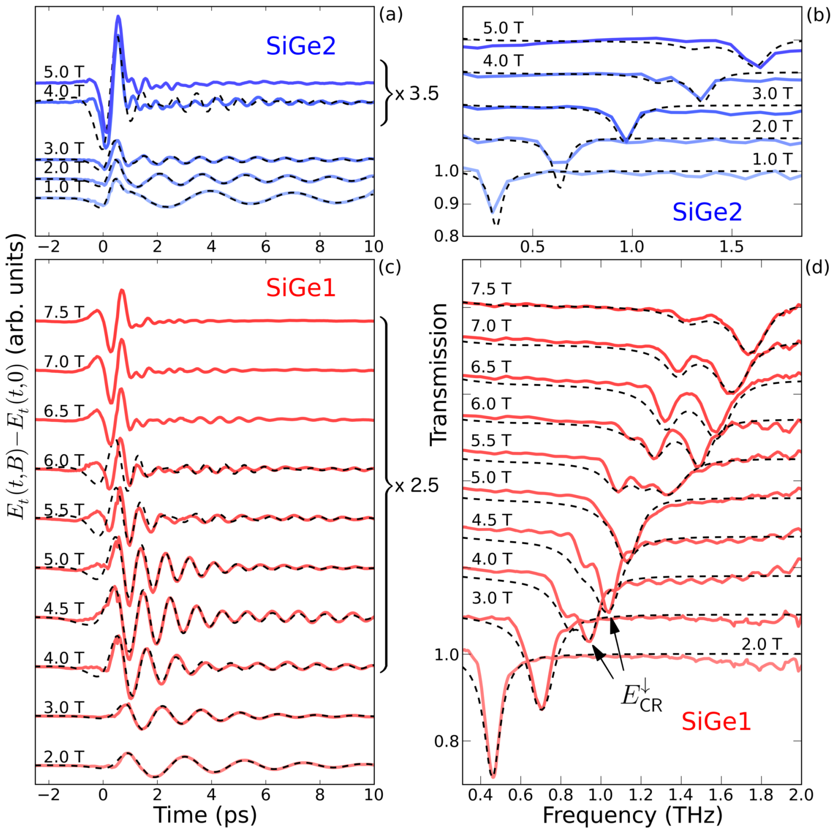

Figure 4.4: (**a,c**) Time-domain CR-waveforms. (**b,d**) Amplitude of the THz transmission, showing split CRs at $B > 3\,\mathrm{T}$ for both samples. Curves are offset vertically for clarity. Dashed black curves are fits obtained as outlined in Section 4.2. These allowed the determination of $N_i, \omega_{c,i}$ and $\tau_{\mathrm{THz},i}$ at different B.

present a smaller transmission which could be related to an higher hole density involved in the spin-down to spin-down transitions [46]. This, as outlined in Section 2.3.1, may be linked to the sub-band dispersion for HH states in the cubic Rashba model which leads to $p_\downarrow > p_\uparrow$, with $p_\downarrow$ and $p_\uparrow$ being the hole density in the spin-down and spin-up states, respectively.

At low magnetic field, where the Zeeman term is weaker, the Rashba term and the nonparabolicity would also lead to split-CRs. However, at this stage it is difficult to argue that the time-domain CR-waveforms without a clear deviation from a single CR-waveform, as well as transmission spectra with a single CR feature, may be effectively composed by more than one CR. This point is clarified in the next section together with the model used to obtain fits reported as dashed lines in Figure 4.4.

4.2 Data analysis

In this section, the Gabor-Morlet wavelet transform is first presented as a straightforward method to analyse the time evolution of the frequency-dependent amplitude of CR-waveforms, and allows the identification of the effective contribution of one or more CRs at different magnetic fields. This is further demonstrated in Section 4.2.2, where the model used to obtain fits in the time- and frequency-domains is outlined.

4.2.1 The Gabor-Morlet wavelet waveform

The Gabor-Morlet wavelet transform $G(\omega, t', \sigma)$ is defined as:

$$G(\omega, t', \sigma) = \int_{-\infty}^{\infty} E_{\mathrm{ind},B}(t) \cdot e^{-t'^2/2\sigma^2} \cdot e^{i\omega t} dt. \tag{4.9}$$

where the second product term within the integral represents a Gaussian centred at time t' and with width defined by σ. A judicious choice of σ in the range $0.5 < \sigma < 2.5\,\mathrm{ps}$ permits the amplitude of the CR (at a certain frequency ω) to be examined at time t', at the expense of a poorer frequency resolution. The time-averaged (Fourier) transform is recovered in the limit $\sigma \to \infty$.

In Figure 4.5(a) the Gabor-Morlet transform is first applied, with width $\sigma = 1.5\,\mathrm{ps}$, to a simulated CR-waveform consisting of a single CR - this has been obtained from Equation 4.14 in the next section, using $E_0(t)$ as the measured transmitted THz-pulse at $B = 0$, cyclotron frequency $f_c = 0.5\,\mathrm{THz}$ and $\tau = 2\,\mathrm{ps}$. The amplitude $|G(\omega, t', \sigma)|$ is also reported for the experimental data of SiGe1 at different magnetic fields in Figure 4.5 (b,c,d), with $\sigma = 1.5\,\mathrm{ps}$. Two temporal regimes can be distinguished. At early times (below 3 ps) $|G|$ exhibits a broadband response corresponding to the driving electric field $E_0(t)$, green waveform. At $t' > 3.5$ ps, $|G|$ evolves into a more narrow-band cyclotron resonance and represents the free-induction decay of the inter-LL transitions. While at B = 5.5 T, Figure 4.5(d), multiple resonances can be clearly resolved, as indicated by the red and blue dashed horizontal lines, at B = 3.0 T and 5.0 T there is no clear splitting either in $|G|$ [Figure 4.5(b,c)] or in the transmission in the frequency-domain [Figure 4.4]. As in the case of the substrate's response in Figure 4.2, this can be related to the fact that the splitting in the frequency-domain is comparable to the linewidth of the CR transitions (Section 2.6.1).

To examine whether a broad resonance consists of multiple narrower resonances, time slices of the Gabor-Morlet amplitude $|G|$ - at fixed frequencies - are

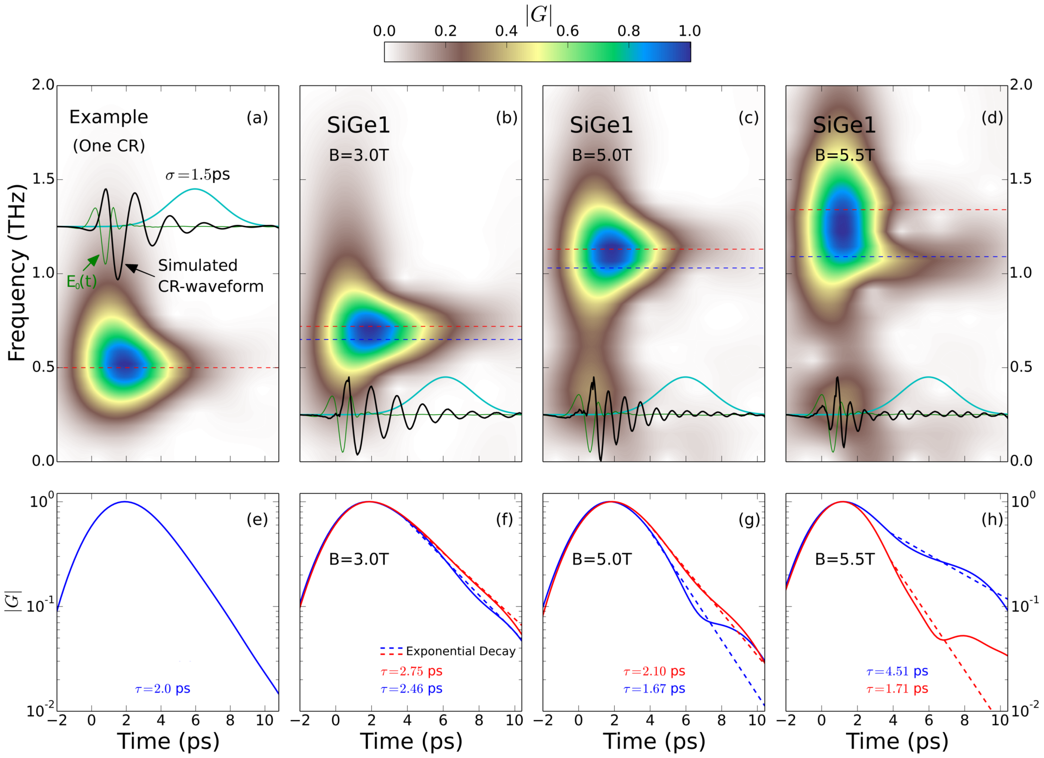

Figure 4.5: Gabor-Morlet wavelet transform of: (**a**) a single CR-waveform simulated using Equation 4.14 [Section 4.2.2]; (**b,c,d**) the experimental CR-waveforms for the SiGe1 sample at different B (black lines). (**e**) Time slice at 0.5 THz [horizontal red dashed line in (**a**)] showing an exponential decay of $|G|$. (**f,g,h**) Deviation from the exponential decay as a result of multiple interfering CRs.

plotted with a logarithmic y axis in Figure 4.5(e-h). Since the CR-waveform in Figure 4.5(a) consists of a single CR, the time slice at $f = 0.5\,\mathrm{THz}$ exhibits an exponential decay with lifetime $\tau = 2\,\mathrm{ps}$ [Figure 4.5(e)]. In Figure 4.5(f-h), the deviation from an exponential decay (dashed lines) indicates that there are multiple, interfering CRs even at $B = 3\,\mathrm{T}$ and $5\,\mathrm{T}$. These CRs present different lifetime τ as a consequence of the different occupancy of the initial and final LL states, see Section 2.6.1. This will be analysed in detail, later in Section 5.8, by calculating the joint density of states. Furthermore, the high frequency resonance at $5.5\,\mathrm{T}$, red lines in Figure 4.5(h), is characterised by a shorter decay time as a result of the broader linewidth, $\Gamma = \hbar/\tau$, in Figure 4.5(d). In conclusion, the Gabor-Morlet waveform provides a sensitive analysis which permits beats between spin-split CRs to be observed.

4.2.2 Modelled CRs in the time- and frequency-domains

This section outlines the fitting methods in the time- and frequency-domain used to estimate frequencies, carrier densities and lifetimes of the i-th CR at different B. Modelling the transmission in both domains assures precision in evaluating these parameters. The origin of the induced electric field in the time-domain, given by Equation (4.3), is first explained using both the quantum mechanical and classical approach. Secondly, the parallel agreement of the simulations in both domains is deeply analysed in order to clarify the presence of more CRs at different B.

Quantum mechanics view. In the quantum mechanical view every CR can be seen as a two-level system where holes are excited from the LL state $|1\rangle$ to $|2\rangle$ with an energy difference $E_2 - E_1$ defining the cyclotron frequency $\omega_c = (E_2 - E_1)/\hbar$. The density matrix formalism describes the dynamics of such a system by solving the Optical Bloch Equations (OBEs), as described for instance in Arikawa *et al.* [101]. For short pulses, the analytic solutions of the OBEs are provided by a perturbation theory which, in the first order, leads to the homogeneous free decay of the diagonal element ρ_{12} of the density matrix as a result of the interaction with an electric field $E_0(t)$:

$$\rho_{12}(t) = e^{-i\omega_c t} i \int_{-\infty}^{t} e^{-(t-t')/\tau} E_0(t') e^{i\omega_c t'} \, dt'. \tag{4.10}$$

The two-level system defines a macroscopic polarization $P = 2N_{\text{sys}}\mu_{12}\text{Re}[\rho_{12}]$, where μ_{12} is the dipole matrix element between the considered states and N_{sys} is the number of two-level systems. The induced electric $E_{\text{ind},B}(t) \propto dP/dt$ has frequency ω_c and decay rate $1/\tau$.

Classical view. In the classical (Drude) picture, the cyclotron motion of holes within the quantum well in the i-th state, with a density p_i and effective mass m_i^*, is described by the dynamical conductivity [98]:

$$\sigma_i(t) = [2\pi p_i e^2/m_i^*] e^{-t/\tau_i} \cos \omega_{c,i} t \, . \tag{4.11}$$

The interaction of the THz field with holes defines an induced current:

$$\begin{aligned} j_{\text{ind},i}(t) = \int_{-\infty}^{t} E_0(t')\sigma_i(t-t') \, dt' = \\ = [2\pi p_i e^2/m_i^*] \int_{-\infty}^{t} E_0(t') e^{-(t-t')/\tau_i} \cos\left[\omega_{c,i}(t-t')\right] dt', \end{aligned} \tag{4.12}$$

which has a structure similar to Equation (4.10). In this picture, the reemitted THz field due to the i-th transition, $E_{\text{ind},i} \sim dj_{\text{ind},i}/dt$, can be written as [98]:

$$E_{\text{ind},i}(t) \;=\; [2\pi p_i e^2/m_i^*]\sqrt{\omega_{c,i}^2 + 1/\tau_i^2} \;\times\; \int_{-\infty}^{t} E_0(t')e^{-(t-t')/\tau_i}\cos[\omega_{c,i}(t-t')]\,dt'. \tag{4.13}$$

The normalised experimental CR-waveforms at different B were fitted by taking into account the sum of the i-th CR arising from transitions between different LLs:

$$E_{\text{ind}}(t) = \sum_i A_i \int_{-\infty}^{t} E_0(t')e^{-(t-t')/\tau_i}\cos[\omega_{c,i}(t-t')]\,dt', \tag{4.14}$$

owing to the determination of the frequency, effective mass and lifetime of the CRs contributing to $E_{\text{ind}}(t)$.

Considering different lifetimes for the CRs is justified by the different occupation of initial and final states - as in the transition scheme of Figure 2.22 - as well as by the Gabor-Morlet analysis in Section 4.2.1.

Modelled transmission. As Equation (4.14) was used to fit the normalised CR-waveforms, the factors A_i were varied between 0 and 1. The determination of p_i was achieved by using $\omega_{c,i}$, m_i^* and τ_i, obtained from the CR-waveform fits, to simulate the transmission in the frequency-domain by means of the stack model outlined in Section 4.1.2. The i-th contribution to $T_B(\omega)$ was taken into account by modelling the complex refractive index for the Ge-QWs, as given by Equation (4.5). The depth of the transmission spectra at the cyclotron frequency $f_{c,i}$ is related to p_i through the conductivity $\sigma_i(\omega)$ defined in Equation (4.6) or to the tensor element σ_{xx} in Equation (2.65).

To clarify the adopted model, it is useful to first consider the CR-waveform and the transmission spectrum at $B = 5.5\,\text{T}$ for the SiGe1 sample reported in Figure 4.6(c,f), respectively. The modelled CR-waveform, black line, agrees well using three CRs (as clearly resolved in the transmission spectrum) whose waveforms are plotted with different colours and present different phase, frequency, decay time and amplitude. The strongest contribution (purple) with $A_1 = 0.57$ corresponds to the highest cyclotron frequency, $f_{c,1}$. Once the density p_1 was determined such that the related conductivity σ_1 led $T_B(\omega)$ to reach the same depth as the experiment at $f_{c,1}$,

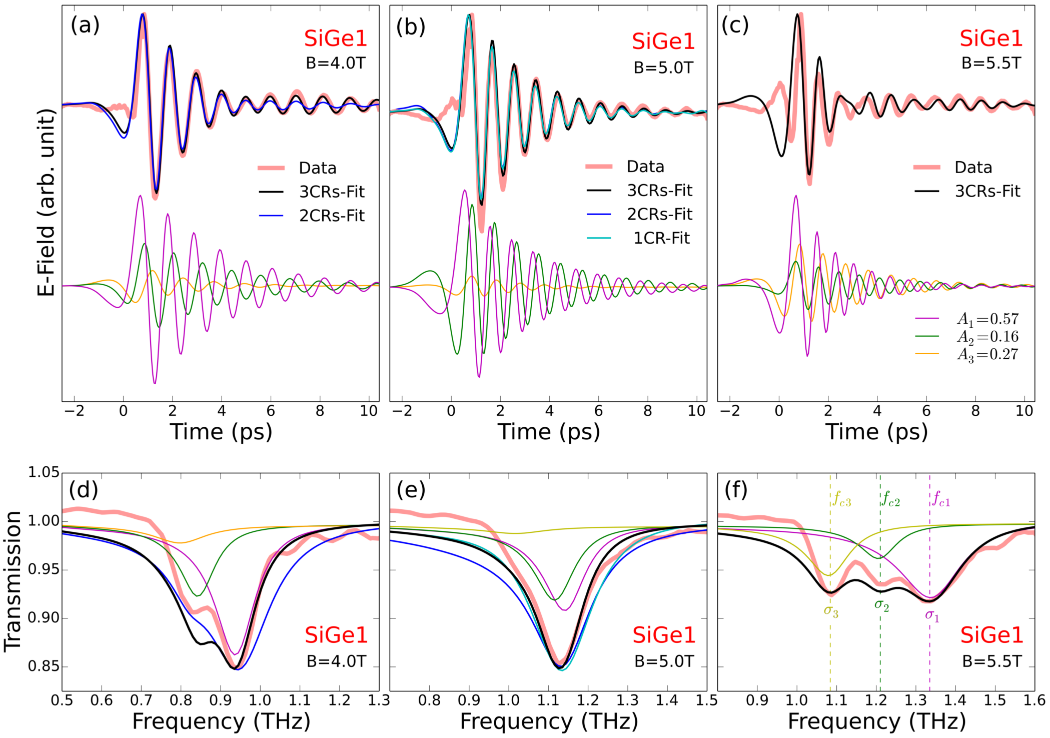

Figure 4.6: Examples of modelled CR-waveforms and transmission spectra for the sample SiGe1. (**a,b,c**) Comparison of the agreeement of fits with data (thick red line) in the time-domain which considered the contribution of three (black line) or two (blue) or one CR (cyan). The contribution of the different CRs, in the case of the 3CRs-fit, are plotted in the bottom part of the figure (purple, green and yellow lines). (**d,e,f**) Comparison of the agreement in the frequency-domain with parameters obtained from the time-domain fits above.

the hole density p_i, which participates in the i-th transition, was determined using:

$$p_i = p_1 \frac{A_i}{A_1} \sqrt{\frac{\omega_{c,1}^2 + 1/\tau_1^2}{\omega_{c,i}^2 + 1/\tau_i^2}}. \tag{4.15}$$

Here the other parameters are as obtained from the time-domain fits. The modelled conductivity $\sigma = \sum_i \sigma_i$ results in a simulated transmission (black line) which well agrees with the experiment (red line).

For $B \geq 4\,\mathrm{T}$, three CRs were used for the SiGe1 sample. For instance, at $B = 4\,\mathrm{T}$ - where two CRs are resolved in the transmission - the best fit was obtained in both domains by considering three CRs [Figure 4.6(a,d)]. At $B = 5\,\mathrm{T}$ in Figure 4.6(b), fitting with three CRs (black line), instead of two (blue line), does not effectively improve the agreement between fit and data but, as shown in Figure

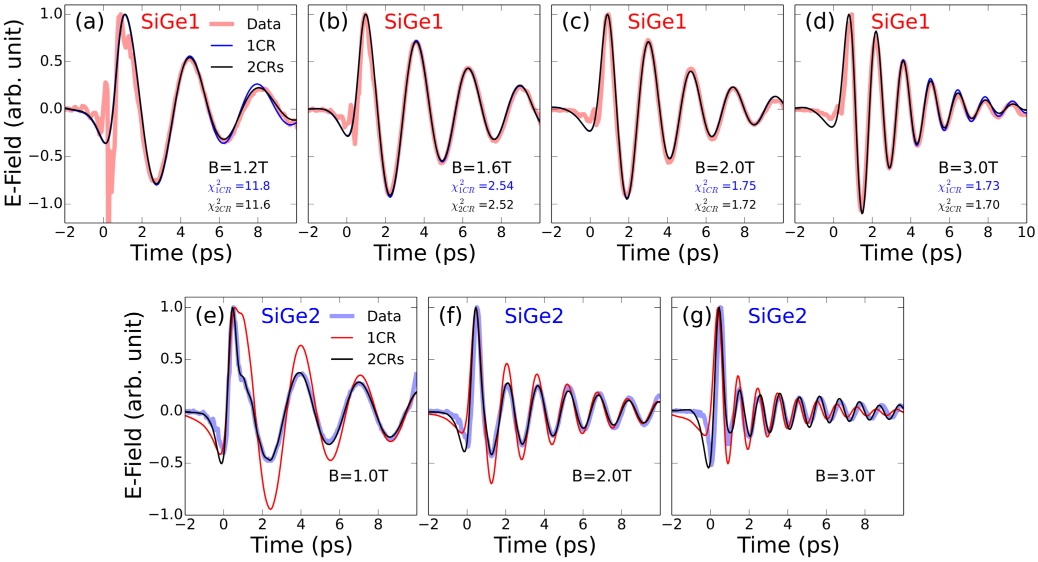

Figure 4.7: Comparison between time-domain fits obtained using one or two CRs for $B \leq 3\,\mathrm{T}$. (**e,f,g**) SiGe1 data CR-waveforms (red lines) and fits which consider one CR (blue line) and two CRs (black line). Values of χ^2 indicate the different agreement. The deviation from a single exponential is evident at $B = 1.2$ (**a**) and $3.0\,\mathrm{T}$ (**d**). (**e,f,g**) Clear deviation from a single CR-waveform (red line) and the two CRs fit (black) for SiGe2.

4.6(e), the latter case does not agree as well as in the three CRs case. Conversely, the comparable agreement with data for the one (cyan line) and three CRs fits in the frequency-domain transmission of Figure 4.6(e) does not give rise to the same agreement with the CR-waveform in Figure 4.6(b)

In conclusion, as the relative depth of the different features is well reproduced for the two samples, the agreement given by transferring the time-domain parameters to the frequency-domain is clearly visible in Figure 4.4.

4.3 Low magnetic field range at T=2K

Even if clear split-CRs in the frequency domain - or beating effects in the time domain - are not resolved for SiGe1 at $B = 3.0\,\mathrm{T}$ and at $B = 5.0\,\mathrm{T}$ [see Figure 4.4(c,d)], the Gabor-Morlet transform analysis presented in Figure 4.5 shows an evident deviation from a single exponential decay. For this reason it was worth comparing time-domain fits obtained by assuming one or two CRs for $B \leq 3\,\mathrm{T}$.

In Figure 4.7 this comparison shows a smaller residual ($\chi^2 = |E^{\mathrm{exp}}_{\mathrm{ind}} - E^{\mathrm{fit}}_{\mathrm{ind}}|^2$) between fit and experiment by using two CRs instead of one. While the CR-waveforms below $3\,\mathrm{T}$ appear, at first glance, to decay exponentially, there is a deviation from single exponential decay that is clearly visible at $B = 1.2\,\mathrm{T}$ and

3.0 T. Using one CR gave rise to the lowest residual at $B = 1.0, 1.4, 1.8\,\mathrm{T}$. The CR frequencies for spin-up to spin-up and spin-down to spin-down transitions can be similar when LLs overlap, as sketched in Figure 2.22(a). For instance, a time-domain fit at 1.6 T with two CRs produces $f_{c,1} = 0.3634\,\mathrm{THz}$ and $f_{c,2} = 0.3640\,\mathrm{THz}$ (i.e. a difference $\Delta f_c = 0.0006\,\mathrm{THz}$, so effectively one CR), while at 1.2 T a two CR fit yields a much larger $\Delta f_c = 0.04\,\mathrm{THz}$.

Thus, for SiGe1, the Gabor-Morlet transform analysis, as well as the comparison of the fits above demonstrate that two CRs clearly participate in the CR-waveforms. The presence of two distinguished CRs at low magnetic field, where the Zeeman term does not strongly contribute, demonstrates the presence of the Rashba SOI within the Ge-QWs.

For SiGe2, fits were obtained by considering two CRs in the whole magnetic field range. The time-domain oscillations of the CR-waveforms in Figure 4.7(e,f,g) do not show clear, single-frequency decays with exponential envelopes, and these were therefore not possible to fit with just one CR. This is clearly evident by comparing fits with one (red lines) and two CRs (black lines).

4.3.1 Hole density and effective mass

The fitted p_i were averaged over $1 \leq B \leq 3\,\mathrm{T}$, where two CRs were used to fit data, giving values for $p_\downarrow^{\mathrm{THz}}$ (corresponding to the highest cyclotron frequencies) and $p_\uparrow^{\mathrm{THz}}$ (lowest cyclotron frequencies), see Figure 4.9. These values are reported in Table 4.2 and were used to get $p_{\mathrm{2D}}^{\mathrm{THz}} = p_\downarrow^{\mathrm{THz}} + p_\uparrow^{\mathrm{THz}}$ [74], corresponding to spin polarizations $(p_\downarrow^{\mathrm{THz}} - p_\uparrow^{\mathrm{THz}})/(p_\downarrow^{\mathrm{THz}} + p_\uparrow^{\mathrm{THz}})$ of 7.2 % for SiGe1 and 3.2 % for SiGe2.

Magnetotransport (MT) measurements for SiGe1 [75] revealed beatings in the Shubnikov-de Haas oscillations (SdH) (Section 2.5.2) and led to the determination of spin-split densities $p_{\uparrow\downarrow}^{\mathrm{MT}}$. These are also reported in Table 4.2 for comparison. For the SiGe1 sample, the spin polarisation obtained from MT-measurements (6.6%) is in line with values determined from THz-TDS. A contribution from the B:SiGe supply layer, which is above the Ge-QW in SiGe2 (normal modulation doped QW),

Sample	$p_\downarrow^{\mathrm{THz}}$	$p_\uparrow^{\mathrm{THz}}$	$p_{\mathrm{2D}}^{\mathrm{THz}}$	$p_\downarrow^{\mathrm{MT}}$	$p_\uparrow^{\mathrm{MT}}$
SiGe1	5.2 ± 0.2	4.5 ± 0.2	9.7 ± 0.3	6.31	5.53
SiGe2	1.6 ± 0.3	1.5 ± 0.3	3.1 ± 0.4	-	-

Table 4.2: Hole density ($\times 10^{11}\,\mathrm{cm}^{-2}$) from THz-TDMS experiments: spin-down LLs ($p_\downarrow^{\mathrm{THz}}$); spin-up ($p_\uparrow^{\mathrm{THz}}$) and total density ($p_{\mathrm{2D}}^{\mathrm{THz}}$). Magnetotransport spin-down ($p_\downarrow^{\mathrm{MT}}$) and spin-up ($p_\uparrow^{\mathrm{MT}}$) density [75]. For SiGe2, a contribution from the B:SiGe supply layer prevented the observation of the beating effect in the SdH-oscillation.

Sample	m^*_{THz} (m_0)	m^*_{MT} (m_0)	m^*_b (m_0)
SiGe1	0.115 ± 0.003	0.095	0.103 ± 0.002
SiGe2	0.083 ± 0.005	0.065	0.087 ± 0.002

Table 4.3: Effective masses obtained from the linear fit of the cyclotron frequency (m^*_{THz}) and from magnetotransport measurements (m^*_{MT}) [75].

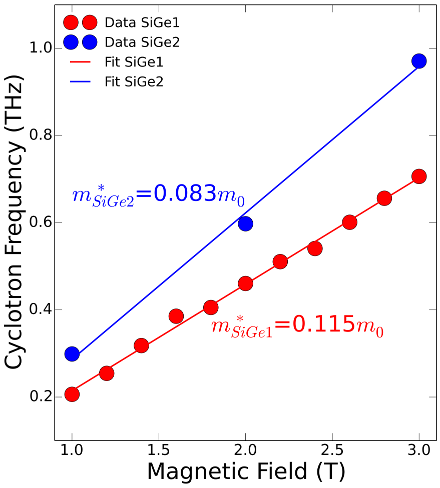

Figure 4.8: Effective mass evaluation from $f_c = eB/2\pi m^*$.

prevented the observation of the beating effect in the SdH-oscillation. Conversely, results from THz time-domain cyclotron spectroscopy were not influenced by holes in the B:SiGe supply layer (which have higher m^* than holes in the QW [50], and should result in absorption features at different frequencies).

Heavy-hole effective masses were determined by linear fits (shown in Figure 4.8) of the CR frequencies, in the same magnetic range as used for the density evaluation. The obtained values are reported in Table 4.3 (m^*_{THz}) together with the effective masses from MT-measurements (m^*_{MT}). Owing to its higher density in comparison with SiGe2, since μ lies at higher energies, the heavier mass in SiGe1 is a consequence of the nonparabolicity.

As reported in Section 3.4.1, for a Ge content $x = 0.8$ and at $k = 0$, the energy difference between the HH- and LH-band is $\sim 40\,\mathrm{meV}$ [see Figure 3.4(b)]. By using the densities and effective masses obtained, the Fermi energy, $E_{\mathrm{F}} = 2p^{\mathrm{THz}}_{2\mathrm{D}}\hbar/m^*_{\mathrm{THz}}$, can be calculated. This results to be $\sim 20\,\mathrm{meV}$ and $\sim 8\,\mathrm{meV}$ for the SiGe1 and SiGe2 samples, respectively. By still referring to Figure 3.4(b), since the absolute value of the LH-band energy - for 0.8% Ge - is higher than the evaluated E_{F}, at

Sample	β_p (10^{-28} eVm^3)	Δ_p (meV)	β (10^{-28} eVm^3)	Δ (meV)	β_{MT} (10^{-28} eVm^3)
SiGe1	0.9 ± 0.3	2.8 ± 0.8	0.5 ± 0.1	1.6 ± 0.2	1.0 ± 0.6
SiGe2	1.2	0.6	1.2 ± 0.4	0.6 ± 0.2	-

Table 4.4: Cubic Rashba coefficients and energy splitting evaluated from: the spin-resolved sub-band densities using Equation (2.52)(β_p, Δ_p); the magnetic-field dependence of the cyclotron splitting energy from the transition between LLs obtained by modelling the experimental CR energies (Figure 4.10)(β, Δ); the SdH oscillations (β_{MT}) [75]. As SiGe2 is a normal modulation doping structure (see Figure 3.3(a) and Table 3.1), the contribution from the B:SiGe supply layer, in between the Hall-bar and the QW, prevented the determination of β_{MT} from the analysis of SdH oscillations.

these densities only the HH band is occupied at 2 K.

4.3.2 First evaluation of the Rashba splitting energy

For holes in the HH-band, where the splitting energy is cubic in the k-space, a first evaluation of the cubic Rashba coefficient can be performed by using the determined spin-split sub-band densities $p_\downarrow$, $p_\uparrow$ - see Section 2.3.1 and Equation (2.52). The required expression is [46]:

$$\beta_p = \sqrt{\frac{2}{\pi}} \frac{\hbar^2}{2m^*} \frac{p(p_+^* - p_-^*) + \Delta p(p_+^* + p_-^*)}{6p^2 + 2(\Delta p)^2} \tag{4.16}$$

where $p = p_\downarrow + p_\uparrow = p_{2\mathrm{D}}^{\mathrm{THz}}$, $\Delta p = |p_\uparrow - p_\downarrow|$, and $p_\pm^* = \sqrt{p \pm \Delta p}$. Performing this analysis, by using the hole densities and effective masses (m_{THz}^*) reported in Table 4.2 and Table 4.3, results in values of the Rashba coefficient (β_p) as reported in Table 4.4 together with the spin-splitting energy:

$$\Delta_p = 2\beta k_{\|}^3 \simeq 2\beta k_{\mathrm{F}}^3, \tag{4.17}$$

where $k_{\|} \simeq k_{\mathrm{F}} = \sqrt{2\pi p_{2\mathrm{D}}^{\mathrm{THz}}}$. Since the HH energy is close to μ, here k_{F} is the Fermi wave vector. For comparison, the spin-split density and effective mass obtained from MT measurements (Table 4.3 and 4.3) results in $\beta_{\mathrm{MT}} = 1.0 \pm 0.6 \times 10^{-28}$ eVm^3 and in agreement with the values from THz-TDS (Table 4.4). For the SiGe2 sample, experimental transmissions were acquired with magnetic field steps of 1 T, therefore errors are not given due to the poorer statistics.

4.4 Landau level calculations

In Section 2.6 the quantum description of CRs between LLs has been outlined together with a full calculation for a Ge-QW on a $\mathrm{Si}_{0.5}\mathrm{Ge}_{0.5}$ buffer layer (Figure 2.22). CR transitions were described by means of the absorption coefficient α in Equation (2.89). Since calculating α needs a precise knowledge of the hole wavefunctions, the following section firstly introduces (Section 4.4.1) an useful approximation to calculate LLs - as proposed by Winkler [46] - whose B-evolution considers the effect of the linear SIA spin-splitting (see Section 2.3). By considering that the obtained densities in Section 4.3.1 indicate that only the first HH-subband is occupied in the sGe-QWs investigated in this chapter, an adaptation of the Winkler's approximation - for a general SIA spin-splitting - is outlined in Section 4.4.2, where the effect of nonparabolicity is also investigated. This must be taken into account to obtain spin-split CRs, whose energy splitting increases with magnetic field as reported in Figure 4.4(b,d) or Figure 2.22. The outlined model is then used in Section 4.4.3 in order to reproduce CR energies obtained from the time- and frequency-domain fits at different magnetic fields (Section 4.2). This approach, besides offering another way to evaluate the Rashba spin-splitting energies (a first evaluation was reported in Section 4.3.2), also allows the estimation of the g-factors for the investigated samples.

4.4.1 2D-systems with linear SIA

The influence of the Rashba spin-splitting on LLs can be obtained by considering the EFA Hamiltonian in Equation (2.80) and adding the Rashba term for electrons given in Equation (2.42). By replacing k_+, k_- with the definition of creation and annihilation operators in Equation (2.79), the Rashba-term reads [46]:

$$H_{6c6c}^{\mathrm{SIA}} = \sqrt{\frac{2eB}{\hbar}}\alpha \begin{pmatrix} 0 & ia \\ -ia^{\dagger} & 0 \end{pmatrix}, \tag{4.18}$$

and the Hamiltonian for the in-plane motion results in LL-energies which depend on both Zeeman and Rashba splitting-energy as:

$$\begin{aligned} E_{8c,n,\mathcal{N}}^{\pm} = E_{mn}(\boldsymbol{k}_0) + \hbar\omega_{\mathrm{c}}\left(\mathcal{N} + \frac{1}{2} \pm \frac{1}{2}\right) \\ \mp \frac{1}{2}\sqrt{(\hbar\omega_{\mathrm{c}} - g^{*}\mu_B B)^2 + 8\alpha^2\frac{eB}{\hbar}\left(\mathcal{N} + \frac{1}{2} \pm \frac{1}{2}\right)}. \end{aligned} \tag{4.19}$$

The Rashba splitting energy for electrons can be defined as $\Delta_\alpha = |E_+^{\mathrm{CB}}(\boldsymbol{k}_\parallel) - E_-^{\mathrm{CB}}(\boldsymbol{k}_\parallel)| = 2\alpha k_\parallel$ [see Equation (2.44)]. This can be written as a function of the sheet density N_s by assuming $k_\parallel \simeq k_{\mathrm{F}} = \sqrt{2\pi N_s}$.

4.4.2 General SIA spin-splitting and nonparabolic corrections

In the following, Equation (4.19) is adapted for a general Rashba spin-splitting (Section 2.3). Furthermore, a non-parabolicity correction for effective masses and g factors is also introduced.

The Rashba spin-splitting for electrons Δ_α can be considered in terms of a general Rashba splitting energy Δ_m (where m denotes the m-th bulk subband, see Section 2.2.1) such that:

$$8\alpha^2 \frac{eB}{\hbar} = \frac{eB}{\pi\hbar N_s}\Delta_m^2. \tag{4.20}$$

By explicitly writing the magnetic quantum number m_j for a particular bulk band ($m_j = 1/2$ for electrons and LHs, $m_j = 3/2$ for HHs), Equation (4.19) becomes:

$$\begin{aligned} E^{\pm}_{m,n,\mathcal{N}} = E_{mn}(\boldsymbol{k}_0) + \hbar\omega_{\mathrm{c}}\left(\mathcal{N} + \frac{1}{2} \pm m_j\right) \\ \mp m_j\sqrt{(\hbar\omega_{\mathrm{c}} - g^*\mu_B B)^2 + \frac{eB}{\pi\hbar N_s}\Delta_m^2(\mathcal{N} + \frac{1}{2} \pm m_j)}. \end{aligned} \tag{4.21}$$

If one considers LLs as δ-functions, i.e. without considering the LL-broadening outlined in Section 2.5.1, CRs are simply given by:

$$E^{\pm}_{\mathrm{CR}} = |E^{\pm}_{\mathrm{HH},1,\mathcal{N}} - E^{\pm}_{\mathrm{HH},1,\mathcal{N}+1}|. \tag{4.22}$$

where $E^{\pm}_{\mathrm{CR}}$ indicates CR-energies obtained as transitions ($\Delta\mathcal{N} = 1$) from spin-up to spin-up states ($E^{+}_{\mathrm{CR}} = E^{\uparrow}_{\mathrm{CR}}$), and from spin-down to spin-down states ($E^{-}_{\mathrm{CR}} = E^{\downarrow}_{\mathrm{CR}}$). Here CRs with conserved spin are considered as the absorption coefficient in Equation (2.89) has nonvanishing matrix elements only if $\Delta\mathcal{N} = 1$ and the spin does not change. Furthermore, in comparison with α in Equation (2.89), the considered CR-transitions do not take into account the occupation factors. These will be considered later in Section 5.8 in order to calculate the joint density of states (JDOS) and qualitatively explain the presence of further CRs at low magnetic field for another set of QWs with 1.3% compressive strain.

Zeeman, Rashba and nonparabolicity effects. By means of Equation (4.21)

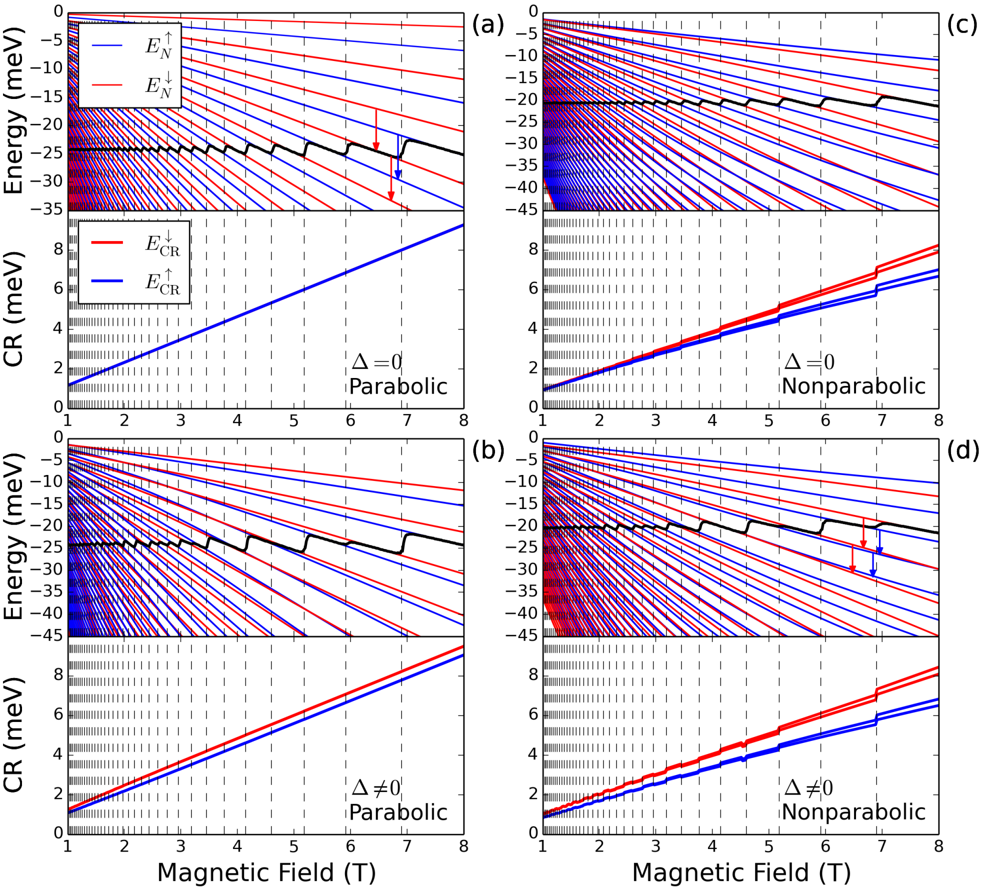

Figure 4.9: Approximated LL-calculation [Equation 4.21] for the first subband of a square QW by assuming: (**a**) parabolic dispersion without SIA ($\Delta = 0$); (**b**) parabolic dispersion and SIA ($\Delta \neq 0$); (**c**) nonparabolic dispersion [effective mass and g-factor by means of Equations (4.24) and (4.23)], neglecting SIA; (**d**) nonparabolic dispersion with SIA. CRs obtained by considering δ-function LLs [i.e. neglecting the real absorption in Equation (2.89))]. Double lines for $E_{\mathrm{CR}}^{\downarrow\uparrow}$ arise from transition towards occupied states close to the chemical potential.

and neglecting the Rashba-term ($\Delta_{\mathrm{HH}} = 0$), Figure 4.9(a) shows calculated LLs for the first HH-subband ($E_{\mathrm{HH},1}(\boldsymbol{k}_0) = (\hbar^2\pi^2)/(2m^*_{\mathrm{HH}}L^2)$) of a square QW, together with CR-energies ($E_{\mathrm{CR}}^{\downarrow\uparrow}$) indicated by blue and red arrows for spin up-to-up, and spin down-to-down transitions, respectively. In this first case, no spin-split CRs are obtained since the Zeeman energy does not depend on the LL-index $\mathcal{N}$. As shown in Figure 4.9(b), if we now add the Rashba contribution ($\Delta_{\mathrm{HH}} \neq 0$) the model results in split-CRs whose energy difference remains constant over the considered B-range. Like in the Zeeman effect, this is due to the fact that Δ does not depend on $\mathcal{N}$ in Equation (4.21).

As discussed in describing Winkler's calculation in Figure 2.22(a), spin-split

CRs can arise from the strong nonparabolicity of the HH-band, owing to the interaction with the LH and SO bands [46], which affects m^* and g^* as well as the Fermi energy. The nonparabolicity can be approximated with an energy-dependence [102]:

$$g^*(E) = g_0(1 - \alpha_{\mathrm{NP}} E), \tag{4.23}$$

and

$$m^*(E) = m_b^*\Big(1 + 2\frac{E}{E_g}\Big), \tag{4.24}$$

where $E = E^{\pm}_{m,n,\mathcal{N}}$, E_g is the energy gap of the QW and m_b^* is the band-edge effective mass, that is at $k_{\parallel} = 0$. The effective mass nonparabolicity enters in the cyclotron resonance $\omega_{\mathrm{c}} = eB/m^*(E)$. The substitution of the nonparabolic effective mass into Equation (2.38), for the Fermi energy of a square QW, results in:

$$E_{\mathrm{F}} = \frac{\hbar^2 \pi N_s}{m^*(E)} = \frac{\hbar^2 \pi N_s}{m_b^*\Big(1 + 2(E_{\mathrm{HH},1} + E_{\mathrm{F}})/E_g\Big)}. \tag{4.25}$$

The above identity leads to a quadratic equation whose physical solution, by considering $E_{\mathrm{HH},1} \ll E_g$, is:

$$E'_{\mathrm{F}} = \frac{-E_g + \sqrt{\mathcal{A}}}{2} \quad \text{where} \quad \mathcal{A} = E_g^2 + 4\bigg(E^2_{\mathrm{HH},1} + E_{\mathrm{HH},1}E_g + \frac{N_s \pi \hbar^2 E_g}{m_b^*}\bigg). \tag{4.26}$$

In detail, $E_{\mathcal{N}}$ are LLs firstly obtained without the Rashba contribution, as from Equation (2.82) or, equivalently, from Equation (4.21) with $\Delta_{\mathrm{HH}} = 0$ - essentially the LLs in Figure 4.9(a). The LLs for the parabolic subband are used to obtain the corrected $g^*(E_{\mathcal{N}})$, $m^*(E_{\mathcal{N}})$ and E'_{F} which act as new inputs to calculate LLs with the nonparabolic correction. These are shown in Figure 4.9(c,d) for $\Delta_{\mathrm{HH}} = 0$ and $\Delta_{\mathrm{HH}} \neq 0$, respectively. In line with the full calculations shown in Figure 2.22(a), the nonparabolicity results in overlapping LLs and split-CRs whose energy difference increases gradually with B, as also obtained in experiments within this chapter (Figure 4.4). Furthermore, the case $\Delta_{\mathrm{HH}} \neq 0$ gives rise to split CRs already at low magnetic fields, where the contribution of the Zeeman splitting can be neglected [46]. As outlined in Section 2.6.1, CRs appear and disappear at integer filling factor ν, owing to the evolution of the LL occupancy. As the model considers δ-function LLs (width $\Gamma = 0$, see Section 2.5.1), i.e. neglecting disorder [44], two transitions between spin-down LLs (with energy $E^{\downarrow}_{\mathrm{CR}}$, red lines) and two transitions between spin-up LLs ($E^{\uparrow}_{\mathrm{CR}}$, blue lines) are considered in the model because Γ may result in an overlap between the last two occupied LLs, giving rise to up to four CRs, as depicted in Figure 2.22(c,d,e,f).

4.4.3 Evaluated Rashba spin-splitting and g-factor

Figure 4.9(d) clearly indicates that the magnetic field evolution of the spin-down and spin-up LLs ($E_N^{\uparrow\downarrow}$) depends on the combined influence of the Zeeman effect, Rashba spin-orbit coupling as well as of the nonparabolicity. In the following section, Equation (4.21) is used to model the evaluated CRs (Section 4.2) in order to estimate crucial quantities such as Δ_{HH} (what follows will consider the notation $\Delta_{\mathrm{HH}} \equiv \Delta$) and g^* for the sGe-QWs characterised in this chapter.

The nonparabolicity is taken into account by means of Equations (4.23) and (4.24) with:

$$E = E_1 + E_{\omega_c,N}^{\uparrow\downarrow} + E_{\mathrm{Zeeman}}^{\uparrow\downarrow}, \tag{4.27}$$

where $E_1 = \hbar^2\pi^2/2m_b^* L_{\mathrm{QW}}^2$ is the ground state energy for a rectangular well with thickness L_{QW}, while $E_{\omega_c,N}^{\uparrow\downarrow} + E_{\mathrm{Zeeman}}^{\uparrow\downarrow}$ are the LL energies in the parabolic case without the SOI contribution, i.e.:

$$E_{\omega_c,N}^{\uparrow\downarrow} + E_{\mathrm{Zeeman}}^{\uparrow\downarrow} = \hbar\omega_c(N + 1/2) \pm m_J g_0 \mu_B B. \tag{4.28}$$

In Figure 4.10(a,b) the calculated Landau level energies, obtained by considering the nonparabolicity above - and calculated as explained in Section 4.4.2 - are reported for SiGe1 and SiGe2. The chemical potential μ_{F} (black lines) jumps between different LL energies E_N when ν is an integer, at values of B (vertical dashed lines) obtained considering $B = h\rho_{2\mathrm{D}}/e\nu$ with $\rho_{2\mathrm{D}} = \rho_{2\mathrm{D}}^{\mathrm{THz}}$ in Table 4.2.

The transitions are shown in Figure 4.10(c,d) and in good agreement with the CR energies ($\hbar 2\pi f_c$) obtained from fits in Section 4.2. Both Rashba and Zeeman splitting effects were required to model the full range of magnetic fields for both samples. The energy splitting Δ and the related Rashba coefficient β [from Equation (4.17)] are reported in Table 4.4 and in line with Δ_p and β_p obtained from the evaluated spin-split hole densities [Equation (2.52)]. Best fits at high B required a nonparabolicity factor $\alpha_{\mathrm{NP}} = 3 \times 10^{-5}\,\mathrm{eV}^{-1}$ for both samples, with $g_0 = 3.2$ for SiGe1 and $g_0 = 7.0$ for SiGe2. These are in line with the value of $g^* = 4.3$ reported for a 15 nm thick Ge-QW [103], and with the expectation that g increases in magnitude for wider wells as the bulk limit is approached [46]. The evaluated band edge values of the effective masses were as reported in Table 4.3.

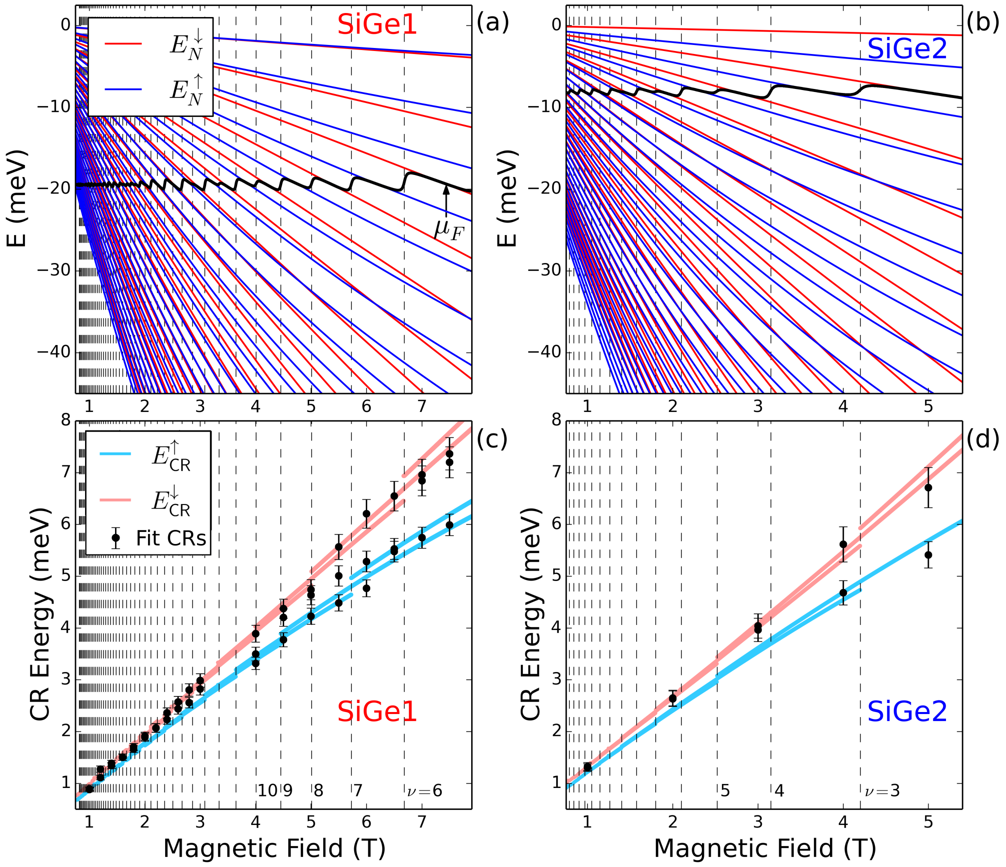

Figure 4.10: (**a,b**) Heavy-hole Landau levels for SiGe1 and SiGe2, respectively, calculated from Equation (4.21) with parameters as described in the text. The black dashed vertical lines are the magnetic field values for which the filling factor ν is an integer. The thick black line describes the evolution of the chemical potential μ with the magnetic field. (**c,d**) Calculated (lines) and experimental (points) cyclotron energies for transitions between spin up ($m_J = 3/2$, blue lines) and spin down ($m_J = -3/2$, red lines) states.

Strain-dependence of Δ. As presented in Section 2.3.2, a previous study of a Ge-QW (with 2.1% strain) reported a spin-splitting energy $\Delta = 0.3 - 0.4\,\mathrm{meV}$ (tuned by an electric field) [59], corresponding to a cubic Rashba coefficient $\beta = 0.1 - 0.07 \times 10^{-28}\,\mathrm{eV\,m^3}$. The strong increase in β reported here for SiGe1 and SiGe2 can be attributed to the lower strain used in the present study (0.8% instead of 2.1%) [59, 53]. As shown in Figure 3.4, the reduced strain leads to a ~ 2.75 times smaller HH-LH energy splitting [50]($\sim 40\,\mathrm{meV}$ instead of $\sim 110\,\mathrm{meV}$ in Ref. [59]). Using $\beta \propto 1/(E_{\mathrm{HH}} - E_{\mathrm{LH}})^2$ for the Rashba coefficients dependence on HH-LH splitting - see Section 2.3.2 and Equation (2.57) - this leads to an approximately 8-fold increase in β, in reasonable agreement with the observed values.

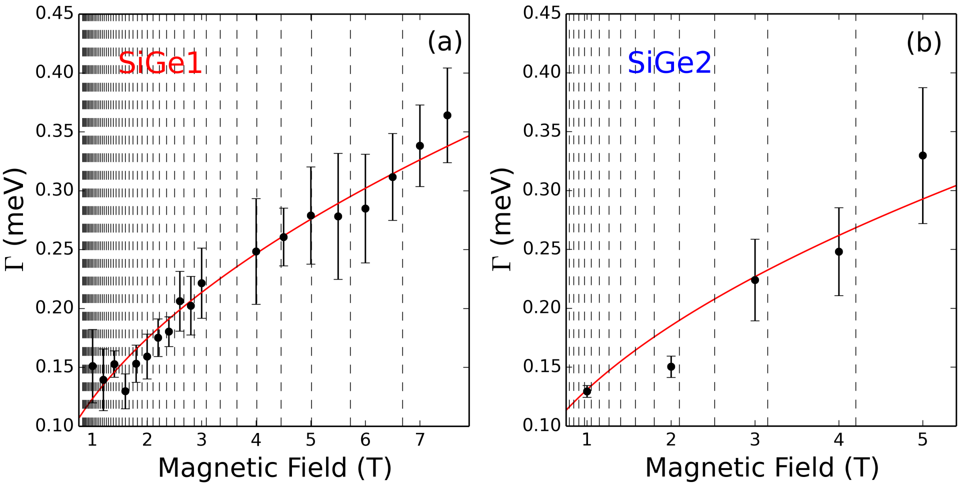

Figure 4.11: Landau level width $\Gamma = \hbar/\tau_{\mathrm{THz}}$ obtained from the experiment (points). The red line is a fit using $\Gamma \propto \sqrt{B}$ (see text).

4.5 Transport characterisation

Transitions between LLs are characterised by different lifetimes due to the partial occupation of initial and final states (Section 2.6.1). This was confirmed from the Gabor-Morlet transform, as well as from the fits in the time- and frequency-domain in Section 4.2. For this reason, and since the LL width Γ is thought to be independent of LL index [69], the average value of τ_i (τ_{THz}) was considered at every B. This decreases monotonically from around 5 ps at $B = 1.0\,\mathrm{T}$ to 2 ps above $B = 5\,\mathrm{T}$. As previously reported [104], values of τ_{THz} are slightly larger than the single-particle (quantum) lifetimes τ_{q} obtained by analysing the Shubnikov-de Haas oscillations [75] (see Table 4.5). The physical meaning of quantum lifetime was introduced in Section 2.5.2. For the SiGe2 sample, the SdH oscillations revealed carriers with different τ_q.

The obtained τ_{THz} were used to estimate the B-dependence of the LLs width given by $\Gamma(B) = \hbar/\tau_{\mathrm{THz}}(B)$. These are reported in Figure 4.11(a,b) for SiGe1 and SiGe2, respectively. The error bars were obtained by varying the fits (to time-domain data for $B \leq 5\,\mathrm{T}$, and frequency-domain data at higher B) until χ^2 increased by 20 %.

The experimental CR linewidth is consistent with $\Gamma \propto \sqrt{B}$, as indicated by the dashed lines in Figure 4.11(e,f). For short-range scattering potentials $\Gamma = \sqrt{2\hbar^2 eB/\pi m_b^* \tau_{\mathrm{t}}}$, where τ_{t} is the $B = 0$ transport relaxation time [69], see Section 2.5.1. Using the experimental Γ the zero-field lifetimes were found to be $\tau_{\mathrm{t}} = 31 \pm 1$ ps

Sample	τ_{THz} (ps)	τ_{q} (ps)	τ_{t} (ps)	τ_{MT} (ps)	$\mu_{\mathrm{H}}(10^5\,\mathrm{cm}^2\,/\mathrm{Vs})$
SiGe1	5.1-1.8	0.5	31 ± 1	24	4.5
SiGe2	5.1-2.0	$1.6, 1.4, 0.87$	33 ± 3	29	7.8

Table 4.5: Average value of τ_i obtained from the time- and frequency-domain fits (τ_{THz}) in the magnetic field range 1.0-7.5 T. Quantum lifetime from magnetotransport measurements (τ_{q}) [75]. Transport lifetime obtained from THz-TDS (τ_{t}) and from magnetotransport measurements (τ_{MT}). Hall mobility (μ_{H}) [75].

and 33 ± 3 ps for SiGe1 and SiGe2, respectively, and in line with τ_{MT} obtained from the dc Hall mobility [75] and reported in Table 4.5. Interface roughness scattering, remote and background ionized impurity scattering are also thought to contribute to the mobility of Ge-QWs [105]. The transport lifetimes τ_{MT} and τ_{t} are substantially greater than τ_{q} (Table 4.5). Both remote ionized impurity scattering and interface roughness scattering can result in $\tau_{\mathrm{MT}} > \tau_{\mathrm{q}}$ [106]. Furthermore, CR lifetime broadenings of the order of 0.3 meV (as reported herein) and with the same $\Gamma \propto \sqrt{B}$ dependence can also arise from hole-acoustic phonon scattering mediated by the deformation potential [107, 108, 109].

4.6 Spin-relaxation time

In Section 4.2.1 it has been shown that time-slices of the Gabor-Morlet amplitude at the resonance frequencies reveal pronounced coherent beats that persist over the experimental time window. This provides direct evidence that the up and down spin populations remain phase-coherent over this time scale, with a spin-dephasing time $\tau_s > 10$ ps. Both the Elliot-Yafet (EY) and the Dyakonov-Perel (DP) spin-dephasing mechanisms - briefly introduced in Section 2.4 - may contribute in sGe-QWs [28, 53]. Momentum scattering destroys spin coherence in the EY process, which predicts $\tau_s \propto \tau_t/(g^* - g_0)^2$, where g^* is the effective hole g-factor, $g_0 = 2.022$, and τ_t is the momentum scattering time [28]. The DP mechanism is also active in systems without inversion symmetry [53].

Weak antilocalization results reported $\tau_s \sim 16$ ps when the Rashba splitting energy $\Delta = 0.30$ meV and $\tau_t = 0.16$ ps, and identified the DP process as dominant [59]. Scaling this value of τ_s according to the DP process ($\tau_s \propto 1/\tau_t$) predicts that $\tau_s < 0.2$ ps for the values of τ_t determined for SiGe1 and SiGe2. However, this short τ_s is not consistent with our observation of quantum beats between spin-up and spin-down CRs, which show that $\tau_s > 10$ ps. The DP mechanism, which is significant only in the case of strong momentum scattering [53], therefore does not dominate in our samples. In bulk Ge, where the EY mechanism dominates, hole dephasing times are $\sim 150\,\mathrm{ps}$ at around $6\,\mathrm{K}$ [32].

4.7 Summary

In conclusion, narrow cyclotron resonances of spin-split heavy hole states were observed in strained Ge quantum wells. The time-frequency decomposition method applied to data from THz time-domain spectroscopy permitted spin-split resonances to be identified even when their spacing in frequency was smaller than their linewidth. Spin-split sub-band densities and cyclotron energies were used to independently estimate the Rashba coefficient. Importantly, the Rashba coefficient was obtained from THz time-domain cyclotron spectroscopy in a noncontact fashion and for a sample with a parallel conduction path (SiGe2), a challenge with device magnetotransport. The Rashba splitting energy for holes in strained Ge quantum wells ($\Delta \sim 2.0\,\mathrm{meV}$) was found to be enhanced in comparison to previous reports, and approaches values found for 2DEGs in III-V semiconductors (e.g., $\Delta = 4.0\,\mathrm{meV}$ in InAs QWs [110] and $\Delta = 11.6\,\mathrm{meV}$ in GaN QWs [78]). Finally, an enhanced spin-orbit interaction and a long spin decoherence time were demonstrated concurrently with a high mobility, emphasizing the potential of strain-engineered Ge quantum wells for CMOS-compatible spintronics. The experimental approach adopted herein is highly complementary to previous magnetotransport studies of the Rashba effect in Ge quantum wells [59, 75] as it is contactless and therefore is not sensitive to device fabrication issues.

Chapter 5

OQHE in higher strain Ge-QWs

In the following chapter, experiments on spin-split heavy-hole gases within 1.3% strained Ge-QWs (samples Ge-10nm and Ge-20nm in Table 3.1) are described. The effect of the higher strain, in comparison to Chapter 4 is investigated by means of *polarization-resolved* THz-TDMS outlined in Section 3.2.3. This technique probes the parallel and perpendicular response of carriers to incident linearly-polarised THz-pulses and allows the observation of the magnetic field dependence of the complex Faraday angle, Θ_{F}. Since the complex Faraday angle is related to the transverse magnetoconductivity $\sigma_{xy}(\omega, B)$ (Hall response), polarisation resolved THz-TDMS gives the chance to investigate the presence of plateaux in σ_{xy} at integer filling factors as a consequence of the optical quantum Hall effect (OQHE), i.e. the quantum Hall effect driven by an ac electric field.

An introduction to the Faraday effect is first given in Section 5.1. This, driven by the presence of two dimensional carrier systems, results in a transmitted THz-pulse with an altered polarisation-plane and ellipticity and can be explained in terms of cyclotron active and inactive modes. The theoretical model is outlined in Section 5.1.1, where the relation between Θ_{F} and σ_{xy} is presented. The method to observe the OQHE in the THz-range, and the high mobility two-dimensional systems for which this effect has been reported, are briefly presented in Section 5.2. A comparison with 2DEGs in a GaAs/AlGaAs-QW is given in Section 5.3, this permitted heavy holes within the sGe-QWs to be uniquely identified by the opposite helicity of the transmitted THz radiation in the time domain, as well as from the opposite sign of the determined ellipticity in the frequency-domain. Effective masses are evaluated in Section 5.4 where a first estimation of the carrier densities is obtained by means of the f-sum rule applied to the experimental longitudinal conductivity σ_{xx}. In Section 5.4.1 the carrier density is alternatively evaluated, together with

CR-frequencies and lifetimes, by fitting both the time-domain waveforms and the complex Faraday angles in the frequency-domain, also allowing the determination of σ_{xy}. As presented in the case of the 0.8% sGe-QWs, the determined CR-frequencies in the examined magnetic field range are modelled by calculating the Landau level (LL) transitions, as reported in Section 5.5. This permitted the evaluation of the g-factor as well as the Rashba splitting energy, which is found to be weaker as a consequence of the enhanced strain. Strain-enhanced lifetimes with mobilities exceeding $1.5 \times 10^6\,\mathrm{cm^2V^{-1}s^{-1}}$ are reported in Section 5.6. As reported in Section 5.7, the strain-enhanced mobilities within the characterised samples allowed the first observation of the OQHE for 2D heavy holes, via distinct plateaux in σ_{xy} at even and odd filling factors. Finally, differences between the 10 and 20 nm thick sGe-QWs are discussed in Section 5.8 in the context of the joint density of states.

The results in this chapter have been published as M. Failla *et al.*, New J. Phys. **18**, 11, 113036 (2016).

5.1 The Faraday effect

In the mid-nineteenth century Michael Faraday (1791-1867) spent considerable effort to prove that light was an electromagnetic phenomenon [111]. He performed experiments to find evidence that electric and magnetic forces can affect light's polarisation. While, because of the lack of sensitive enough methods, he could not prove the electro-optic effect - discovered thirty years later by John Kerr (1824 1907) - on 1845 he observed the magneto-optical effect which has since been named the Faraday effect or Faraday rotation. The Faraday effect consists of the rotation of the polarisation-plane of linearly polarised light propagating through a medium in the parallel direction to an applied magnetic field, i.e. in the Faraday geometry [79]. The polarisation-plane is rotated by the Faraday angle:

$$\theta_F = VBd, \tag{5.1}$$

where d is the thickness of the medium, B is the applied magnetic field and V is called the Verdet constant. In the following the Faraday effect is described for a 2D conductive system.

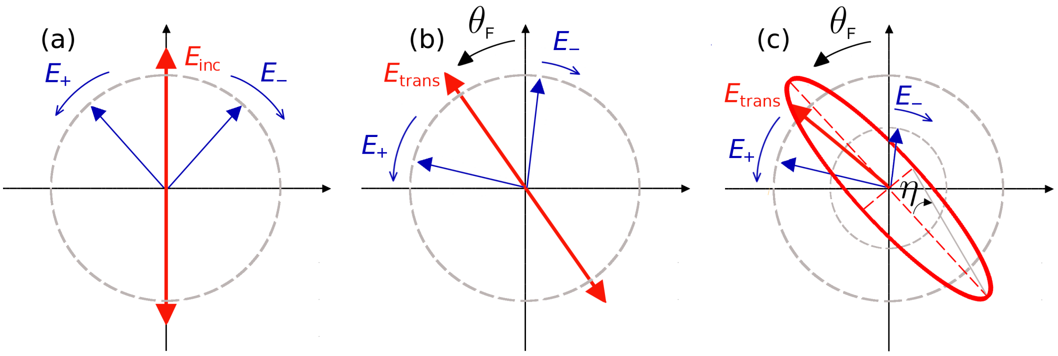

Figure 5.1: (**a**) Decomposition of a linearly polarised incident pulse, E_{inc}, in cyclotron resonance active and inactive modes, $E_\pm$. (**b**) Rotation of the polarisation-plane θ. (**c**) The Faraday effect results in a transmitted elliptically-polarised wave with θ-tilted polarisation-plane and ellipticity η, see text. Adapted from [112].

5.1.1 Cyclotron resonance active and inactive modes in the Faraday geometry

A linearly polarised wave propagating through a medium in the Faraday geometry can be decomposed into a superposition of circularly polarised waves [see Figure 5.1(a)], i.e.:

$$E_{x,y} = \sqrt{1/2}(E_+ \pm E_-), \tag{5.2}$$

and, vice-versa, by measuring E_x and E_y, the transmitted CR-modes can be obtained from:

$$E_\pm = \sqrt{1/2}(E_x \pm iE_y). \tag{5.3}$$

These waves are cyclotron resonance active (CRA) or inactive (CRI) modes, with opposite circular handedness - here ± denote right and left-handed light - which couples with the cyclotron motion of carriers within the material, see Section 2.5.

To explain how, in the Faraday effect, the presence of carriers affects the polarisation state of an incident pulse, let us consider the dielectric tensor of a material (in the Faraday geometry, Section 2.6.1) given by [112]:

$$\epsilon(\omega) = \begin{pmatrix} \epsilon_{xx}(\omega) & \epsilon_{xy}(\omega) & 0 \\ -\epsilon_{xy}(\omega) & \epsilon_{xx}(\omega) & 0 \\ 0 & 0 & \epsilon_{zz}(\omega) \end{pmatrix}.$$

The non-zero off-diagonal components, ϵ_{xy}, are induced by the magnetic field. The dielectric constants for the CRA/CRI modes is given by:

$$\epsilon_\pm(\omega) = \epsilon_{xx}(\omega) \mp i\epsilon_{xy}(\omega). \tag{5.4}$$

As already outlined in Section 3.3, this is related to the complex refractive index through:

$$\epsilon_\pm = \tilde{n}_\pm^2 = (n_\pm(\omega) + i\kappa_\pm(\omega))^2. \tag{5.5}$$

The difference between n_+ and n_- leads to different velocities and phases for the $E_\pm$ modes ($v_\pm = c/n_\pm$) and results in the θ-rotation of the plane of polarisation as depicted in Figure 5.1(b). At the same time, different absorption coefficients ($\alpha_\pm = 2\kappa_\pm\omega/c$) lead to different amplitudes. As a consequence of those differences, the transmitted wave presents an elliptical polarisation with ellipticity η, as shown in Figure 5.1(c).

Since the velocity, phase and absorption coefficients are related to complex refractive index, and therefore to the complex dielectric function, the Faraday rotation can be described as a function of the sheet conductivity σ, defined in Equations (2.66) and (2.67). Considering an ac-field $E_\pm$ and the Drude formalism as in Section 2.5, the current density produced by the CRA/CRI modes is:

$$J_\pm = \sigma_\pm E_\pm. \tag{5.6}$$

The complex conductivity $\sigma_\pm$ is related to the diagonal and off-diagonal component of the optical conductivity tensor in Equation (2.65), i.e. [113]:

$$\sigma_\pm = \sigma'_\pm + i\sigma''_\pm = \sigma_{xx} \pm i\sigma_{xy}. \tag{5.7}$$

Let us now consider a generic 2-dimensional carrier system - with sheet density N_s - sandwiched between two materials with refractive indexes n_1 and n_2. The transmission of the CR-modes depends on the complex conductivity as [114]:

$$E_\pm = \frac{2n_1}{n_1 + n_2 + \sigma_\pm/\epsilon_0 c} = |E_\pm| e^{i\xi_\pm} \tag{5.8}$$

where:

$$\xi_\pm = -\tan^{-1} \frac{\omega_{ps}(\omega \pm \omega_c)}{(\omega \pm \omega_c)^2 + (1/\tau^2 + \omega_{ps}/\tau)}, \tag{5.9}$$

with

$$\omega_{ps} = \frac{N_s e^2}{m^* \epsilon_0 c}(n_1 + n_2) \tag{5.10}$$

defined as in Ref. [115]. The incident pulse is rotated by the Faraday angle:

$$\theta_F = \frac{\xi_+ - \xi_-}{2}, \tag{5.11}$$

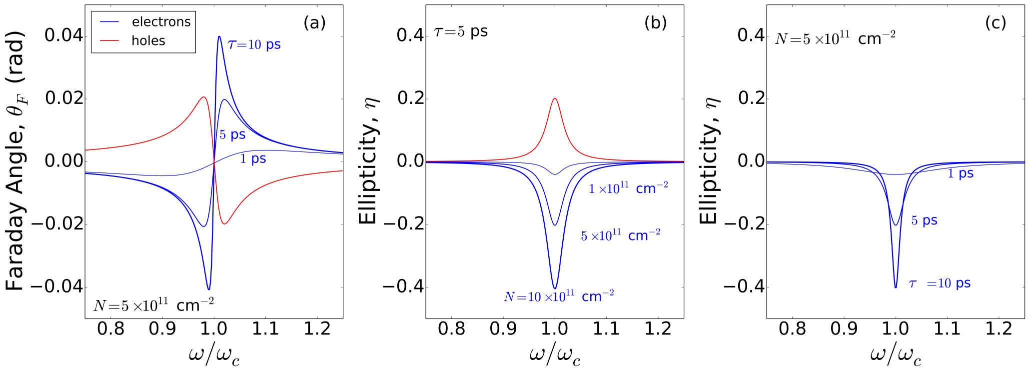

Figure 5.2: (**a**) Faraday angle θ_F, given by the real part of Equation (5.15), for electrons (blue) and holes (red). Curves have zero value at the cyclotron resonance frequency $\omega = \omega_c$. (**b**) The Lorentzian shape of the ellipticity η, given by the imaginary part of Equation (5.15), and the comparison at different carrier density N and same value of lifetime τ. (**c**) Comparison of the ellipticity with the same carrier density and different lifetimes.

and results in a transmitted elliptically-polarized pulse with ellipticity:

$$\eta = \frac{|E_+| - |E_-|}{|E_+| + |E_-|}. \tag{5.12}$$

With the assumption $\omega_{ps} \ll [(\omega \pm \omega_c)^2 + 1/\tau^2]^{1/2}$ we obtain [114, 70]:

$$\theta_F \approx \frac{\sigma''_- - \sigma''_+}{2(n_1+n_2)\epsilon_0 c} = \frac{\mathrm{Re}(\sigma_{xy})}{(n_1+n_2)\epsilon_0 c} \tag{5.13}$$

$$\eta \approx \frac{\sigma'_- - \sigma'_+}{2(n_1+n_2)\epsilon_0 c} = \frac{\mathrm{Im}(\sigma_{xy})}{(n_1+n_2)\epsilon_0 c} \tag{5.14}$$

where the last equality is obtained from Equation (5.7). The Faraday rotation spectrum can be therefore defined as:

$$\Theta_F(\omega, B) = \theta_F(\omega, B) + i\eta(\omega, B) \simeq \frac{\sigma_{xy}(\omega, B)}{(n_1+n_2)\epsilon_0 c}. \tag{5.15}$$

Equation (5.15) relates the Faraday angle and the ellipticity to σ_{xy} and, as demonstrated in Section 2.5, to the carrier density, scattering time and cyclotron frequency. Hence, the ellipticity change η corresponds to the imaginary part of σ_{xy}, while θ_F corresponds to the real part of σ_{xy}.

In Figure 5.2 examples of θ_F and η spectra for electrons (blue lines) at different values of N and τ, are calculated by means of Equation (5.15). Here σ_{xy} is given by Equation (2.65). The spectra of θ_F in Figure 5.2(a) present features around

ω_c which become sharper for higher values of τ. The Faraday angle spectrum for holes is inverted (red lines) as this results from the opposite sign of the hole effective mass [100]. The ellipticity η, shown in Figure 5.2(b), is a Lorentzian centred at ω_c with height and FWHM proportional to N_s and $1/\tau$, respectively. At a constant value of N_s, the change of η with τ, which also influences the height of the Lorentzian peak, is depicted in Figure 5.2(c).

5.2 The optical quantum Hall effect

Recent years have shown an ac analogue of the QHE (see Section 2.5.1) when a dc magnetic field B and the ac electric field of light are perpendicular: i. e. the optical quantum Hall effect (OQHE). As stated in the introduction, determining the complex Faraday angle $\Theta_{\mathrm{F}}(\omega, B)$ is crucial for studies of the OQHE, as this is related to the transverse magnetoconductivity which can be readily determined from Equation (5.15).

A numerical study of the dynamical response [116] predicted plateaux-like features in the carrier density dependence of the transverse (off-diagonal) magnetoconductivity $\sigma_{xy}(\omega, B)$ at THz frequencies, at integer values of the fill factor $\nu = hp_{\mathrm{2D}}/eB$. Based on this result, Ikebe *et al.* proposed a normalisation method to remove the frequency dependence of σ_{xy} by defining the normalised optical Hall conductivity [70]:

$$\tilde{\sigma}_{xy} = \left[\frac{e^2}{h}\frac{\omega_c^2}{(\omega + i/\tau)^2 - \omega_c^2}\right]^{-1}\sigma_{xy}. \tag{5.16}$$

By substituting σ_{xy} with the corresponding element of the Drude model conductivity tensor given in Equation (2.65), and considering $\omega_c = eB/m^*$, one obtains $\tilde{\sigma}_{xy} = hp_{\mathrm{2D}}/eB = \nu$. Thus $\tilde{\sigma}_{xy}$ represents an estimation of the filling factor, which is related to B and the carrier density p_{2D}.

Experimentally, plateaux in $\sigma_{xy}(\omega)$ or in the Faraday rotation angle have been witnessed only for electrons in GaAs heterostructures [70, 117] or for Dirac fermions in graphene [118]. As a consequence of the higher strain within the sGe-QWs studied herein, the expected high mobility for HHs would make possible the observation of the OQHE for 2DHGs. Important distinctions about these systems in comparison to previous studies are that: (i) the Rashba SOI can contribute in sGe, whereas it is negligible in the OQHE systems reported so far [70, 117, 118], (ii) the Zeeman energy $m_J g^* \mu_{\mathrm{B}} B$ is larger for heavy holes (which have magnetic quantum number $m_J = \pm 3/2$) than for electrons ($m_J = \pm 1/2$) for the same effective g-factor g^*, (iii) the strength of the Rashba energy Δ and Zeeman energy are closely linked to the strain, and (iv) the valence band structure of sGe is more strongly non-parabolic than that of the GaAs conduction band.

5.3 Ellipticity spectra from polarisation-resolved THz-TDMS

In the previous section the relationship between the CRA/CRI modes $E_{\pm}$ and the orthogonal components of a transmitted pulse $E_{x,y}$ has been shown. By means of polarization-resolved THz time-domain spectroscopy the two measured components of the transmitted THz pulse, $E_{x,y}$, are used to construct the CRA/CRI-modes, $E_{\pm}$, using Equation (5.3). This was performed by generating linearly polarised THz pulses using an interdigitated GaAs emitter photoexcited by femtosecond pulses from a Ti:sapphire laser oscillator. A wire grid polariser was placed after the THz emitter. THz pulses were focused on samples placed in a superconducting magnet in the Faraday geometry, where $B = 0.0 - 7.5\,\mathrm{T}$ was applied along the growth axis in $0.1\,\mathrm{T}$ steps, and at $T = 3\,\mathrm{K}$. To investigate the longitudinal and transverse response of HHs to an ac electric field, the orthogonal components of the THz radiation were probed using electro-optic sampling with a <111>-oriented ZnTe crystal [88, 119]. Details of the experimental setup are outlined in Section 3.2.3. This directly yields the complex transverse conductivity $\sigma_{xy}(\omega, B)$ (Hall response) and longitudinal conductivity $\sigma_{xx}(\omega, B)$.

In the following, samples are labeled as Ge-10nm and Ge-20nm, in accordance with the thickness of each Ge-QW. These are compared to a GaAs/AlGaAs sample (4×30 nm QWs). Details of samples are given in Section 3.4 and Table 3.1. In Figure 5.3(a) the x- and y-components ($E_x \gg E_y$) of the transmitted THz pulse through the GaAs/AlGaAs sample at $B = 0\,\mathrm{T}$ are shown in the time domain. The CR response can be resolved in the time domain by subtracting the transmitted THz electric field at $B = 0\,\mathrm{T}$ from that at finite B, i.e. $E^{\mathrm{CR}}_{x,y}(B, t) = E_{x,y}(B, t) - E_{x,y}(0, t)$. Examples of the CR response for the GaAs/AlGaAs and the Ge-20nm samples are given in Figure 5.3(b,c). Beating effects are clearly visible in E^{CR}_x and E^{CR}_y due to multiple transitions with different frequencies, as outlined in Section 4.2.

In contrast to the characterisation reported in Chapter 4, which just examined E^{CR}_x, the additional knowledge of E^{CR}_y allows the definitive identification of the type of quasiparticle undergoing CR. The total CR-waveforms $\mathbf{E}^{\mathrm{CR}}(t) = E^{\mathrm{CR}}_x \widehat{x} + E^{\mathrm{CR}}_y \widehat{y}$, shown as multicoloured lines in Figure 5.3(b,c), are elliptically polarised with opposite helicity (arrows) for the 2DEG and the 2DHG. This is because the CRA modes for electrons are CRI for holes, as a consequence of the opposite

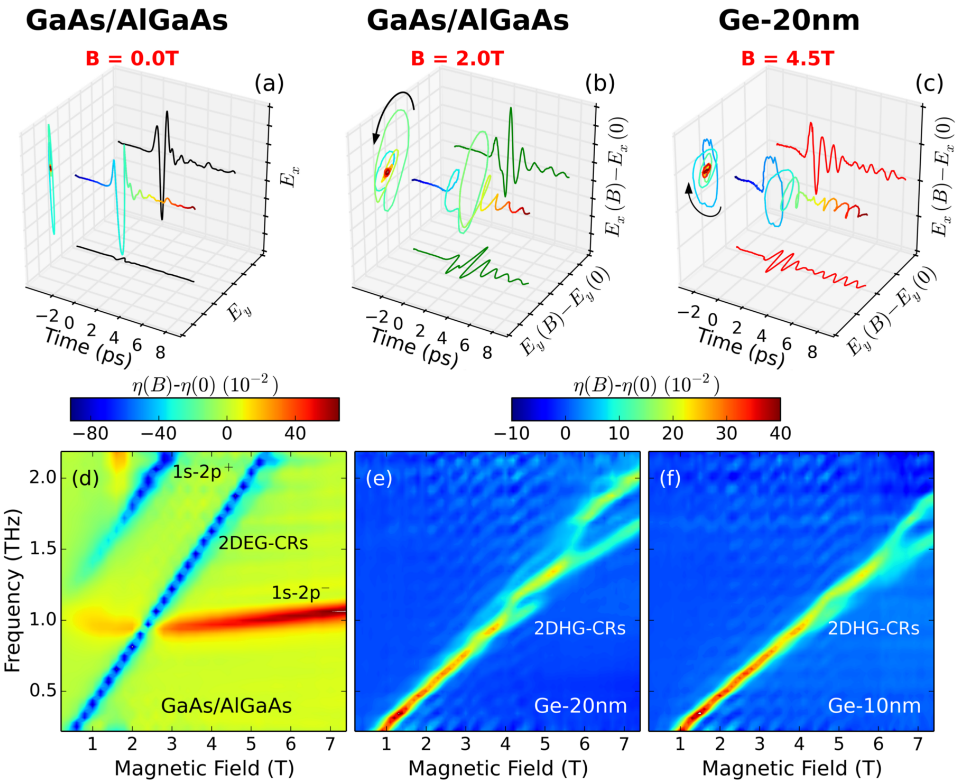

Figure 5.3: (**a**) Orthogonal components E_x, E_y of the transmitted THz pulse through the GaAs/AlGaAs sample (black lines), and the total waveform (multicoloured lines), at $B = 0\,\mathrm{T}$. (**b,c**) CR waveforms of the GaAs/AlGaAs and the Ge-20 nm samples, respectively, showing different helicity (arrows). (**d,e,f**) Ellipticity $\Delta\eta \propto \mathrm{Im}(\sigma_{xy})$ for the three samples showing different transitions. Split-CRs are resolved for the Ge-20 nm and Ge-10 nm samples.

sense of cyclotron rotation due to the opposite sign in the effective mass [100].

The time-domain data were Fourier transformed, and then converted to a circular basis set using Equation (5.3). The Faraday angle is then obtained from Equation (5.11), while the ellipticity is obtained from Equation (5.12). To rule out any contribution to θ_F and η at $B = 0\,\mathrm{T}$ due to the small but finite ellipticity of the incident pulse [see Figure 5.3(a)], $\Delta\theta_\mathrm{F} = \theta_\mathrm{F}(B) - \theta_\mathrm{F}(B = 0)$ and $\Delta\eta = \eta(B) - \eta(B = 0)$ have been considered. In Figure 5.3(d,e,f) the ellipticity change $\Delta\eta$ is shown for all samples in the magnetic field range 0-7.4 T. For the GaAs sample [Figure 5.3(e)] the resonance with frequency proportional to B and $\Delta\eta < 0$ is ascribed to the CR of the 2DEG. The blue branch (above 1 THz frequency) corresponds to hydrogenic 1s-2p$^+$ transitions of donor-bound electrons in the n-type substrate, while the red region results from hydrogenic 1s-2p$^-$ transitions [120]. These contributions have opposite ellipticity because the B-field lifts the degeneracy of the 2p excited states for donor-bound electrons in the substrate. In Figure 5.3(f,g), the positive $\Delta\eta$ is assigned to the CRs of the 2DHG within the Ge quantum well. The opposite sign with respect to that for the GaAs 2DEG shows that holes are the dominant charge carrier in the sGe-QWs. As outlined in Section 2.3.2, and reported in Chapter 4, the HH valence band of strained Ge is nonparabolic, and the Zeeman effect results in spin-split CRs at high B, while at all B the Rashba interaction can split spin-up to spin-up and spin-down to spin-down CR energies [46, 58].

5.4 Sheet density and effective mass

In order to know the magnetic field at which to expect quantum Hall plateaux the carrier density p_{2D} of the 2DHG was found accurately.

Firstly, the experimental longitudinal conductivity $\sigma_{xx} = \sigma'_{xx} + i\sigma''_{xx}$ was obtained from the transmission $T_{xx}(B,\omega) = E_{xx}(B,\omega)/E_{xx}(0,\omega)$ using [121]:

$$\sigma_{xx} = \frac{2n}{Z_0}\left(\frac{1}{T_{xx}} - 1\right), \tag{5.17}$$

where E_{xx} is the transmitted THz field along x for an incident pulse along x. Equation (5.17) is a generalisation of Equation (3.16) for a high conductive thin film sandwiched between a material with refractive index n. This approximation allowed the determination of the sheet density by using the experimental σ_{xx} and the sum rule [122]:

$$p_{\mathrm{2D}}^{\mathrm{sum}} = \frac{2m^*_{\mathrm{THz}}}{\pi e^2}\int_{f_1}^{f_2} \sigma'_{xx}(\omega)d\omega. \tag{5.18}$$

Here, m^*_{THz} is an estimate of the effective mass given by a linear fit to the CR frequencies for $B \leq 3\,\mathrm{T}$ (as in the previous chapter, see Figure 4.8). The effective mass of $0.069\,m_e$ for the the GaAs/AlGaAs sample is identical to that obtained by magneto-transport measurements [123]. In Equation (5.18), the frequency interval (f_1, f_2) can be varied to match a particular transition, for instance as required to isolate the 2DEG response of the GaAs/AlGaAs sample from the hydrogenic transitions in the substrate. To check the reliability of the estimated densities, the average value $p_{\mathrm{2D,GaAs/AlGaAs}}^{\mathrm{sum}} = 4.4 \times 10^{11}\ \mathrm{cm}^{-2}$, obtained for the GaAs/AlGaAs sample for $B \leq 3\,\mathrm{T}$ and by considering $n = 3.6$ [70], is in good agreement with the sheet density from magneto-transport measurements [123] by considering the contribution of four QWs, i.e. $p_{\mathrm{2D,GaAs/AlGaAs}}^{\mathrm{MT}} = 4 \times p_{\mathrm{2D,GaAs/AlGaAs}}^{\mathrm{sum}} \sim 18 \times 10^{11}\ \mathrm{cm}^{-2}$, validating this procedure.

Hole sheet densities within the Ge-QWs were averaged for data in the mag-

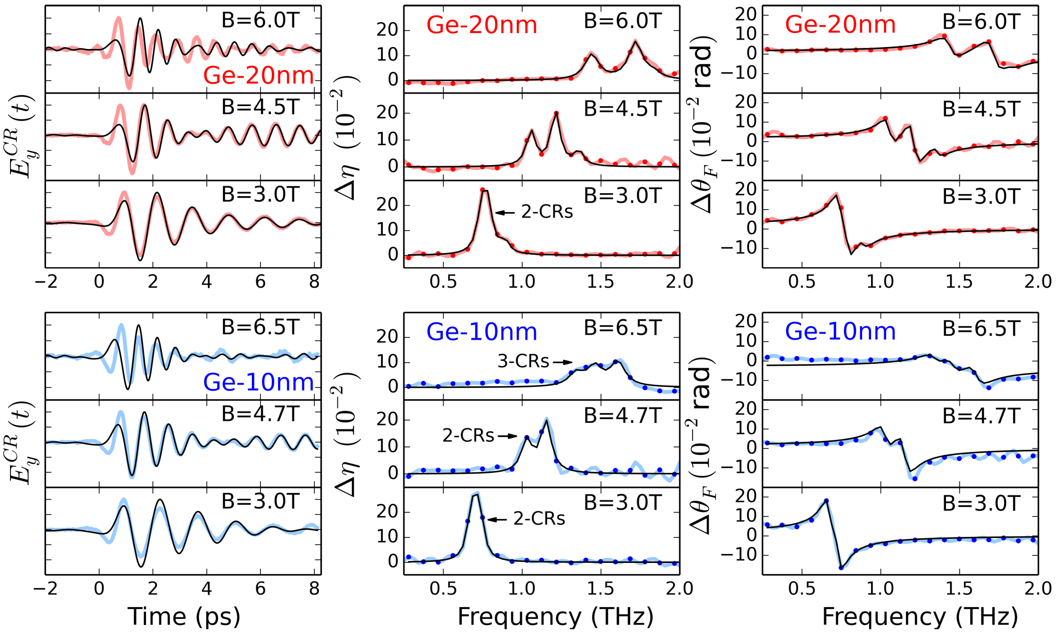

Figure 5.4: CR waveforms in time domain, $E_y^{\mathrm{CR}}(t)$, ellipticity $\Delta\eta$ and Faraday angle $\Delta\theta$ in the frequency domain for the Ge-10nm and Ge-20nm samples. Points and coloured lines are experimental data, non-padded and padded, respectively (see Section 3.3). Black lines are fits that allow $\sigma_{xy}(\omega, B)$, the transverse (or Hall) conductivity, to be determined.

netic field range without well resolved split-CRs ($B \leq 3.5\,\mathrm{T}$). The obtained values (with using $n_{\mathrm{SiGe}} = 3.8$ [124]), are $p_{\mathrm{2D}}^{\mathrm{sum}} = 13.0 \pm 0.2 \times 10^{11}$ cm^{-2} and $12.5 \pm 0.2 \times 10^{11}$ cm^{-2} for the Ge-10nm and Ge-20nm, respectively. In the same magnetic field range, linear fits of the CR frequencies result in $0.120 \pm 0.001 m_0$ and $0.110 \pm 0.001 m_0$.

5.4.1 Fit of the complex Faraday spectra

The sheet density can be alternatively evaluated, together with the CR-frequencies and lifetimes, by fitting $\Delta\theta_{\mathrm{F}}$ and $\Delta\eta$, which are linked to the real and imaginary parts of $\sigma_{xy}(\omega)$ [114, 70], as in Equation 5.15. Here, the Drude-Lorentz transverse magnetoconductivity was assumed [125] and given by [see Equation (2.65)]:

$$\sigma_{xy}(\omega) = \sum_i A_i \frac{\omega_{c,i}}{(\omega + i/\tau_i)^2 - \omega_{c,i}^2}, \tag{5.19}$$

where the $\sum_i$ considers different CR-transitions having angular frequencies $\omega_{c,i}$ and lifetime τ_i. The i-th amplitude is given by $A_i = p_{\mathrm{2D},i} e^2 / m_i^*$, where e is the carrier charge, m_i^* the cyclotron mass (from $m_i^* = eB/\omega_{c,i}$) and $p_{\mathrm{2D},i}$ is the sheet density involved in the i-th CR. As in the sGe-QWs characterisation presented in Chapter 4, with respective fitting methods outlined in Section 4.2.2, parameters from frequency-

Sample	$p_{\mathrm{2D}}^{\mathrm{sum}}$ ($\times 10^{11}\,\mathrm{cm}^{-2}$)	$p_{\mathrm{2D}}^{\mathrm{THz}}$ ($\times 10^{11}\,\mathrm{cm}^{-2}$)	$p_{\mathrm{2D}}^{\mathrm{Hall}}$ ($\times 10^{11}\,\mathrm{cm}^{-2}$)
Ge-10nm	13.0 ± 0.2	13.3 ± 0.5	13.5 ± 0.4
Ge-20nm	12.5 ± 0.2	12.3 ± 0.3	13.1 ± 0.4

Table 5.1: Sheet carrier density evaluated from: Equation (5.18)($p_{\mathrm{2D}}^{\mathrm{sum}}$); fits of time and frequency domain data ($p_{\mathrm{2D}}^{\mathrm{THz}}$); classical Hall conductivity ($p_{\mathrm{2D}}^{\mathrm{Hall}}$) in Section 5.7.

domain fits were validated by time-domain fits [98], which can for instance give more accurate lifetimes if experimental time windows are comparable to τ_i.

Fits to $\Delta\eta$ for the GaAs 2DEG's CR [Figure 5.3(d)] used $n_1 = n_2 = 3.6$ in Equation (5.15). An electron density of $p_{\mathrm{2D}} = 4.5 \times 10^{-11}\,\mathrm{cm}^{-2}$ per quantum well was found, in good accord with the sum-rule result in the previous section. In Figure 5.4, the experimental CRs in the time domain for the sGe-QWs, together with $\Delta\eta$ and $\Delta\theta_{\mathrm{F}}$ (coloured lines) and fits (black lines) using $n_1 = n_2 = n_{\mathrm{SiGe}} = 3.8$ [124], are shown at various B. The total sheet density for the Ge samples, $p_{\mathrm{2D}}^{\mathrm{THz}}$, averaged in the magnetic field range $1.5 \leq B \leq 3.5\,\mathrm{T}$, is in line with $p_{\mathrm{2D}}^{\mathrm{sum}}$, as reported in Table 5.1.

A different evolution of the CRs with B is observable by comparing the Ge-20nm and Ge-10nm samples. At $B = 3.0\,\mathrm{T}$ the ellipticity $\Delta\eta$ of the 20 nm well displays a prominent shoulder at high frequency. This appears for $B > 2.0\,\mathrm{T}$ and is still present at 4.5 T where $\Delta\eta$ consists of three resonances. On the other hand, the Ge-10nm sample exhibits a transition from one to two clearly resolved CRs at 4.7 T evolving into three CRs for $B \geq 6.4\,\mathrm{T}$. As the hole masses and densities are similar, this implies that another material parameter differs between samples. The following examines whether the Zeeman or the Rashba energies drive these differences.

5.5 Zeeman and Rashba energies

To investigate further, the CR-energies from fits are reported as black circles in Figure 5.5(a,b). Landau fans, reported in Figure 5.5(c,d) for spin up (blue lines) and spin down levels (red), were calculated in order to model the experimental CR energies, using the approach detailed in Section 4.4 and already used in the sGe-QWs characterisation in Chapter 4. As outlined earlier, this includes the influence of the Rashba effect, through the splitting energy Δ, and the Zeeman effect (proportional to the g-factor). The energy dependence of the effective mass and g-factor due to nonparabolicity was considered using Equation (4.24) and (4.23) [102], respectively. The chemical potential μ_{F} [black lines in Figure 5.5(c,d)] jumps between different

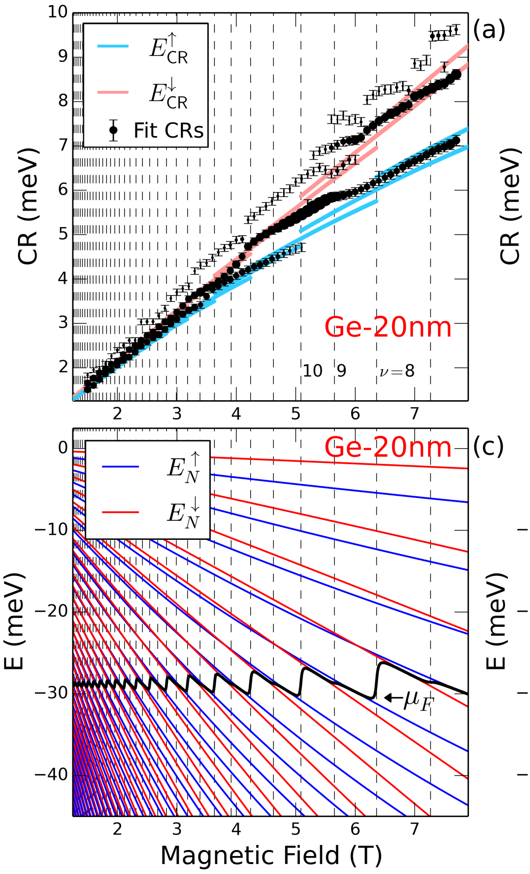

Figure 5.5: (**a,b**) Calculated spin down-down (red lines) and up-up (blue lines) transition energies compared with experiment (solid black circles). The relative size of the black circles is proportional to the estimated carrier density of the i-th CR while the error bar depicts the linewidth of the resonance. The magnetic fields at which ν is an integer are depicted as black dashed vertical lines. (**c,d**) Calculated spin down (red lines) and spin up (blue lines) LL energies.

LL energies E_N when ν is an integer, at values of B (vertical dashed lines) obtained considering $B = hp_{2\mathrm{D}}/e\nu$ with $p_{2\mathrm{D}} = p_{2\mathrm{D}}^{\mathrm{THz}}$ in Table 5.1. CRs appear and disappear at integer fill factor ν, owing to the evolution of the LL occupancy.

The energy of the strongest transitions in the experiment (big black circles) are in agreement with the spin-down-down ($E_{\mathrm{CR}}^{\downarrow}$, red lines) and spin-up-up ($E_{\mathrm{CR}}^{\uparrow}$, blue lines) transition energies between spin-split LLs. As in Section 4.4, two $E_{\mathrm{CR}}^{\downarrow}$ and two $E_{\mathrm{CR}}^{\uparrow}$ are considered as a consequence of transitions considered between δ-function LLs (width $\Gamma = 0$). The model will also underestimate the CR energy when the uppermost LL is more than half occupied as it does not include the joint density of states (JDOS). The LLs broadening and JDOS are investigated later in

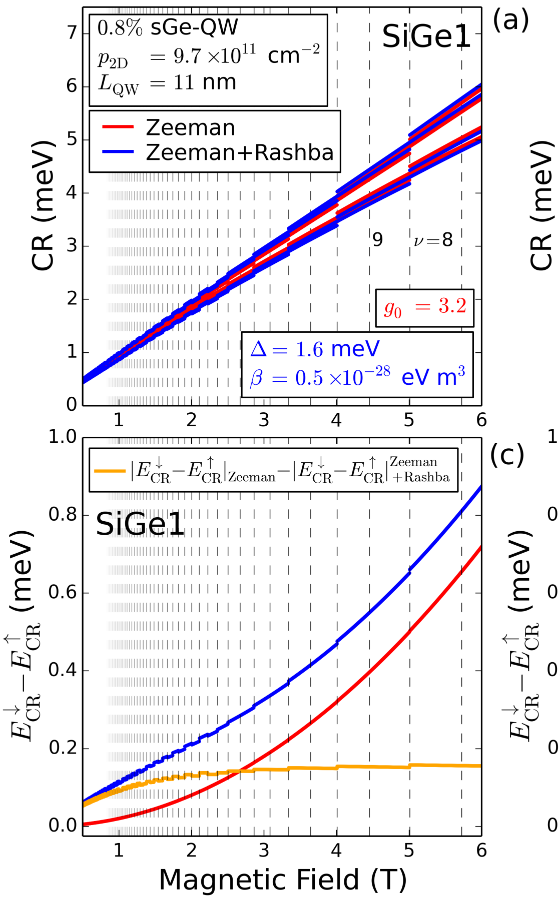

Figure 5.6: (**a,b**) CR-energies calculated by considering the effect of the bare Zeeman effect (red lines) and considering the addition of the Rashba splitting energy Δ (blue lines) for sample SiGe1 (Chapter 4) and Ge-20nm, respectively. (**c,d**) CR-splitting ($E_{\text{CR}}^{\downarrow} - E_{\text{CR}}^{\uparrow}$) for the LLs in (**a**) and (**b**) respectively. The yellow line is the difference between the red and the blue lines.

Section 5.8.

The best agreement of the model with the experimental CRs energies was obtained with $\Delta = 0.4 \pm 0.2$ meV and $m_b^* = 0.091 \pm 0.001 m_0$ for both samples. In Chapter 4, it has been found $\Delta \simeq 2.0$ meV and $m_b^* = 0.103\, m_0$ for a Ge-QW with 0.8% strain (SiGe1 sample) and a similar sheet density (9.7×10^{11} cm^{-2}). As already mentioned on page 87, since the strain increases $E_{\text{HH,LH}}$ [50] (where $E_{\text{HH,LH}}$ is the HH-LH band energy difference at the Γ point) and being $\Delta \propto 1/(E_{\text{HH,LH}})^2$ [59], the lower values reported in the current characterisation (1.3% sGe-QWs) - as well as values from Moriya *et al.* for a 2.1% sGe-QW [59] - agree with the expectation that Δ decreases with strain.

The modelled *g*-factors were $g_0^* = 2.8 \pm 0.5$ and 5.0 ± 0.5 for the Ge-10nm

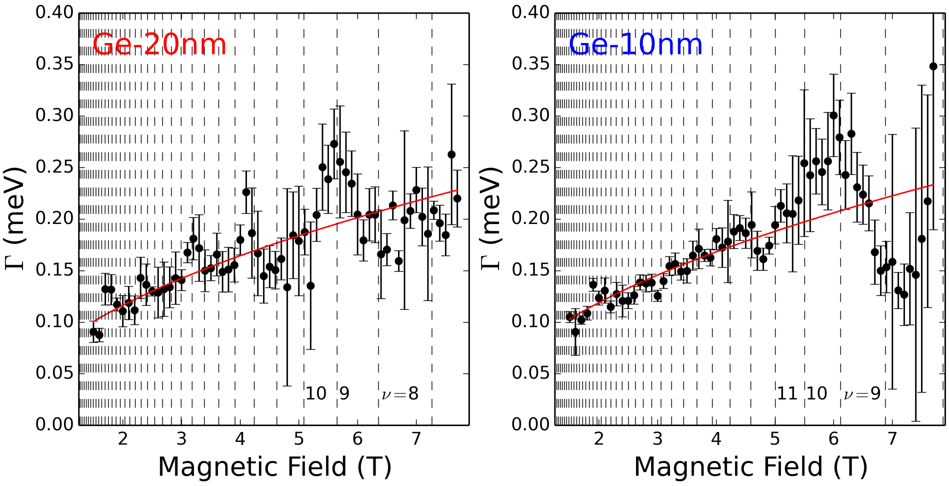

Figure 5.7: The linewidth $\Gamma(B)$ from the experiment (points) can be fitted in order to extract the transport lifetime τ_{tr} using $\Gamma = \sqrt{2\hbar^2 eB/\pi m_b^* \tau_{\mathrm{tr}}}$ (red line).

and Ge-20nm samples, respectively, with a nonparabolicity constant $\alpha_{\mathrm{NP}} = 0.025 \pm 0.005\,\mathrm{meV}^{-1}$. As the Zeeman splitting is proportional to the g-factor, sample Ge-20nm has a larger Zeeman energy than Ge-10nm, with consequences for the OQHE plateaux reported later in the manuscript. For 0.8% strained Ge-QWs with thickness 11 nm and 22 nm in Chapter 4, $g_0 = 3.2$ and 7.0 were found, respectively.

A comparison between the evolution of CR energies for the SiGe1 (11 nm thick 0.8%-sGe-QW) and Ge-20nm samples, with (blue lines) and without the Rashba contribution (red lines), is reported in Figure 5.6(a,b). The comparison between the related CR-splitting, $E^{\downarrow}_{\mathrm{CR}} - E^{\uparrow}_{\mathrm{CR}}$, is shown in Figure 5.6(c,d). For the SiGe1 sample, the effect of the Rashba splitting ($\Delta = 1.6\,\mathrm{meV}$) clearly increases $E^{\downarrow}_{\mathrm{CR}} - E^{\uparrow}_{\mathrm{CR}}$. The small size of the Rashba energy ($\Delta = 0.4\,\mathrm{meV}$) in the present case results, as shown in Figure 5.6(d), in a small contribution to the CR splitting of $\sim 0.01\,\mathrm{meV}$.

5.6 Transport lifetime and mobility

To verify that sGe-QWs studied have sufficiently high mobility to enter the quantum Hall regime, the transport mobility was determined from the B-dependence of the CR linewidth $\Gamma = \hbar/\tau_{\mathrm{THz}}$. Here, τ_{THz} is the average of the different τ_i obtained by fitting $\Delta\eta$, $\Delta\theta_{\mathrm{F}}$ and $E^{\mathrm{CR}}_y(t)$. $\Gamma(B)$ is shown in Figure 5.7 for Ge-10 nm and Ge-20 nm. The overall magnetic field evolution of Γ is consistent with $\Gamma \propto \sqrt{B}$, as expected when the mobility is mainly affected by a short-range scattering potential

[69]. As already presented in Section 4.5, the fit of this dependence, shown as the red line, allows the extrapolation of the transport lifetime τ_{tr} and mobility. This was found to be $\tau_{\mathrm{tr}} = 75 \pm 4\,\mathrm{ps}$ and $79 \pm 3\,\mathrm{ps}$ for the Ge-10nm and Ge-20nm samples, with mobilities $\mu = e\tau_{\mathrm{tr}}/m_b^* = (1.45 \pm 0.06) \times 10^6\,\mathrm{cm}^2\mathrm{V}^{-1}\mathrm{s}^{-1}$ and $(1.52 \pm 0.08) \times 10^6\,\mathrm{cm}^2\mathrm{V}^{-1}\mathrm{s}^{-1}$ respectively.

The higher mobility for the samples presented in the previous chapter, $\mu \sim 6 \times 10^5\,\mathrm{cm}^2\mathrm{V}^{-1}\mathrm{s}^{-1}$ ($\tau_{\mathrm{tr}} \sim 30\,\mathrm{ps}$) for 0.8% strain, may be linked to the larger $E_{\mathrm{HH,LH}}$. The apparent oscillation in τ_{THz} at different filling factors may be related to the variation in LL occupancy [126, 69, 127], as the CR linewidth depends on the width of the unoccupied region of the final LL. This point is elucidated in the joint density of states description later in the chapter.

5.7 Observation of the OQHE in strained Ge-QWs

Given the high mobility and precise knowledge of the fill factor demonstrated above, the transverse magnetoconductivity was examined for signs of the optical quantum Hall effect. The approach, as outlined in Section 5.2, consists of normalising σ_{xy} with the CR response through Equation (5.16) to obtain the effective density $\tilde{\sigma}_{xy}$ [70], i.e. an estimation of the filling factor ν. This should show plateaux at integer values of ν similar to those seen in the dc quantum Hall effect. Conversely, in the classical limit (low B or high ν) a straight line is expected, as $\tilde{\sigma}_{xy} \to p_{\mathrm{2D}}h/eB$.

The evolution of $\tilde{\sigma}_{xy}$, obtained from the fits of $\sigma_{xy}(\omega, B)$, is shown in Figure 5.8 for both Ge-QWs (solid circles). The classical limit is also shown (red lines) and was obtained using the sheet densities $p_{\mathrm{2D}}^{\mathrm{Hall}} = 13.5 \pm 0.4 \times 10^{11}\,\mathrm{cm}^{-2}$ for Ge-10 nm and $13.1 \pm 0.4 \times 10^{11}\,\mathrm{cm}^{-2}$ for Ge-20 nm. As can be seen in Table 5.1, these densities are in good accord with those from the sum-rule method and from fitting $\Delta\eta$ and $\Delta\theta_{\mathrm{F}}$. In the limit of smaller ν (larger B) clear plateaux are evident in $\tilde{\sigma}_{xy}$ for both samples at even filling factors ν =10, 12 and 14. In particular, these appear wider for the Ge-20nm sample while for the Ge-10nm a clear plateau is resolved at the odd filling factor $\nu = 11$.

The observation of an OQHE plateau at odd filling factor $\nu = 11$ implies that there is substantial spin splitting: in the absence of spin splitting the spin-up and down states are degenerate and plateaux are at even ν. For instance, for a gated GaAs 2DEG the OQHE around odd values of ν was attributed to the Zeeman effect [117]. Here, the relative weakness of the Rashba spin-splitting term suggests that the Zeeman term is responsible for the plateaux at $\nu = 11$ in Ge-10 nm. The insets in Figure 5.8 show the evolution of μ_{F} and the LL energies with the filling factor

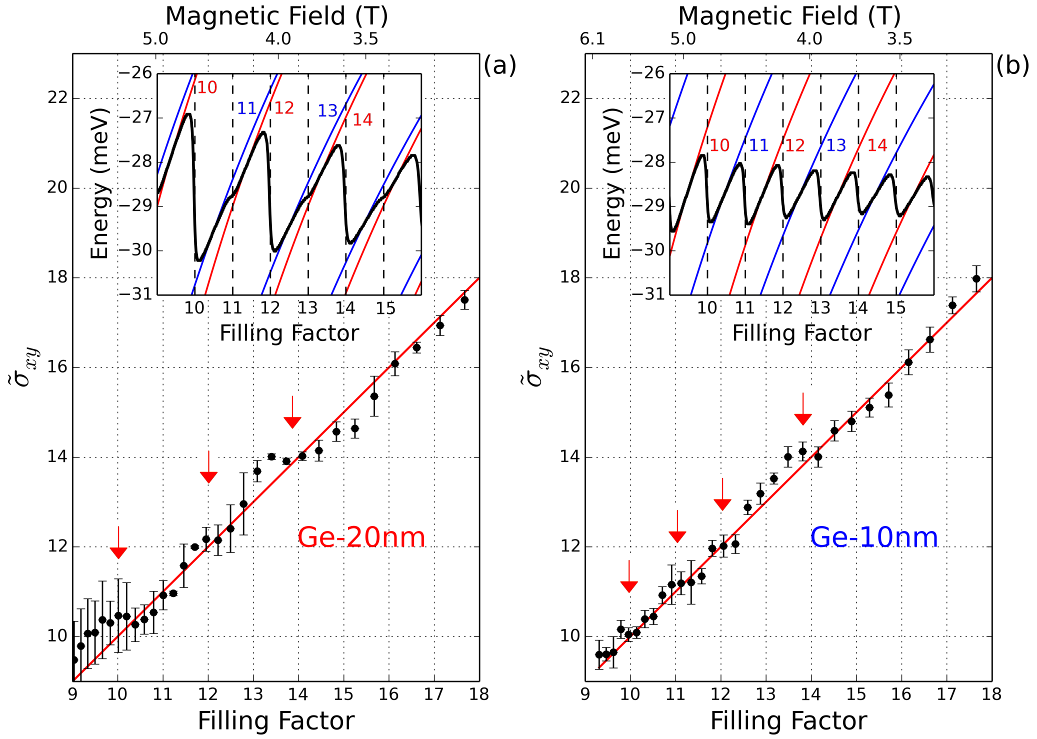

Figure 5.8: Normalized optical Hall conductivity $\tilde{\sigma}_{xy}$ as a function of filling factor and magnetic field (solid circles). Error bars are obtained by normalising fits of $\sigma_{xy}(\omega, B)$ with residual χ^2 increased by 20%. At integer filling factors $\tilde{\sigma}_{xy}$ shows evident deviations from the Drude classical limit (red lines), with plateaux around ν =10, 12, 14 (Ge-20 nm) and ν =10, 11, 12, 14 (Ge-10 nm). The insets show the evolution of the chemical potential (black line) and LLs (blue and red lines) with the filling factor.

for both samples. A plateau in σ_{xy} arises when μ_{F} lies inbetween two LLs, where changing B does not change the density of occupied states. Note that for Ge-10 nm, the LLs are well spaced in energy and ν, and hence on sweeping ν via changing B (as in the experiment) plateaux in σ_{xy} may be resolved at odd or even ν. However for Ge-20 nm the larger effective g-factor g_0^* has modified the LL dispersion, and odd and even levels are close together (within the LL linewidth, see next section). This may explain the lack of odd plateaux in the experimental result for Ge-20 nm: while there is a well defined jump in μ_F for even ν, the change is less pronounced for odd ν and the plateaux should be correspondingly weaker, or narrower in B.

The width $\Delta\nu$ of the OQHE plateaux reported in Figure 5.8 in terms of the filling factor ν is $\Delta\nu \sim 0.5$ for all the plateaux observed between $\nu = 10$ and $\nu = 14$. This is relatively large in comparison to the OQHE plateaux widths reported for high mobility 2DEGs [70, 117]. Ikebe *et al.* reported that $\Delta\nu \sim 0.05 \rightarrow 0.1$ for the THz OQHE around $\nu = 2$, while the dc Hall plateaux were broader ($\Delta\nu \sim 0.4$) [70]. Similarly, Stier *et al.* found that $\Delta\nu \sim 0.1$ for OQHE plateaux in the Faraday angle (around $\nu = 4$), with wider dc plateaux [117]. The difference between the dc and OQHE plateaux width was assigned by Ikebe *et al.* to the difference in length scales probed by dc Hall measurements and ac THz spectroscopy [70]. A number of factors may contribute to the larger $\Delta\nu$ reported here: the OQHE plateaux width depends on factors that include the distance travelled by a carrier in one oscillation period of the THz electric field, the characteristic length scale of disorder, and the LL index [70]. A comparison to the dc plateaux widths was not possible for devices made on these samples, although QHE plateaux have been seen in similar sGe-QWs [75, 128, 129].

5.8 Comparison of samples: the joint density of states

The LL-calculation adopted in this thesis - in order to model the experimental CR energies (as reported in Figure 4.10 and Figure 5.5) - considered CR transitions between δ-function LLs, that is without considering the LL's linewidth or broadening (Section 2.5.1). A more detailed calculation of the CR energies, by means of the joint density of states (JDOS), is presented in the following Section in order i) to clarify the mismatch between the experimental and modelled CRs in Figure 5.5(a) ii) to check why in the Ge-10nm samples high-energy CRs are not resolved and iii) to check if the Γ-oscillation in Figure 5.7 is related to the LL occupancy.

Joint density of states. Section 2.6.1 outlined the absorption between LLs by means of Equation (2.89). This requires explicit knowledge of the occupied and unoccupied states with wavefunctions $|o\rangle$ and $|u\rangle$, as well as the knowledge of the matrix elements $|\langle o|\boldsymbol{e}\cdot\boldsymbol{v}|u\rangle|^2$ [see Equation 2.88]. In comparison with transitions between δ-function LLs, the JDOS gives the chance to take into consideration the LL occupancy, leading to a better approximation of the absorption in Equation (2.89). The JDOS was calculated, by considering spin-conserving transitions, in the following way:

$$\begin{aligned}\mathrm{JDOS}(\hbar\omega) = &\int g(E_{\mathcal{N}}^{\uparrow\downarrow}) f(E_{\mathcal{N}}^{\uparrow\downarrow}) dE_{\mathcal{N}}^{\uparrow\downarrow} \times \\ &\qquad \int g(E_{\mathcal{N}+1}^{\uparrow\downarrow})[1 - f(E_{\mathcal{N}+1}^{\uparrow\downarrow})]\delta(E_{\mathcal{N}+1}^{\uparrow\downarrow} - E_{\mathcal{N}}^{\uparrow\downarrow} - \hbar\omega) dE_{\mathcal{N}+1}^{\uparrow\downarrow}. \quad (5.20)\end{aligned}$$

where $\hbar\omega$ is the energy of the exciting radiation, $g(E)$ is the density of states in Equation (2.85) for the i-th LL and $f(E)$ is the relative occupation which depends on the chemical potential and temperature [the Fermi-Dirac distribution in Equation (2.5)].

Γ oscillation and samples comparison. To qualitatively clarify the oscillation of Γ with B [Figure 5.7(a,b)] and the differences between the two samples, the JDOS was calculated from the LL fans in Figure 5.5(c,d). LLs with a Lorentzian shape were assumed [Equation (2.85)], with a width given by the fitted $\Gamma(B) \propto \sqrt{B}$ [red lines in Figure 5.7(a,b)]. A comparison between the DOS for the two samples at $B = 3\,\mathrm{T}$ is given in Figure 5.9(a,b). Adjacent odd and even LLs for Ge-20nm overlap and, when μ_{F} crosses two adjacent LLs, four spin-conserving CR transitions are therefore allowed [arrows in Figure 5.9(a)]. A negligible overlap results for the Ge-10nm sample in Figure 5.9(b) where, depending on the position of μ_{F}, only two or three (pictured) CRs can appear.

The shaded areas in Figure 5.9(c,d) show the JDOS contribution for each transition. The optical conductivity is proportional to the JDOS (black line), and can therefore exhibit shoulders or non-Lorentzian lineshapes as a result of partial LL occupancy. The two small contributions in Figure 5.9(c) as well as the two spin-up to spin-up transitions in Figure 5.9(d) (blue areas), differ in transition energy from the $\Gamma = 0$ case (blue and red vertical lines). The calculated JDOS in Figure 5.9(c,d) can be qualitatively compared with the experimental ellipticity reported in Figure 5.4. While two CRs are resolved in the experimental ellipticity at B=3.0T for Ge-20nm, only one is resolved for Ge-10nm, as in the JDOS model.

The overall trend at different B is depicted in Figure 5.9(e,f), which can be compared with Figure 5.5(a,b). Note that for Ge-20 nm, with larger g_0^*, the JDOS of the relatively weak, higher CR energy transitions is greater than that for Ge-10 nm, in agreement with the experiment. Finally, Figure 5.9(g,h) illustrates the mean linewidth Γ from the JDOS calculation (where each CRs contribution is weighted by its amplitude) at different B. The oscillation evident in Γ presents maxima at integer filling factor and minima at half-integer ν. The JDOS is narrowest when the uppermost LL is half-full, at half-integer ν. This gives a qualitative explanation for the oscillation in $\Gamma(B)$ from the experiment reported in Figure 5.7(a,b).

5.9 Summary

In summary, the longitudinal and transverse magnetoconductivity of strained Ge quantum wells have been characterized, in a non-contact manner, by means of po-

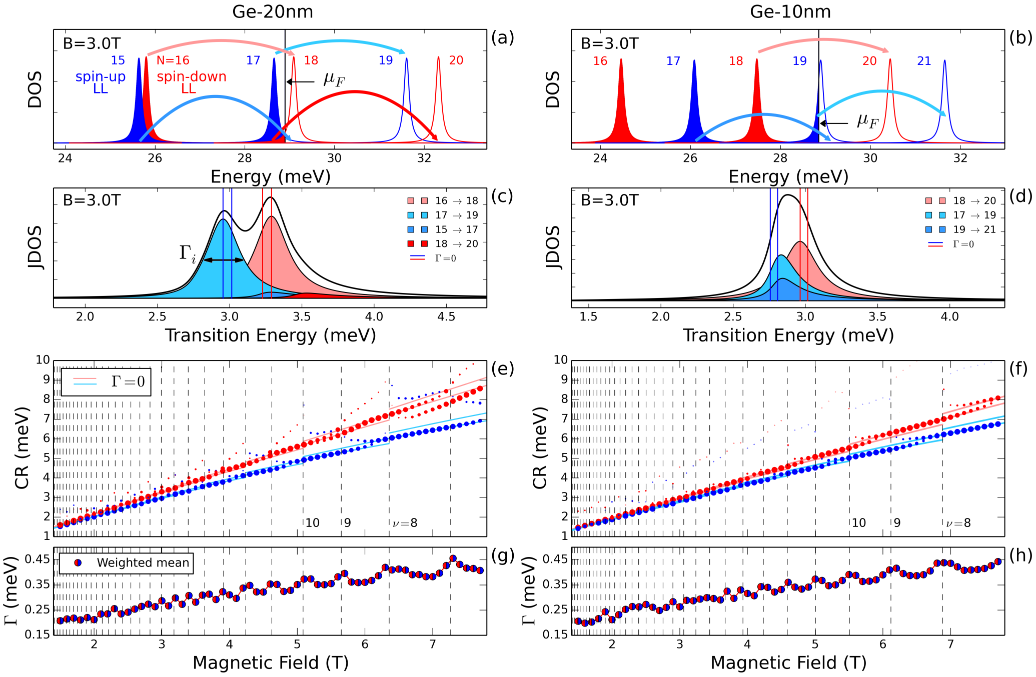

Figure 5.9: (**a,b**) Density of states (DOS) of LLs at $B = 3.0\,\mathrm{T}$ assuming a Lorentzian shape. Arrows mark spin-conserving transitions between occupied and unoccupied LLs. (**c,d**) Joint DOS at $B = 3.0\,\mathrm{T}$ for the transitions in (a) and (b). The black line shows the total JDOS, while the shaded areas denote the contributions from individual transitions with different widths Γ_i. (**e,f**) Evolution with B of the transition energies given by the maximum of the JDOS peaks. The dot size represents the amplitude of the different contributions. Red and blue lines depict the $\Gamma = 0$ transition energies. (**g,h**) Evolution with B of the mean of Γ_i, weighted by the peak intensities. Maxima appear at integer ν.

larization resolved THz-TDS. An improved mobility, but a lower spin-splitting energy, was found in comparison to Ge-QWs with lower strain analysed in Chapter 4. By determining the off-diagonal component of the conductivity tensor the optical quantum Hall effect at terahertz frequencies was observed for spin-split HHs states, apparent as plateaux-like structures in the normalized σ_{xy}. Samples with different well width resulted in qualitatively different OQHE features, as a result of the suppressed g-factor in narrow quantum wells changing the Zeeman energy.

Chapter 6

Anisotropic hole mobility in sGeQWs

In CMOS technology - apart from the chance to increase the channel mobility by strain engineering (Sections 1.2.1 and 2.1.3) or by realising QW-FETs (Section 1.1.1 and 2.2) - it is well known that device performances can be enhanced by orienting devices along a particular crystallographic direction. This is due to the anisotropic character of the mobility, as already demonstrated for Si p-type devices [130].

The mobility can change along different directions in relation to the direction-dependent band structure, and therefore to the anisotropic effective mass. For Ge-devices, as in the case of Ge on insulator (0.1% compressively strained) channels, this argument was ascribed to a ~ 5 times increase of the hole mobility along [110], in comparison with the one along [100] [131]. Since the mobility [as from Equation (2.10)] is inversely proportional to the effective mass, one would expect that such an increase can be related to a lower effective mass along [110] or to an increased lifetime. Preliminary results on Ge-QWs on $Si_{0.15}Ge_{0.85}$ buffer layers [132] - obtained by means of Hall bars [Figure 2.20(c,d)] oriented along the [110] and [100] directions - reported a 10% mobility enhancement along [110], which was assigned - as the effective mass was found to be heavier along [110] - to the anisotropic scattering mechanism rather than the direction dependence of the effective mass.

The following chapter first introduces band structure calculations for sGe-QWs in order to investigate the directional dependence of the HH-band, thus the related effective mass anisotropy (Section 6.1). As a suitable approach to investigate the anisotropic hole mobility in sGe-QWs, the alignment of a *rotatable polarisation* THz time-domain spectroscopy (RP-THz-TDS) setup is introduced in Section 6.2.

Finally, in Section 6.3, the effective mass and carrier lifetime dependence of the conductivity is described in order to predict results from RP-THz-TDS of sGe-QWs.

6.1 Anisotropic valence bands in germanium

In Figure 6.1(a-h), the energy dispersions for the valence bands in compressively strained Ge, along the [110] and [100] direction, are presented by considering different Ge content ($0.7 \leq x \leq 1.0$). Calculations are obtained by means of a $6{\times}6$ $\boldsymbol{k} \cdot \boldsymbol{p}$ method proposed by Sun *et al.* [133].

The HH-, LH- and SO-bands are presented in Figure 6.1(a,b) for the case of bulk Ge ($x = 1.0$) along [110] and [100], respectively. Since estimated densities, within sGe-QWs characterised in Chapters 4 and 5, indicated that only the HH-band is occupied, the following focuses on this particular band. For bulk Ge, this is parabolic along the [100]-direction (blue line) - as clearly noticeable from the corresponding effective mass, which is obtained by means of Equation (2.8) and reported in Figure 6.1(i) (blue line). Conversely, as evident from the related effective mass in Figure 6.1(i), the HH-band is nonparabolic along the [110] direction [red line in Figure 6.1(a)]. The difference between the effective mass along the two directions can be used to quantify the anisotropy.

Calculated energy dispersions for 10 nm (solid lines) and 20 nm (dashed lines) sGe-QWs are reported in Figure 6.1(c-h). These are obtained by considering the value for the k-vector along z which is given by the quantum confinement, i.e. $k_z = \pi/L$, where L is the QW thickness (Section 2.2.1). The model reproduces the degeneracy removal (splitting), between HH- and LH-bands at $k = 0$, due to both quantum confinement and strain. In all cases, the HH-LH splitting is larger for the 10 nm QW [see Equation (2.34)] and increases at higher strain (or less Ge content), in line with the HH-LH splitting in Figure 3.4. As in the case of bulk Ge, energy dispersions differ along the two considered directions.

Figure 6.1(j-l) shows calculated effective mass, as a function of energy, along the [110] (red lines) and [100] direction (blue lines). The energy range is chosen in order to be within the estimated Fermi energies of samples investigated in this thesis (Sections 4.4.3 and 5.5). For Ge-QWs on $\mathrm{Si}_{0.1}\mathrm{Ge}_{0.9}$ buffer layers [Figure 6.1(j)] along the [100] direction, the parabolic character of the HH band of bulk Ge is less affected in the case of 10 nm QWs (solid blue lines), while for 20 nm QWs (dashed blue lines) the effective mass presents a stronger nonparabolicity. At higher strain [Figure 6.1(k,l)], the nonparabolicity along [100] becomes less pronounced for 20 nm QWs and similar to the one of 10 nm QWs. The HH-bands along [110] present abrupt

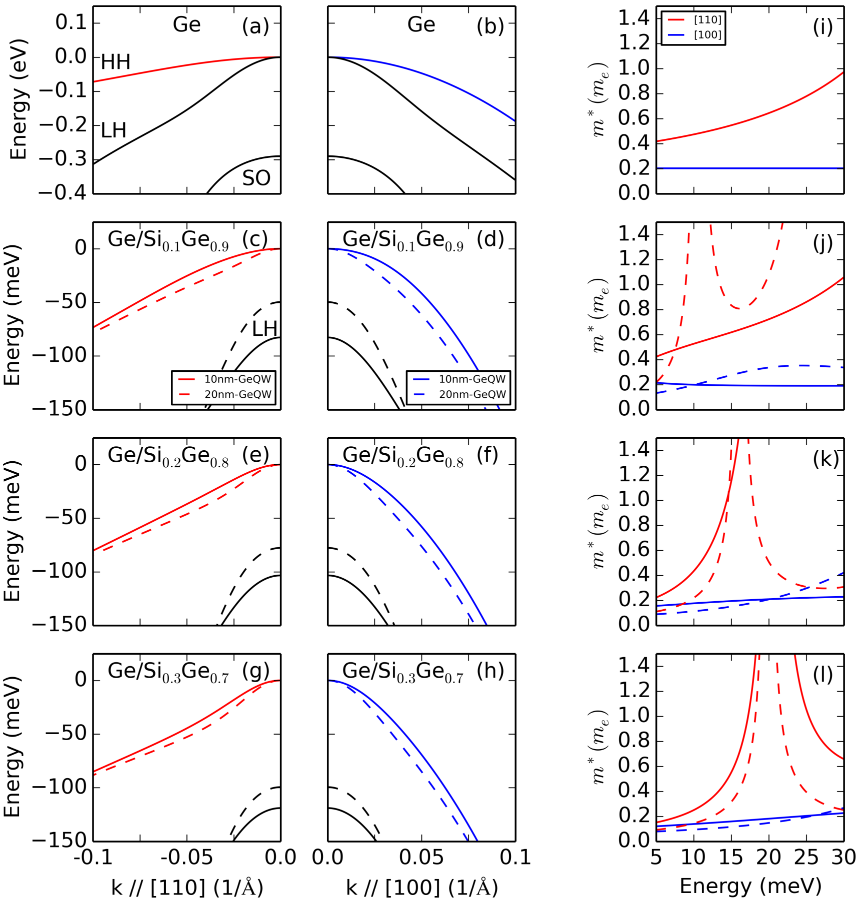

Figure 6.1: (**a-h**): Valence bands for Ge/Si$_{1-x}$Ge$_x$ QWs with different Ge content x, calculated along the [110] and [100] directions by means of a 6×6 $\boldsymbol{k}\cdot\boldsymbol{p}$ method proposed by Sun *et al.* [133]. Red and blue curves are along the [110] and [100] direction, respectively. Solid lines are for 10 nm QWs and dashed lines for 20 nm QWs. The anisotropic character of the bands is clearly noticeable. (**i,l**) Calculated effective mass for HH-bands in (**a,h**).

changes - resulting from the curvature change of the related HH-bands - therefore suggesting stronger anisotropy at particular energies and thus carrier densities.

Note that the effective mass, obtained for Ge contents $x = 0.8$ and 0.7 in Figure 6.1(k,l), differs from the experimental effective masses reported in Tables 4.3 and Section 5.5 for the investigated sGe-QWs within this thesis. This is due to the fact that, in CR experiments, the evaluated effective mass represents an average along a constant energy surface (CES) given by values of k - along the [100] and [010] - which results in the same energy $E(k_{[100]}, k_{[010]})$ (see Section 2.1.2). The CR effective mass at the Fermi energy E_F - and related Fermi wavevector k_F - can be

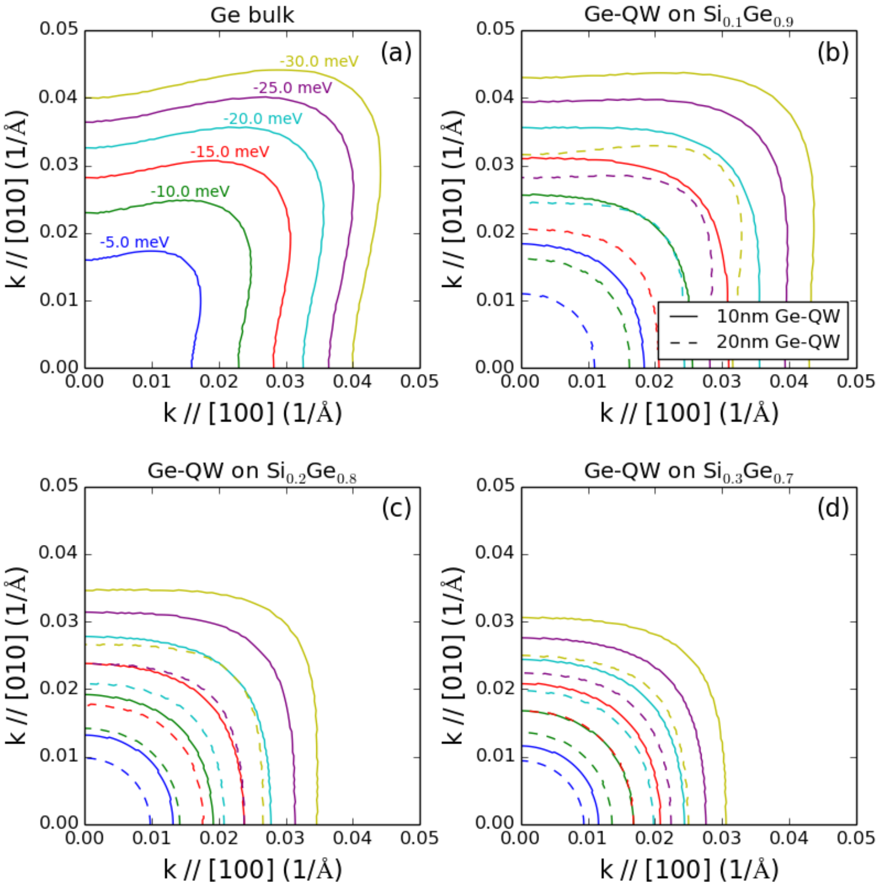

Figure 6.2: Constant energy surfaces for bands in Figure 6.1. (**a**) Bulk Ge. (**b**) sGe-QWs on $Si_{0.1}Ge_{0.9}$. (**c**) sGe-QWs on $Si_{0.2}Ge_{0.8}$. (**d**) sGe-QWs on $Si_{0.3}Ge_{0.7}$.

evaluated by means of the following expression:

$$m^*(E_\mathrm{F}, B, k_\mathrm{F}) = \frac{\hbar^2}{2\pi} \cdot \frac{\partial}{\partial E} A(E_\mathrm{F}, B, k_\mathrm{F}), \tag{6.1}$$

where B is the magnetic field and A is the area of the CES.

Constant energy surfaces. A qualitative estimation of the nonparabolicity can be obtained by plotting CESs. These, as obtained for HH-bands in Figure 6.1(a-h), are shown in Figure 6.2.

Generally speaking, an isotropic band would result in circular CESs. By observing Figure 6.2(a), clear warped surfaces are obtained for Ge bulk. The introduction of strain leads to more circular CESs, as noticeable in Figure 6.2(b) where solid lines are CESs for 10 nm QWs and dashed lines for 20 nm QWs.

The strain seems to decrease the anisotropy character of the HH-band. For instance, by comparing CESs at -30 meV (yellow lines) for different Ge content, higher strain results in more isotropic energy surfaces. In all cases, lower carrier densities - which correspond to lower energies - result in more isotropic CESs. This can be easily noticed in Figure 6.2(d) by comparing the shape of CESs at -5 meV and -30 meV. Furthermore, a comparison between CESs, at the same energy and strain for 10 nm (thick lines) and 20 nm sGe-QWs, suggests that thicker QWs, with the same carrier density, are more anisotropic.

6.2 Rotatable polarisation THz-TDS

From the band structure calculations presented in the previous section, and from the discrepant results of experiments briefly presented in the introduction of this chapter, it is clear that a systematic investigation of the anisotropic hole mobility in Ge needs to be performed, with a particular focus on the strain and QW thickness dependence.

The following, after describing the fabrication of an interdigitated photoconductive emitter (iPCE), outlines the alignment of a *rotatable polarisation* THz-TDS setup as a suitable, contactless, technique to investigate the anisotropic hole mobility in sGe-QWs in a future study. This system was designed and optimised to give linearly polarised THz pulses with an amplitude that is independent of the polarisation angle.

6.2.1 Interdigitated photoconductive THz emitter: fabrication

The interdigitated photoconductive emitter (iPCE) was realised on a semi-insulating GaAs substrate by means of photolithography, evaporation and lift-off processes. Photolithography was performed by using a AZ5214E photoresist, which gives rise to an ideal negative wall profile to facilitate the lift-off [134]. This was spin-coated on the GaAs substrate for 35 s at 4000 rpm and, afterwards, pre-baked for 2 minutes at 110° C. The bottom layout of the iPCE - Au strips in Figure 6.3(a) - was transferred from the photomask to the PR by exposing UV light with a fluence of $\sim 40\,\mathrm{mJ/cm^2}$. After a second bake at 115° C for 4 minutes, the PR was flood exposed with a UV-fluence of $\sim 250\,\mathrm{mJ/cm^2}$. The layout was successively developed by using a MF-319 developer for 45 s. By means of an electron beam evaporator, 300 nm of gold on top of 5 nm of Ti were deposited. The thin Ti layer assured a better contact with the GaAs substrate. Lift-off in acetone completed the first step.

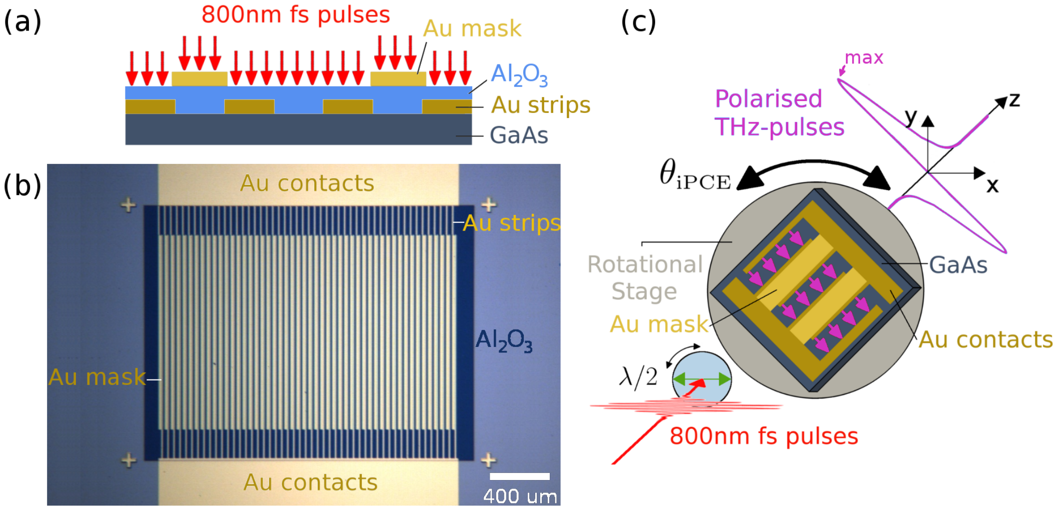

Figure 6.3: (**a**) Sketch (cross section) of the interdigitated photoconductive emitter (iPCE). (**b**) Optical microscopy (top view) of the iPCE. (**c**) Scheme of the iPCE mounted in a rotation stage allowing the polarisation of the THz-pulse to be rotated in accordance with the acceleration of the photogenerated carriers (purple arrows).

To avoid destructive interference, further Au strips were deposited, by again using the above procedure in order to cover every other gap [Au mask in Figure 6.3(a)]. Before this deposition, in order to prevent short circuiting, a 110 nm layer of insulating Al_2O_3 [blue layer in Figure 6.3(a)] was deposited to vertically separate the Au mask and strips. Such a thickness was chosen in order to maximise the transmission of the 800 nm photoexcitation beam. An optical microscopy image of the obtained device is reported in Figure 6.3(b), where Au contacts, strips and mask, as well as the Al_2O_3 layer are clearly distinguishable. The Au strips have a $5\,\mu$m width and a $5\,\mu$m spacing, resulting in a photoconductive area of $2\,\text{mm} \times 1.3\,\text{mm}$.

As described in Section 3.2.1, the photoexcitation of such a device results in the emission of linearly polarised THz pulses [see Figure 3.2(c)]. This is a consequence of the acceleration of the photogenerated carriers in the direction perpendicular to the gold strips. In Figure 6.3(c) the direction of the accelerated carriers (purple arrows) defines the polarisation of the emitted pulse (purple THz-trace). Therefore, by mounting the device on a motorised rotation stage, one can obtain a rotatable polarisation emitter whose alignment is described in the next Section.

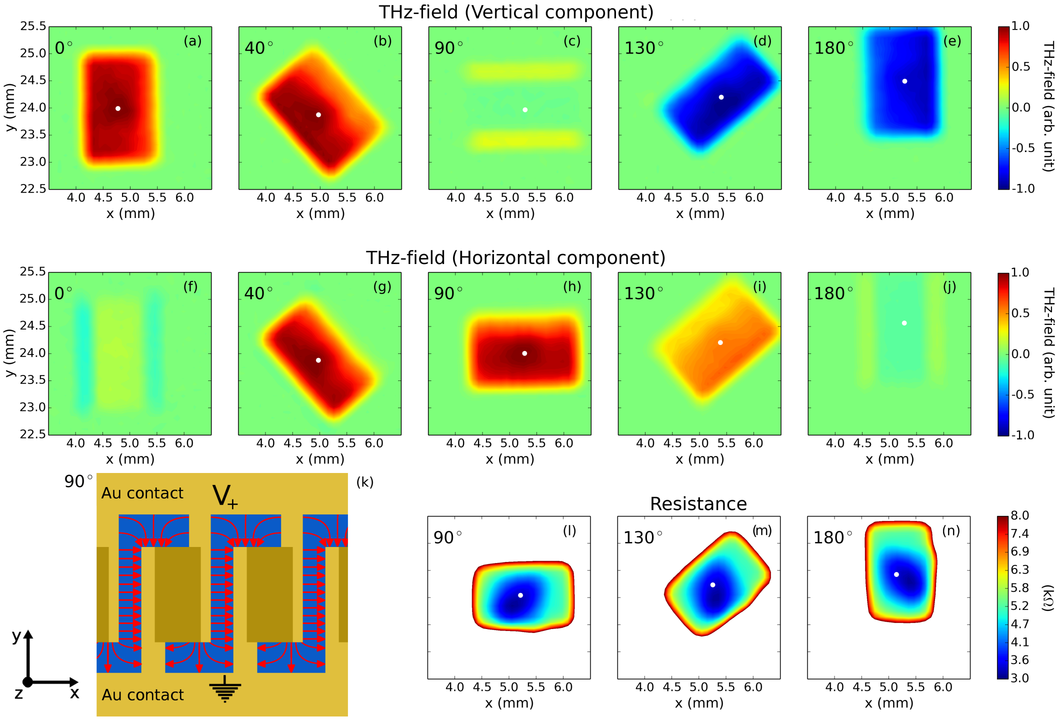

Figure 6.4: (**a-e**) Map of the vertical component of the emitted THz-pulse at different angles. (**f-j**) Horizontal component of the THz-pulse. (**k**) Scheme of the iPCE showing the direction of the accelerated carriers due to the applied voltage. (**l-n**) Resistance map.

6.2.2 Alignment

Focusing the exciting beam onto the same position of the photoconductive area of the iPCE is fundamental to obtain a constant THz emission at different emitter angles, θ_{iPCE}. Since centring the device by hand is a challenging task, the rotation stage was mounted onto two motorised linear stages, allowing movement of the emitter along the x and y directions and, therefore, focusing of the excitation beam in different parts of the device. The following presents xy-maps of the THz emission, and resistance, as obtained by moving the two motorised linear stages - therefore focusing the exciting beam on different parts of the device. Obtained maps were used to estimate the centre positions at different angles, $x_c(\theta_{\text{iPCE}}), y_c(\theta_{\text{iPCE}})$.

THz-emission maps. The iPCE was initially positioned in order to get vertically polarised emission [i.e. along the y-axis, see the cartesian axes in Figure 6.3(c)] at the angle $\theta_{\text{iPCE}} = 0°$ of the rotation stage. At different θ_{iPCE} and xy-positions, the two orthogonal components of the emitted pulse were measured - via the detection scheme outlined in Section 3.2.3 - to obtain THz-emission maps $E_{\text{THz},x}(x, y, \theta_{\text{iPCE}})$

and $E_{\mathrm{THz},y}(x, y, \theta_{\mathrm{iPCE}})$. A first time-domain scan was performed to fix the delay stage in order to measure the maximum of the THz-waveform [see *max* in Figure 6.3(c)]. By maintaining the delay stage at this position, $E_{\mathrm{THz},x}(x, y, \theta_{\mathrm{iPCE}})$ and $E_{\mathrm{THz},y}(x, y, \theta_{\mathrm{iPCE}})$ were measured for $0° \leq \theta_{\mathrm{iPCE}} \leq 180°$, with 10° steps. Maps of the two THz components are shown in Figure 6.4(a-e) and in Figure 6.4(f-j), for $\theta_{\mathrm{iPCE}} = 0°$, 40°, 90°, 130°, 180°. The photoconductive area is clearly resolved in all scans with exceptions at $\theta_{\mathrm{iPCE}} = 90°$, in Figure 6.4(c), or at $\theta_{\mathrm{iPCE}} = 0°, 180°$ in Figure 6.4(f, j). In these cases, a small signal is visible in two different areas of the emitter and ascribed to the carrier acceleration from the large Au contacts to the fingers. Figure 6.4(k) depicts the iPCE at 90°, where red arrows indicate the acceleration of carriers due to the applied voltage. At $\theta_{\mathrm{iPCE}} = 90°$, the THz emission arising from the carrier motion between the gold strips is horizontal (along the x-axis), while the two yellow areas in Figure 6.4(c) are due to the vertical motion of carriers from the Au contacts to the strips, giving rise to a vertical THz emission (along y). The same argument can be made for Figures 6.4(f, j). By still referring to Figure 6.4(k), or Figure 6.3(c), the sign change of the vertical component, from 0° to 180°, is due to the change of the motion direction of the photoexcited carriers. The appearance of a stronger emission in one side of the photoconductive area could be due to either i) a small misaligning of the gold strips with the mask lines, which could cause destructive interference, or ii) a change in the Al_2O_3 thickness, which may result in a different transmission of the exciting pulse in different parts of the photoconductive area.

Resistivity maps. A further xy-scan was obtained by measuring the resistance, as presented in Figure 6.4(l-n) for $\theta_{\mathrm{iPCE}} = 90°$, 130°, 180°. As from THz-maps, the photoconductive area is well resolved. The centre of the photoconductive area clearly presents lower resistivity than the edges. The low resistance region matches the strong emitting areas reported in Figure 6.4(a-e) and (f-j).

Centre positions. The obtained THz and resistance maps allowed us to calculate the centre position coordinates of the iPCE at different θ_{iPCE}, $[x_c(\theta_{\mathrm{iPCE}}), y_c(\theta_{\mathrm{iPCE}})]$. These are obtained by considering a *centre of mass* calculation, such that:

$$x_c(\theta_{\mathrm{iPCE}}) = \frac{1}{F(\theta_{\mathrm{iPCE}})} \sum_{ij} f(\theta_{\mathrm{iPCE}}, x_i, y_j) x_i(\theta_{\mathrm{iPCE}}) \tag{6.2}$$

$$y_c(\theta_{\mathrm{iPCE}}) = \frac{1}{F(\theta_{\mathrm{iPCE}})} \sum_{ij} f(\theta_{\mathrm{iPCE}}, x_i, y_j) y_i(\theta_{\mathrm{iPCE}}), \tag{6.3}$$

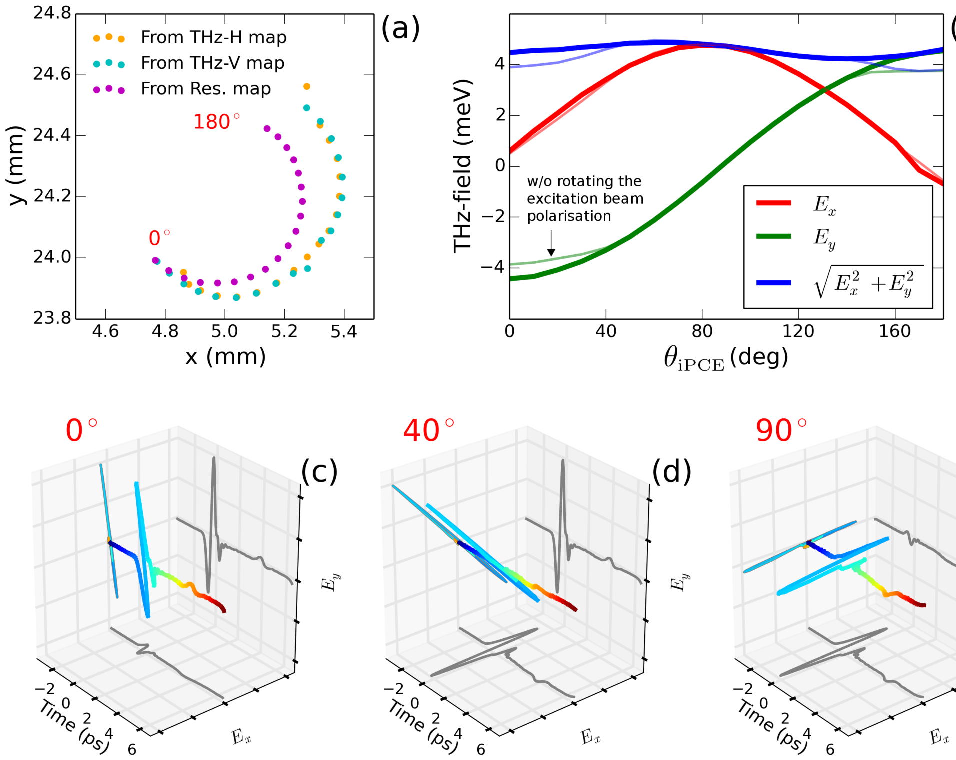

Figure 6.5: (**a**) Centre position obtained from the horizontal THz emission (orange dots), vertical THz emission (cyan) and resistance map (magenta). (**b**) Maximum amplitude of the vertical (red line) and horizontal (green) components at different emitter angles together with the total component (blue line). Thinner lines are obtained without rotating the polarisation of the exciting beam (see text). (**c,d,e**) Time-domain waveforms of the total THz pulse showing the different polarisation at $\theta_{\rm iPCE} = 0°, 40°, 90°$.

where $F(\theta_{\rm iPCE}) = \sum_{ij} f(\theta_{\rm iPCE}, x_i, y_j)$, i, j are the map coordinates and $f(\theta_{\rm iPCE}, x_i, y_j)$ can be either the measured THz-field component or the inverse of the resistance, i.e. $f(\theta_{\rm iPCE}, x_i, y_j) = 1/R(\theta_{\rm iPCE}, x_i, y_j)$. The white dots in Figure 6.4 depict the centre positions obtained from this method. All the centre coordinates from the different maps - in the considered $\theta_{\rm iPCE}$-range - are reported in Figure 6.5(a). Differently from the centre positions obtained from the resistance map (magenta dots), centre positions from the THz-maps (cyan and orange dots) deviate from a circle, due to the asymmetric distribution of the THz amplitude reported in Figures 6.4(a-e) and (f-j).

THz-emission at different angles. The orthogonal THz-components (green and red lines), as well as the THz-field amplitude, $E_{\rm THz}(\theta_{\rm iPCE}) = \sqrt{E^2_{{\rm THz},x}(\theta_{\rm iPCE}) + E^2_{{\rm THz},y}(\theta_{\rm iPCE})}$

(blue line), are reported in Figure 6.5(b) and were obtained - at different angles - by focusing the exciting beam at the centre coordinates obtained from the resistance maps. As in Figure 6.4, while the horizontal component presents a maximum close to $\theta_{\mathrm{iPCE}} = 90°$, maxima for the vertical component are at 0° and 180°. The total THz-field varies by $\sim 7\%$ across the full range of rotation, confirming the correct alignment. This is obtained by also rotating the polarisation of the exciting beam - by means of a half-wave plate [see Figure 6.3(c)] - in order to rotate its polarisation parallel to the Au strips. Note that, without this co-rotation of the exciting beam polarisation, the obtained variation along the considered θ_{iPCE}-range was $\sim 15\%$ [see the thin colored lines in Figure 6.5(b)]. Examples of time-domain waveforms (multicolored lines) - and therefore the related polarisation - are shown in Figure 6.5(c,d,e) at the emitter angles $\theta_{\mathrm{iPCE}} = 0°, 40°$ and $90°$, together with the two orthogonal components (grey lines).

6.3 Anisotropic mobility and THz-conductivity

After describing the alignment of RP-THz-TDS, the following outlines how the determined experimental conductivity would change along different directions.

The anisotropic conductivity can be simply probed by rotating the iPCE and measuring the transmission along different crystallographic directions parallel to the iPCE polarisation which is defined by θ_{iPCE}, i. e. :

$$T(\omega, \theta_{\mathrm{iPCE}}) = E(\omega, \theta_{\mathrm{iPCE}})/E_r(\omega, \theta_{\mathrm{iPCE}}). \tag{6.4}$$

Here $E(\omega, \theta_{\mathrm{iPCE}})$ is the transmitted THz pulse through the sGe-QW samples and $E_r(\omega, \theta_{\mathrm{iPCE}})$ is a reference pulse. This can be either the measured THz pulse without sample or the transmitted pulse through a reference sample (for instance the same sample with the QW removed by etching [104]). As described in Section 3.3 within the thin-film approximation, the conductivity along different directions can be directly obtained from the experimental transmission via:

$$\sigma(\omega, \theta_{\mathrm{iPCE}}) = \frac{2\tilde{n}_i}{Z_0}\left(\frac{1}{T(\omega, \theta_{\mathrm{iPCE}})} - 1\right) = \sigma_0(\theta_{\mathrm{iPCE}})\frac{1}{1 - i\omega\tau(\theta_{\mathrm{iPCE}})}, \tag{6.5}$$

where n_i is the refractive index of the SiGe layer sandwiching the QWs and Z_0 is the impedance of free space. The last equality is obtained by considering the 2D-conductivity from Equation (2.66), with $\omega_c = 0$, and by considering the θ_{iPCE}-

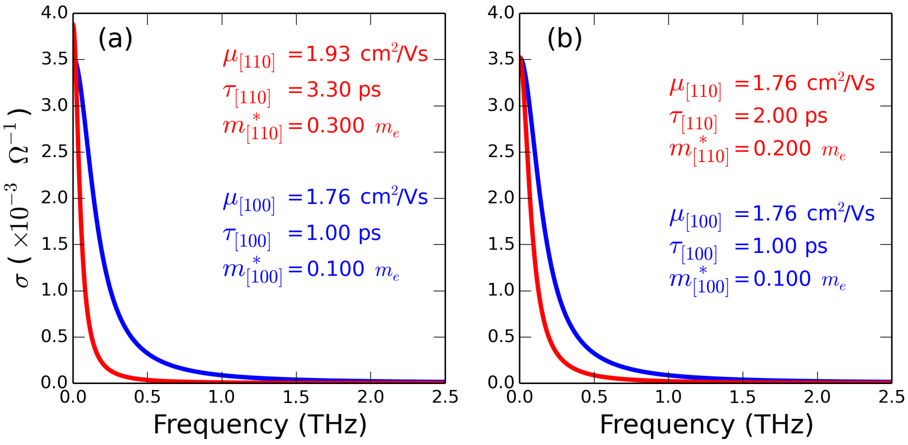

Figure 6.6: (**a**) Simulated $\sigma(\omega)$ [Equations (6.5) and (6.6)] at THz frequency along the [100] and [110] directions. These are obtained by assuming a 10% increase of μ along [110] (as reported in Ref.[132]). The difference along the two directions could be probed by means of the RP-THz-TDS outlined in Section 6.2. (**b**) Example of $\mu_{[100]} = \mu_{[110]}$ which results in a different $\sigma(\omega)$ due to different values of m^* and τ.

dependence of the DC-conductivity:

$$\sigma_0(\theta_{\text{iPCE}}) = \frac{N_s e^2 \tau(\theta_{\text{iPCE}})}{m^*(\theta_{\text{iPCE}})}. \tag{6.6}$$

Figure 6.6 shows examples of the optical THz-conductivity, as obtained from Equations (6.5) and (6.6) and by considering a carrier density $N_s = 12.5 \times 10^{11}\,\text{cm}^{-2}$ (average density from samples in Chapter 5). In detail, Figure 6.6(a) shows conductivity simulations along the [100] (red lines) and [110] direction (blue line), by assuming mobilities of $\mu_{[100]} = 1.76\,\text{cm}^2/\text{Vs}$ and $\mu_{[110]} = 1.93\,\text{cm}^2/\text{Vs}$, respectively - i.e. a 10% increase as reported in Ref. [132]. The different effective mass and lifetime (reported within the Figure) clearly results in a different frequency-dependence of $\sigma(\omega)$, therefore suggesting that RP-THz-TDS would be a suitable experiment to probe the anisotropic mobility. This method could allow - by fitting $\sigma(\omega)$ - the evaluation of effective masses and lifetimes along different directions. For instance, Figure 6.6(b) describes the case of the same mobilities along the two directions but resulting from different values of m^* and τ.

6.4 Summary

In this chapter, calculations of the band structure in sGe-QWs were presented in order to qualitatively determine the HHs effective mass along the [100] and [110] directions (Section 6.1). Results suggest that the anisotropic HH-bands can be responsible for the experimental changes of the mobility reported along different directions in sGe-QWs. The anisotropic character of the HH-bands, for different strain and QW-thickness, was qualitatively determined by calculating constant energy surfaces which showed an increased isotropy for higher strain and thicker QWs. The realisation of an iPCE (Section 6.2.1), as well as the alignment of the RP- THz-TDS system (Section 6.2.2), were introduced in order to describe a suitable experiment to probe the mobility anisotropy in sGe-QWs. Analysing the experimental transmission - thus the optical conductivity - along different crystallographic directions could clarify the interplay between the anisotropic effective mass and lifetime (Section 6.3). Moreover, such technique does not require the realisation of any device (such as Hall bars). Furthermore, since the polarisation of the THz pulse can be arbitrarily varied, RP- THz-TDS allows the estimation of the mobility, effective mass and lifetime as a function of the emitter angle, therefore more preciously than that is possible with Hall bar measurements.

Conclusions

Research efforts towards the fabrication and characterisation of strained germanium quantum wells (sGe-QWs) were motivated by the high mobility of holes in strained Ge and the compatibility of Ge with fabrication techniques in CMOS. This thesis, as an alternative to well-established techniques, reported a contact-less characterisation of sGe-QWs by means of THz time-domain magneto spectroscopy (THz-TDMS) and polarisation resolved (PR)-THz-TDMS experiments.

Before presenting the obtained data and the experimental methodology, Chapter 2 reviewed spin-split two dimensional systems, with a particular focus on two-dimensional hole gases (2DHGs) and, especially, the case of heavy hole (HH) bands in sGe-QWs. After outlining the mobility enhancement due to the strain, the modulation doping in QWs was introduced as responsible for the structural inversion asymmetry (SIA). The SIA can result in Rashba spin-splitting at zero magnetic field, a remarkable feature for spintronic applications. The different Rashba spin-splitting for electrons, light and heavy holes have been outlined so that the k^3-dependence of the Rashba spin splitting, for HHs, was highlighted. In order to provide the theoretical background needed to interpret - and analyse - experimental data, the same chapter summarised the effects of external magnetic fields on the QW's band structure. A brief outline of magneto-transport (MT), and cyclotron resonance (CR), experiments introduced expected experimental results for similar systems.

The experimental setup for THz-TDMS and PR-THz-TDMS, together with samples characterised within this thesis, were presented in Chapter 3.

Chapter 4 reported a full characterisation of 0.8% compressively sGe-QWs by means of THz-TDMS, which allowed the determination of the longitudinal conductivity σ_{xx}. The transmission spectra for the two samples showed spin-split CRs, which confirmed the nonparabolic character of HH-bands in Ge. By modelling the transmission in the time- and frequency-domains, the HH's density, cyclotron energy and lifetime were evaluated.

The analysis of data below 3 T determined the spin-split HH density. While this was found to be in line with MT measurements for the inverse modulation doped sGe-QW, remarkably, THz-TDMS also determined the spin-split density within the normal modulation doped sGe-QW. In this case the analysis of MT experiments was complicated by the presence of the supply layer between the Hall bar and the QW. Spin-split densities were used for a first estimation of the Rashba coefficient, and the related Rashba spin-splitting energy Δ, which was found to be in line with MT results for the same sample. Δ was also estimated by modelling the experimental CRs, as obtained from an approximated calculation of Landau levels (LLs) and related CRs, which also allowed the determination the effective mass and g-factor for the two samples. As expected, the g-factor was found to increase with the QW-thickness, while Δ was in line with that determined from the spin-split density. The average value for the two samples was $\Delta \sim 2\,\mathrm{meV}$.

Finally, the transport lifetime was obtained from the magnetic field dependence of the CR-linewidth which, by using the determined effective mass from the LLs calculation, allowed the estimation of the mobility as high as $6 \times 10^5\,\mathrm{cm}^2/\mathrm{Vs}$ (average value for the two samples).

The characterisation of a different set of samples - 1.3% compressively sGe-QWs - was presented in Chapter 5, as obtained from PR-THz-TDMS experiments which evaluated σ_{xx}, as well as the transverse conductivity σ_{xy}. The transverse conductivity was obtained from the complex Faraday angle in the frequency-domain. By comparing the experimental complex Faraday angles, between 2DHGs in sGe-QWs and 2DEG in GaAs-QWs, Chapter 5 demonstrated the opposite response of 2D electrons and holes systems, as due to the opposite sign of the effective mass. Furthermore, spin-split CRs were not observed for the 2DEG, confirming the parabolicity of the conduction band in GaAs.

The total HH density was obtained from fits of σ_{xy}, in line with that evaluated from a sum-rule applied to σ_{xx}. Fits of σ_{xy} provided cyclotron energies and lifetimes which were used to estimate the g-factor, effective mass, transport lifetime and Rashba spin-splitting energy as presented in Chapter 4. Estimated g-factors confirmed higher values for thicker QWs while the mobility, as expected from the higher strain, was found to be $\sim 1.5 \times 10^6\,\mathrm{cm}^2/\mathrm{Vs}$.

The evaluated Rashba spin-splitting energy was $\Delta = 0.4 \pm 0.2\,\mathrm{meV}$ for both samples. By considering that in the 1.3% sGe-QWs the estimated density was higher than the 0.8% sGe-QWs (leading to $k_{\mathrm{F}}^{1.3\%} > k_{\mathrm{F}}^{0.8\%}$), and by assuming the same electric field, $\mathcal{E}_z$, from the modulation doping (same Boron concentration within the supply layer for all the studied samples) the decreased Rashba spin-splitting energy confirms the dependence on the strain which is related to the increased energy splitting between HH- and LH-bands ($\Delta = \beta k_{\mathrm{F}}^3$ with $\beta \propto \mathcal{E}_z / |E_{\mathrm{HH}} - E_{\mathrm{LH}}|^2$).

In addition, the determination of σ_{xy}, as well as the normalisation method reported in Chapter 5, allowed the first observation of the optical quantum Hall effect (OQHE) for 2DHGs, expanding the number of material systems known to exhibit the OQHE. Furthermore, in comparison with the OQHE in 2DEGs, this work reports the observation of broader plateaux as well as the observation of a plateau at odd filling factor, due to a substantial spin splitting.

Results in this thesis suggest a promising future for strained Ge in fundamental and applied physics.

6.5 Future prospects

Even if the following thesis confirmed important results (obtained in as-grown samples) such as the increasing of the mobility with increased strain or the important evaluation of the g-factor, further experimental and theoretical studies are needed in order to more deeply investigate the strain-dependence of the Rashba spin-splitting for HHs, or to understand how localised and delocalised states contribute to the OQHE.

Chapter 6 already gave a future direction of this work. A rotatable polarisation THz-TDS experiment was outlined as a method to evaluate the anisotropic character of the HH-band in sGe-QWs, thus the direction-dependent mobility.

Further insights into the Rashba effect for HHs in sGe-QWs can be obtained, for instance, by performing similar THz-TDMS experiments with the addition of a gate field. This would give a chance to more thoroughly investigate the Rashba effect's dependence on the density and electric field.

Bibliography

[1] S. Sze and K. Ng, *Physics of Semiconductor Devices.* Wiley, 2006.

[2] F. Schäffler, "High-mobility Si and Ge structures," *Semiconductor Science and Technology*, vol. 12, no. 12, p. 1515, 1997.

[3] G. E. Moore, "Cramming More Components onto Integrated Circuits," *Electronics*, vol. 38, pp. 114–117, Apr. 1965.

[4] N. Z. Haron and S. Hamdioui, "Why is CMOS scaling coming to an END?," in *2008 3rd International Design and Test Workshop*, pp. 98–103, Dec 2008.

[5] R. D. Clark, "Emerging applications for high k materials in VLSI technology," *Materials*, vol. 7, no. 4, p. 2913, 2014.

[6] S. E. Thompson, M. Armstrong, C. Auth, *et al.*, "A 90-nm logic technology featuring strained-silicon," *IEEE Transactions on Electron Devices*, vol. 51, pp. 1790–1797, Nov 2004.

[7] K. J. Kuhn, A. Murthy, R. Kotlyar, and M. Kuhn, "(invited) past, present and future: SiGe and CMOS transistor scaling," *ECS Transactions*, vol. 33, no. 6, pp. 3–17, 2010.

[8] A. Chaudhry and M. J. Kumar, "Controlling short-channel effects in deep-submicron SOI MOSFETs for improved reliability: a review," *IEEE Transactions on Device and Materials Reliability*, vol. 4, pp. 99–109, March 2004.

[9] D. Hisamoto, W.-C. Lee, J. Kedzierski, *et al.*, "FinFET-a self-aligned double-gate MOSFET scalable to 20 nm," *IEEE Transactions on Electron Devices*, vol. 47, pp. 2320–2325, Dec 2000.

[10] C. Auth, C. Allen, A. Blattner, D. Bergstrom, *et al.*, "A 22nm high performance and low-power CMOS technology featuring fully-depleted tri-gate

transistors, self-aligned contacts and high density MIM capacitors," in *2012 Symposium on VLSI Technology (VLSIT)*, pp. 131–132, June 2012.

[11] S. Natarajan, M. Agostinelli, S. Akbar, M. Bost, *et al.*, "A 14nm logic technology featuring 2nd-generation FinFET, air-gapped interconnects, self-aligned double patterning and a 0.0588 μm^2 SRAM cell size," in *2014 IEEE International Electron Devices Meeting*, 2014.

[12] "The International Technology Roadmap for Semiconductors (ITRS), System Drivers, 2007, http://www.itrs.net/,"

[13] J. A. D. Alamo, D. A. Antoniadis, J. Lin, W. Lu, A. Vardi, and X. Zhao, "Nanometer-scale III-V MOSFETs," *IEEE Journal of the Electron Devices Society*, vol. 4, pp. 205–214, Sept 2016.

[14] M. Heyns and W. Tsai, "Ultimate Scaling of CMOS Logic Devices with Ge and III/V Materials," *MRS Bulletin*, vol. 34, pp. 485–492, 007 2009.

[15] D. P. Brunco, B. De Jaeger, G. Eneman, J. Mitard, *et al.*, "Germanium MOSFET devices: Advances in materials understanding, process development, and electrical performance," *Journal of The Electrochemical Society*, vol. 155, no. 7, pp. H552–H561, 2008.

[16] S. Takagi, T. Iisawa, T. Tezuka, T. Numata, *et al.*, "Carrier-transport-enhanced channel CMOS for improved power consumption and performance," *IEEE Transactions on Electron Devices*, vol. 55, no. 1, pp. 21–39, 2008.

[17] "The International Technology Roadmap for Semiconductors (ITRS), System Drivers, 2011, http://www.itrs.net/,"

[18] S. Takagi, S.-H. Kim, M. Yokoyama, R. Zhang, *et al.*, "High mobility CMOS technologies using IIIV/Ge channels on Si platform," *Solid-State Electronics*, vol. 88, pp. 2 – 8, 2013. Selected extended papers from {ULIS} 2012 conference.

[19] D. J. Frank, R. H. Dennard, E. Nowak, P. M. Solomon, Y. Taur, and H.-S. P. Wong, "Device scaling limits of Si MOSFETs and their application dependencies," *Proceedings of the IEEE*, vol. 89, pp. 259–288, Mar 2001.

[20] M. Myronov, C. Morrison, J. Halpin, S. Rhead, J. Foronda, and D. Leadley, "Revealing high room and low temperatures mobilities of 2D holes in a strained Ge quantum well heterostructures grown on a standard Si(001) substrate," *Solid-State Electronics*, vol. 110, pp. 35–39, 2015.

[21] R. Pillarisetty, "Academic and industry research progress in germanium nanodevices," *Nature*, vol. 479, pp. 324–328, 2011.

[22] N.-T. Yeh, P.-C. Chiu, J.-I. Chyi, F. Ren, and S. J. Pearton, "Sb-based semiconductors for low power electronics," *J. Mater. Chem. C*, vol. 1, pp. 4616–4627, 2013.

[23] V. Umansky, M. Heiblum, Y. Levinson, J. Smet, J. Nbler, and M. Dolev, "MBE growth of ultra-low disorder 2DEG with mobility exceeding 35×10^6 $\mathrm{cm}^2/\mathrm{Vs}$," *Journal of Crystal Growth*, vol. 311, no. 7, pp. 1658 – 1661, 2009. International Conference on Molecular Beam Epitaxy (MBE-XV)The 15th International Conference on Molecular Beam Epitaxy (MBE-XV).

[24] "The International Technology Roadmap for Semiconductors (ITRS), System Drivers, 2009, http://www.itrs.net/,"

[25] "The International Technology Roadmap for Semiconductors (ITRS), System Drivers, 2003, http://www.itrs.net/,"

[26] C. Morrison and M. Myronov, "Strained germanium for applications in spintronics," *physica status solidi (a)*, vol. 213, no. 11, pp. 2809–2819, 2016.

[27] K. Morii, T. Iwasaki, R. Nakane, M. Takenaka, and S. Takagi, "High-performance GeO_2/Ge nMOSFETs with source/drain junctions formed by gas-phase doping," *IEEE Electron Device Letters*, vol. 31, pp. 1092–1094, Oct 2010.

[28] I. Žutić and S. Das Sarma, "Spintronics: Fundamentals and applications," *Reviews of Modern Physics*, vol. 76, pp. 323–410, Apr. 2004.

[29] S. Dushenko, M. Koike, Y. Ando, T. Shinjo, M. Myronov, and M. Shiraishi, "Experimental demonstration of room-temperature spin transport in n-type germanium epilayers," *Phys. Rev. Lett.*, vol. 114, p. 196602, May 2015.

[30] A. Jain, J.-C. Rojas-Sanchez, M. Cubukcu, J. Peiro, *et al.*, "Crossover from spin accumulation into interface states to spin injection in the germanium conduction band," *Phys. Rev. Lett.*, vol. 109, p. 106603, Sep 2012.

[31] Y. Zhou, W. Han, L.-T. Chang, F. Xiu, M. Wang, M. Oehme, I. A. Fischer, J. Schulze, R. K. Kawakami, and K. L. Wang, "Electrical spin injection and transport in germanium," *Phys. Rev. B*, vol. 84, p. 125323, Sep 2011.

[32] C. Hautmann, B. Surrer, and M. Betz, "Ultrafast optical orientation and coherent Larmor precession of electron and hole spins in bulk germanium," *Physical Review B*, vol. 83, p. 161203, Apr. 2011.

[33] R. Berthelon, F. Andrieu, P. Perreau, E. Baylac, A. Pofelski, E. Josse, D. Dutartre, A. Claverie, and M. Haond, "Performance and layout effects of SiGe channel in 14nm UTBB FDSOI: SiGe-first vs. SiGe-last integration," in *2016 46th European Solid-State Device Research Conference (ESSDERC)*, pp. 127–130, Sept 2016.

[34] E. Kasper, A. Schuh, G. Bauer, B. Hollnder, and H. Kibbel, "Test of Vegard's law in thin epitaxial SiGe layers," *Journal of Crystal Growth*, vol. 157, no. 1, pp. 68 – 72, 1995.

[35] Y. Yamamoto, P. Zaumseil, T. Arguirov, M. Kittler, and B. Tillack, "Low threading dislocation density Ge deposited on Si(100) using RPCVD," *Solid-State Electronics*, vol. 60, no. 1, pp. 2 – 6, 2011. Papers Selected from the 5th International SiGe Technology and Devices Meeting (ISTDM 2010).

[36] J. Matthews and A. Blakeslee, "Defects in epitaxial multilayers," *Journal of Crystal Growth*, vol. 27, pp. 118 – 125, 1974.

[37] R. People and J. C. Bean, "Calculation of critical layer thickness versus lattice mismatch for $\mathrm{Ge}_x\mathrm{Si}_{1-x}$/Si strainedlayer heterostructures," *Applied Physics Letters*, vol. 47, no. 3, pp. 322–324, 1985.

[38] S. B. Samavedam, W. J. Taylor, J. M. Grant, J. A. Smith, P. J. Tobin, A. Dip, A. M. Phillips, and R. Liu, "Relaxation of strained Si layers grown on SiGe buffers," *Journal of Vacuum Science & Technology B: Microelectronics and Nanometer Structures Processing, Measurement, and Phenomena*, vol. 17, no. 4, pp. 1424–1429, 1999.

[39] P. YU and M. Cardona, *Fundamentals of Semiconductor: Physics and Materials Properties.* Springer Berlin Heidelberg, 2013.

[40] C. Kittel, *Introduction to Solid State Physics.* Wiley, 2004.

[41] R. Tilley, *Crystals and Crystal Structures.* Wiley, 2006.

[42] R. Boyd, *Nonlinear Optics.* Elsevier Science, 2013.

[43] M. Cohen and J. Chelikowsky, *Electronic structure and optical properties of semiconductors.* Springer series in solid-state sciences, Springer-Verlag, 1988.

[44] J. H. Davies, *The physics of low-dimensional semiconductors : an introduction.* Cambridge University Press, 1998.

[45] T. Ihn, *Semiconductor Nanostructures: Quantum states and electronic transport.* Oxford University Press, 2010.

[46] R. Winkler, *Spin-Orbit Coupling Effects in Two-Dimensional Electron and Hole Systems.* Springer-Verlag Berlin Heidelberg, 2003.

[47] G. Dresselhaus, A. F. Kip, and C. Kittel, "Cyclotron resonance of electrons and holes in silicon and germanium crystals," *Phys. Rev.*, vol. 98, pp. 368–384, Apr 1955.

[48] P. Löwdin, "A note on the quantummechanical perturbation theory," *The Journal of Chemical Physics*, vol. 19, no. 11, pp. 1396–1401, 1951.

[49] H. Mayer and U. Rössler, "Spin splitting and anisotropy of cyclotron resonance in the conduction band of GaAs," *Phys. Rev. B*, vol. 44, pp. 9048–9051, Oct 1991.

[50] M. V. Fischetti and S. E. Laux, "Band structure, deformation potentials, and carrier mobility in strained Si, Ge, and SiGe alloys," *Journal of Applied Physics*, vol. 80, no. 4, pp. 2234–2252, 1996.

[51] A. Manchon, H. C. Koo, J. Nitta, S. M. Frolov, and R. A. Duine, "New perspectives for Rashba spin-orbit coupling," *Nature Mater*, vol. 14, p. 871, Aug 2015.

[52] Y. A. Bychkov and E. Rashba, "Properties of a 2D electron gas with lifted spectral degeneracy," *JETP lett*, vol. 39, no. 2, p. 78, 1984.

[53] R. Winkler, D. Culcer, S. J. Papadakis, B. Habib, and M. Shayegan, "Spin orientation of holes in quantum wells," *Semiconductor Science and Technology*, vol. 23, p. 114017, Nov. 2008.

[54] A. Balocchi, Q. H. Duong, P. Renucci, B. L. Liu, C. Fontaine, T. Amand, D. Lagarde, and X. Marie, "Full electrical control of the electron spin relaxation in GaAs quantum wells," *Phys. Rev. Lett.*, vol. 107, p. 136604, Sep 2011.

[55] M. Dyakonov, *Spin Physics in Semiconductors.* Springer Series in Solid-State Sciences, Springer Berlin Heidelberg, 2008.

[56] H. Nakamura, T. Koga, and T. Kimura, "Experimental evidence of cubic Rashba effect in an inversion-symmetric oxide," *Phys. Rev. Lett.*, vol. 108, p. 206601, May 2012.

[57] R. Winkler, M. Merkler, T. Darnhofer, and U. Rössler, "Theory for the cyclotron resonance of holes in strained asymmetric Ge-SiGe quantum wells," *Phys. Rev. B*, vol. 53, pp. 10858–10865, Apr 1996.

[58] C. Engelhardt, D. Tbben, M. Aschauer, F. Schffler, G. Abstreiter, and E. Gornik, "High mobility 2D hole gases in strained Ge channels on Si substrates studied by magnetotransport and cyclotron resonance," *Solid-State Electronics*, vol. 37, no. 4-6, pp. 949 – 952, 1994.

[59] R. Moriya, K. Sawano, Y. Hoshi, S. Masubuchi, Y. Shiraki, A. Wild, C. Neumann, G. Abstreiter, D. Bougeard, T. Koga, and T. Machida, "Cubic Rashba spin-orbit interaction of a two-dimensional hole gas in a strained-Ge/SiGe quantum well," *Phys. Rev. Lett.*, vol. 113, p. 086601, Aug 2014.

[60] T. Koga, J. Nitta, T. Akazaki, and H. Takayanagi, "Rashba spin-orbit coupling probed by the weak antilocalization analysis in InAlAs/InGaAs/InAlAs quantum wells as a function of quantum well asymmetry," *Physical review letters*, vol. 89, no. 4, p. 046801, 2002.

[61] F. J. Ohkawa and Y. Uemura, "Quantized surface states of a narrow-gap semiconductor," *Journal of the Physical Society of Japan*, vol. 37, no. 5, pp. 1325–1333, 1974.

[62] S. Datta and B. Das, "Electronic analog of the electro-optic modulator," *Appl. Phys. Lett.*, vol. 56, p. 665, Feb. 1990.

[63] H. C. Koo, J. H. Kwon, J. Eom, J. Chang, S. H. Han, and M. Johnson, "Control of spin precession in a spin-injected field effect transistor.," *Science*, vol. 325, pp. 1515–8, Sept. 2009.

[64] M. Dyakonov, *Spin Physics in Semiconductors.* Springer Series in Solid-State Sciences, Springer Berlin Heidelberg, 2010.

[65] R. J. Elliott, "Theory of the effect of spin-orbit coupling on magnetic resonance in some semiconductors," *Phys. Rev.*, vol. 96, pp. 266–279, Oct 1954.

[66] M. Dyakonov and V. Perel, "Spin relaxation of conduction electrons in noncentrosymmetric semiconductors," *Soviet Physics Solid State, Ussr*, vol. 13, no. 12, pp. 3023–3026, 1972.

[67] E. D. Palik and J. K. Furdyna, “Infrared and microwave magnetoplasma effects in semiconductors,” *Reports on Progress in Physics*, vol. 33, no. 3, p. 1193, 1970.

[68] T. Janssen, A. Tzalenchuk, S. Lara-Avila, S. Kubatkin, and V. Fal’Ko, “Quantum resistance metrology using graphene,” *Reports on Progress in Physics*, vol. 76, no. 10, p. 104501, 2013.

[69] T. Ando, A. B. Fowler, and F. Stern, “Electronic properties of two-dimensional systems,” *Rev. Mod. Phys.*, vol. 54, pp. 437–672, Apr 1982.

[70] Y. Ikebe, T. Morimoto, R. Masutomi, T. Okamoto, H. Aoki, and R. Shimano, “Optical Hall effect in the integer quantum Hall regime,” *Phys. Rev. Lett.*, vol. 104, p. 256802, Jun 2010.

[71] H. Aoki and T. Ando, “Critical localization in two-dimensional Landau quantization,” *Phys. Rev. Lett.*, vol. 54, pp. 831–834, Feb 1985.

[72] B. Huckestein, “Scaling theory of the integer quantum Hall effect,” *Rev. Mod. Phys.*, vol. 67, pp. 357–396, Apr 1995.

[73] I. Berkutov, V. Andrievskii, Y. F. Komnik, Y. A. Kolesnichenko, R. Morris, D. Leadley, and O. Mironov, “Magnetotransport studies of SiGe-based p-type heterostructures: problems of the effective mass determination,” *Low Temperature Physics*, vol. 38, no. 12, pp. 1455–1463, 2012.

[74] B. Das, D. C. Miller, S. Datta, R. Reifenberger, W. P. Hong, P. K. Bhattacharya, J. Singh, and M. Jaffe, “Evidence for spin splitting in $\mathrm{In}_x\mathrm{Ga}_{1-x}\mathrm{As}/\mathrm{In}_{0.52}\mathrm{Al}_{0.48}\mathrm{As}$ heterostructures as $B \to 0$,” *Phys. Rev. B*, vol. 39, pp. 1411–1414, Jan 1989.

[75] C. Morrison, M. Myronov, P. Wiśniewski, S. D. Rhead, J. Foronda, and D. R. Leadley, “Observation of Rashba zero-field spin splitting in a strained germanium 2D hole gas,” *Appl. Phys. Lett.* , vol. 105, p. 182401, 2014.

[76] A. Hassan, R. J. Morris, O. Mironov, S. Gabani, A. Dobbie, and D. R. Leadley, “An origin behind Rashba spin splitting within inverted doped sGe heterostructures,” *Applied Physics Letters*, vol. 110, no. 4, p. 042405, 2017.

[77] J. Luo, H. Munekata, F. F. Fang, and P. J. Stiles, “Observation of the zero-field spin splitting of the ground electron subband in GaSb-InA-GaSb quantum wells,” *Phys. Rev. B*, vol. 38, pp. 10142–10145, Nov 1988.

[78] K. S. Cho, T.-Y. Huang, H.-S. Wang, M.-G. Lin, T.-M. Chen, C.-T. Liang, Y. F. Chen, and I. Lo, "Zero-field spin splitting in modulation-doped $Al_xGa_{1-x}N/GaN$ two-dimensional electron systems," *Applied Physics Letters*, vol. 86, no. 22, p. 222102, 2005.

[79] P. Bhattacharya, *Comprehensive semiconductor science and technology: 6 Volumes.* Elsevier, 2011.

[80] G. Landwehr and E. Rashba, *Landau Level Spectroscopy.* No. pt. 1 in MODERN PROBLEMS IN CONDENSED MATTER SCIENCES, North-Holland, 1991.

[81] R. Ulbricht, E. Hendry, J. Shan, T. F. Heinz, and M. Bonn, "Carrier dynamics in semiconductors studied with time-resolved terahertz spectroscopy," *Rev. Mod. Phys.*, vol. 83, pp. 543–586, Jun 2011.

[82] Spectra-Physics, *MAITAI manual.*

[83] Y. Lee, *Principles of Terahertz Science and Technology.* Springer US, 2010.

[84] G. Gallot, J. Zhang, R. W. McGowan, T.-I. Jeon, and D. Grischkowsky, "Measurements of the THz absorption and dispersion of ZnTe and their relevance to the electro-optic detection of THz radiation," *Applied Physics Letters*, vol. 74, no. 23, pp. 3450–3452, 1999.

[85] D. Marple, "Refractive index of ZnSe, ZnTe, and CdTe," *Journal of Applied Physics*, vol. 35, no. 3, pp. 539–542, 1964.

[86] P. C. Planken, H.-K. Nienhuys, H. J. Bakker, and T. Wenckebach, "Measurement and calculation of the orientation dependence of terahertz pulse detection in ZnTe," *JOSA B*, vol. 18, no. 3, pp. 313–317, 2001.

[87] N. C. J. van der Valk, T. Wenckebach, and P. C. M. Planken, "Full mathematical description of electro-optic detection in optically isotropic crystals," *J. Opt. Soc. Am. B*, vol. 21, pp. 622–631, Mar 2004.

[88] N. C. van der Valk, W. A. van der Marel, and P. C. Planken, "Terahertz polarization imaging," *Opt. Lett.*, vol. 30, pp. 2802–2804, Oct 2005.

[89] J. Lloyd-Hughes and T.-I. Jeon, "A review of the terahertz conductivity of bulk and nano-materials," *Journal of Infrared, Millimeter, and Terahertz Waves*, vol. 33, no. 9, pp. 871–925, 2012.

[90] M. Myronov, X.-C. Liu, A. Dobbie, and D. Leadley, "Control of epilayer thickness during epitaxial growth of high Ge content strained Ge/SiGe multilayers by RP-CVD," *Journal of Crystal Growth*, vol. 318, no. 1, pp. 337 – 340, 2011. The 16th International Conference on Crystal Growth (ICCG16)/The 14th International Conference on Vapor Growth and Epitaxy (ICVGE14).

[91] V. A. Shah, A. Dobbie, M. Myronov, D. J. F. Fulgoni, L. J. Nash, and D. R. Leadley, "Reverse graded relaxed buffers for high Ge content SiGe virtual substrates," *Applied Physics Letters*, vol. 93, no. 19, p. 192103, 2008.

[92] M. Myronov, C. Morrison, J. Halpin, S. Rhead, C. Casteleiro, J. Foronda, V. A. Shah, and D. Leadley, "An extremely high room temperature mobility of two-dimensional holes in a strained Ge quantum well heterostructure grown by reduced pressure chemical vapor deposition," *Japanese Journal of Applied Physics*, vol. 53, no. 4S, p. 04EH02, 2014.

[93] L. Golub and E. Ivchenko, "Spin splitting in symmetrical SiGe quantum wells," *Physical Review B*, vol. 69, no. 11, p. 115333, 2004.

[94] S. N. Holmes, P. J. Newton, J. Llandro, R. Mansell, C. H. W. Barnes, C. Morrison, and M. Myronov, "Spin-splitting in p-type Ge devices," *Journal of Applied Physics*, vol. 120, no. 8, p. 085702, 2016.

[95] M. J. Palmer, G. Braithwaite, M. J. Prest, E. H. C. Parker, T. E. Whall, Y. P. Zhao, S. Kaya, J. R. Watling, A. Asenov, J. R. Barker, A. M. Waite, and A. G. R. Evans, "Enhanced velocity overshoot and transconductance in Si/$\mathrm{Si}_{0.64}\mathrm{Ge}_{0.36}$/Si pMOSFETs - predictions for deep submicron devices," in *31st European Solid-State Device Research Conference*, pp. 199–202, September 2001.

[96] R. A. Logan, J. M. Rowell, and F. A. Trumbore, "Phonon spectra of Ge-Si alloys," *Phys. Rev.*, vol. 136, pp. A1751–A1755, Dec 1964.

[97] C. Morrison, J. Foronda, P. Winiewski, S. Rhead, D. Leadley, and M. Myronov, "Evidence of strong spin-orbit interaction in strained epitaxial germanium," *Thin Solid Films*, vol. 602, pp. 84 – 89, 2016. The 9th International Conference on Silicon Epitaxy and Heterostructures.

[98] D. Some and A. V. Nurmikko, "Realtime electron cyclotron oscillations observed by terahertz techniques in semiconductor heterostructures," *Applied Physics Letters*, vol. 65, no. 26, pp. 3377–3379, 1994.

[99] G. Brooker, *Modern Classical Optics (Oxford Master Series in Atomic, Optical and Laser Physics).* Oxford University Press, USA, Oct. 2003.

[100] A. I. Akhiezer, *Plasma electrodynamics.* Pergamon Press, 1975.

[101] T. Arikawa, X. Wang, D. J. Hilton, J. L. Reno, W. Pan, and J. Kono, "Quantum control of a Landau-quantized two-dimensional electron gas in a GaAs quantum well using coherent terahertz pulses," *Phys. Rev. B*, vol. 84, p. 241307, Dec. 2011.

[102] J. Scriba, A. Wixforth, J. Kotthaus, C. Bolognesi, C. Nguyen, and H. Kroemer, "Spin-and Landau-splitting of the cyclotron resonance in a nonparabolic two-dimensional electron system," *Solid State Communications*, vol. 86, pp. 633–636, June 1993.

[103] I. B. Berkutov, V. V. Andrievski, Y. F. Komnik, O. A. Mironov, M. Mironov, and D. R. Leadley, "Shubnikov-de Haas oscillations of the conductivity of a two-dimensional gas in quantum wells based on germanium and silicon. determination of the effective mass and g factor," *Low Temperature Physics*, vol. 35, no. 2, pp. 141–145, 2009.

[104] N. A. Kabir, Y. Yoon, J. R. Knab, J.-Y. Chen, A. G. Markelz, J. L. Reno, Y. Sadofyev, S. Johnson, Y.-H. Zhang, and J. P. Bird, "Terahertz transmission characteristics of high-mobility GaAs and InAs two-dimensional-electron-gas systems," *Applied Physics Letters*, vol. 89, no. 13, 2006.

[105] A. H. A. Hassan, R. J. H. Morris, O. A. Mironov, R. Beanland, D. Walker, S. Huband, A. Dobbie, M. Myronov, and D. R. Leadley, "Anisotropy in the hole mobility measured along the orientations in a strained Ge quantum well," *Applied Physics Letters*, vol. 104, no. 13, 2014.

[106] T. Unuma, M. Yoshita, and T. Noda, "Intersubband absorption linewidth in GaAs quantum wells due to scattering by interface roughness, phonons, alloy disorder, and impurities," *J. Appl. Phys.*, vol. 93, no. 3, p. 1586, 2003.

[107] M. Singh, "Quantum theory of the cyclotron-resonance line shape in the presence of hole-phonon interactions in p-type multi-quantum-well structures," *Phys. Rev. B*, vol. 36, pp. 5062–5065, Sept. 1987.

[108] M. Singh, "Hole-phonon relaxation time and Landau-level broadening due to hole-phonon interactions in multiple-quantum-well structures in the presence

of a magnetic field and internal strains," *Phys. Rev. B*, vol. 36, pp. 1178–1185, July 1987.

[109] M. P. Chaubey, "Quantum theory of cyclotron-resonance line shape of a two-dimensional hole gas due to hole-phonon interaction in microstructures," *Phys. Rev. B*, vol. 38, pp. 5422–5429, Sept. 1988.

[110] J. Luo, H. Munekata, F. F. Fang, and P. J. Stiles, "Effects of inversion asymmetry on electron energy band structures in GaSb/InAs/GaSb quantum wells," *Phys. Rev. B*, vol. 41, pp. 7685–7693, Apr 1990.

[111] M. Mansuripur, "The Faraday effect," *Optics & Photonics News*, vol. 10, pp. 32–36, Nov. 1999.

[112] T. Arikawa, Q. Zhang, L. Ren, A. A. Belyanin, and J. Kono, "Review of anisotropic terahertz material response," *Journal of Infrared, Millimeter, and Terahertz Waves*, vol. 34, no. 11, pp. 724–739, 2013.

[113] N. Miura, "2.08 - magneto-spectroscopy of semiconductors," in *Comprehensive Semiconductor Science and Technology* (P. Bhattacharya, R. Fornari, and H. Kamimura, eds.), pp. 256 – 342, Amsterdam: Elsevier, 2011.

[114] R. F. O'Connell and G. Wallace, "Ellipticity and Faraday rotation due to a two-dimensional electron gas in a metal-oxide-semiconductor system," *Phys. Rev. B*, vol. 26, pp. 2231–2234, Aug 1982.

[115] K. Chiu, T. Lee, and J. Quinn, "Infrared magneto-transmittance of a two-dimensional electron gas," *Surface Science*, vol. 58, no. 1, pp. 182 – 184, 1976.

[116] T. Morimoto, Y. Hatsugai, and H. Aoki, "Optical Hall conductivity in ordinary and graphene quantum Hall systems," *Phys. Rev. Lett.*, vol. 103, p. 116803, Sep 2009.

[117] A. V. Stier, C. T. Ellis, J. Kwon, H. Xing, H. Zhang, D. Eason, G. Strasser, T. Morimoto, H. Aoki, H. Zeng, B. D. McCombe, and J. Cerne, "Terahertz dynamics of a topologically protected state: Quantum Hall effect plateaus near the cyclotron resonance of a two-dimensional electron gas," *Phys. Rev. Lett.*, vol. 115, p. 247401, Dec 2015.

[118] R. Shimano, G. Yumoto, J. Y. Yoo, R. Matsunaga, S. Tanabe, H. Hibino, T. Morimoto, and H. Aoki, "Quantum Faraday and Kerr rotations in graphene.," *Nature Communications*, vol. 4, p. 1841, jan 2013.

[119] J. Lloyd-Hughes, S. P. P. Jones, E. Castro-Camus, K. I. Doig, and J. L. MacManus-Driscoll, "Modifying the polarization state of terahertz radiation using anisotropic twin-domains in $LaAlO_3$, url = http://ol.osa.org/abstract.cfm?URI=ol-39-5-1121, volume = 39, year = 2014," *Optics Letters*, p. 1121, feb.

[120] J. Lloyd-Hughes, H. E. Beere, D. A. Ritchie, and M. Johnston, "Terahertz magnetoconductivity of excitons and electrons in quantum cascade structures," *Physical Review B*, vol. 77, p. 125322, mar 2008.

[121] X. Wang, D. J. Hilton, L. Ren, D. M. Mittleman, J. Kono, and J. L. Reno, "Terahertz time-domain magnetospectroscopy of a high-mobility two-dimensional electron gas," *Opt. Lett.*, vol. 32, pp. 1845–1847, Jul 2007.

[122] H. D. Drew and P. Coleman, "Sum rule for the optical Hall angle," *Phys. Rev. Lett.*, vol. 78, pp. 1572–1575, Feb 1997.

[123] C. Maissen, G. Scalari, F. Valmorra, M. Beck, J. Faist, S. Cibella, R. Leoni, C. Reichl, C. Charpentier, and W. Wegscheider, "Ultrastrong coupling in the near field of complementary split-ring resonators," *Phys. Rev. B*, vol. 90, p. 205309, Nov 2014.

[124] M. E. Levinshtein, S. L. Rumyantsev, and M. Shur, *Properties of advanced semiconductor materials : GaN, AlN, InN, BN, SiC, SiGe.* Wiley, 2001.

[125] J. Lloyd-Hughes, "Terahertz spectroscopy of quantum 2D electron systems," *Journal of Physics D: Applied Physics*, vol. 47, p. 374006, sep 2014.

[126] T. Englert, J. Maan, C. Uihlein, D. Tsui, and A. Gossard *Solid State Communications*, vol. 46, no. 7, pp. 545 – 548, 1983.

[127] N. Kamaraju, W. Pan, U. Ekenberg, D. M. Gvozdi, S. Boubanga-Tombet, P. C. Upadhya, J. Reno, A. J. Taylor, and R. P. Prasankumar, "Terahertz magneto-optical spectroscopy of a two-dimensional hole gas," *Applied Physics Letters*, vol. 106, no. 3, 2015.

[128] Q. Shi, M. A. Zudov, C. Morrison, and M. Myronov, "Spinless composite fermions in an ultrahigh-quality strained Ge quantum well," *Physical Review B*, vol. 91, p. 241303, June 2015.

[129] O. Mironov, N. D'Ambrumenil, A. Dobbie, D. Leadley, A. Suslov, and E. Green, "Fractional Quantum Hall States in a Ge Quantum Well," *Physical Review Letters*, vol. 116, p. 176802, apr 2016.

[130] M. Fischetti, Z. Ren, P. Solomon, M. Yang, and K. Rim, "Six-band k·p calculation of the hole mobility in silicon inversion layers: Dependence on surface orientation, strain, and silicon thickness," *Journal of Applied Physics*, vol. 94, no. 2, pp. 1079–1095, 2003.

[131] S. Dissanayake, Y. Zhao, S. Sugahara, M. Takenaka, and S. Takagi, "Channel direction, effective field, and temperature dependencies of hole mobility in (110)-oriented Ge-on-insulator p-channel metal-oxide-semiconductor field-effect transistors fabricated by Ge condensation technique," *Journal of Applied Physics*, vol. 109, no. 3, p. 033709, 2011.

[132] M. Myronov and C. Morrison, "2D holes mobility in strained epitaxial germanium," Presented at the 10th International Conference on Silicon Epitaxy and heterostructures, The University of Warwick, Coventry, UK, 18 May 2017.

[133] Y. Sun, S. E. Thompson, and T. Nishida, "Physics of strain effects in semiconductors and metal-oxide-semiconductor field-effect transistors," *Journal of Applied Physics*, vol. 101, no. 10, p. 104503, 2007.

[134] "AZ5214E photoresist," *Merck Performance Materials GmbH.*